2015

Insights into Proton Conducting Solid Oxide Cell for Production of Power and Fuel

Hyunho Shin
Lehigh University

Insights into Proton Conducting Solid Oxide Cell for Production of Power and Fuel

by

Hyun Ho Shin

Presented to the Graduate and Research Committee

of Lehigh University

in Candidacy for the degree of

Doctor of Philosophy

In

Chemical Engineering

Lehigh University

May 2015

DISSERTATION SIGNATURE SHEET

Approved and recommended for acceptance as a dissertation draft in partial fulfillment of the requirements for the degree of Doctor of Philosophy.

_____
Date

_____
Dissertation Director

_____
Accepted Date

Committee Members:

_____
Prof. Steven McIntosh

_____
Prof. Mark A. Snyder

_____
Prof. Israel E. Wachs

_____
Prof. Christopher J. Kiely

Acknowledgement

Even if this dissertation is my own work, I believe that I would never have come to here without the help, support, and guidance of many people. First I would like to deeply thank my advisor, Prof. Steven McIntosh who motivate and encourage students whenever they are in trouble with research work as well as personal life. I wish to thank my committee member Prof. Israel E Wachs, Prof. Mark A. Snyder and Prof Christopher J. Kiely for their guidance over the years. I also would like to thank Prof. Jae Soo You at Chung-Ang University for helping me to start on the path that has led me here.

On a personal level, I would wish thank all of my friend and colleagues at Lehigh University for their support and help over last five years. A very special thank you to all my lab colleague, Mazin Tamimi who is walking dictionary, Alex Tomkiewicz who I can recognize if he is in lab even at the end of hall way by his loud voice and Zhou Yangwho is best coworker ever that I have met so far. I sincerely hope to get an opportunity to work together again. I would like to specially thank to Minseok Song who led me into smoking and mobile game temptation. You are so Korean! I also wish to thank Sungyoung Kim who is Dr. junk. Thanks to Unsam Lee who asked me to put her name here by force, congratulations on your wedding day.

In addition, I wish to thank all my family, my mother and father whom has always been there through my entire life, my brother who had given me a hug whenever I was crying in my childhood, my brother's wife who is the most beautiful in the world and brought big pleasure into our family, so much adorable Wooin and Wooyoung who are my niece and everything to me. Lastly, this dissertation is dedicated to my parents.

Table of contents

1. Introduction 2

1.1 Background and Motivation 2

1.2 SOFC Operation 3

1.3 Perovskite Oxide and Transport Mechanism 5

1.4 Hydrogen Oxidation 8

1.5 Material Choice 11

1.6 Powder Synthesis 13

1.7 X-Ray Diffraction 14

1.8 H2/D2 pulse isotope exchange experiments 15

1.9 Surface Investigation: High Sensitivity-Low Energy Ion Scattering (HS-LEIS) & X-Ray Photoelectron Spectroscopy (XPS) 17

1.10 References 19

2. On H_2/D_2 Isotopic Exchange Rate of Proton Conducting Barium Cerates and Zirconates 24

2.1 Introduction 24

2.2 Experimental 25

2.3 Results 27

2.4 Discussion 37

2.5 Conclusion 46

2.6 References 47

3. Insights into hydrogen oxidation on SOFC anode materials by isotopic exchange.. 50

3.1 Introduction *50*

3.2 Experimental *51*

3.3 Results and discussion *52*

3.4 Conclusion *60*

3.5 References *60*

4. Proton Conducting Perovskites as Supports for Cr Catalysts in Short Contact Time Ethane Dehydrogenation 62

4.1 Introduction *62*

4.2 Experimental *63*

4.3 Results *67*

4.4 Discussion *83*

4.5 Conclusion *87*

4.6 References *88*

5. High elective CO_2 methanation over supported Co and Pt nanoparticles on proton conducting $BaZrO_3$ 91

5.1 Introduction *91*

5.2 Experimental *92*

5.3 Results and Discussion *96*

5.4 References *109*

6. Conclusion 111

7. Vita. 113

List of figures

Figure 1.1 Schematic diagram of proton conducting SOFC during operation 4
Figure 1.2 Ideal cubic perovskite 6
Figure 1.3 Trace of proton (orange): rotational motion and proton transfer[10] 8
Figure 1.4 Possible anodic reaction pathway at a Ni/YSZ TPB (a-e) [35] 10
Figure 1.5 Bragg's diffraction 14
Figure 1.6 schematic representation of pulse H2/D2 isotopic exchangereaction 16
Figure 1.7 Schematic representation of the ion scattering process. 18
Figure 2.1 X-ray diffraction patterns of BC, BCY, BZ and BZY 31
Figure 2.2 SEM micrographs a) Ni/BZ and b) Pt/BZ 32
Figure 2.3 DH formation and D2 consumption in a single pulse (100μL, 5% D2) over BZ in dry H2 at a) 200 °C and b) 550 °C, DH and DHO formation and D2 consumption in wet H2 at c) 300 °C and d) 750 °C 33
Figure 2.4 Relative peak area of D2 and DH as a function of temperature for (a) BZ, (b) BC, (c) BZY and (d) BCY in dry H2, relative peak area of D2, DH and DHO for (e) BZ, (f) BC in wet H2. 34
Figure 2.5 Surface exchange reaction rates for H2/D2 isotope exchange over BZ, BZY, BC, BCY and M/BZ (M=Co, Ni, Cu and Pt) in dry H2, over BZ, BC and Pt/BZ in wet H2. 38
Figure 2.6 HS-LEIS spectrum of (a) BZ, (b) BaO2, (c) ZrO2, (d) BZY, (e) Y2O3 with4 keV Ne+ (1.03 × 1015 ions/cm2) 39
Figure 2.7 Depth profile measurement of (a) BZ and (b) BZY by repeated sputtering with Ar ion dose : 9.5 × 1014 (Ba:closed star, Zr:open star), 4.7× 1016 (Ba:closed square, Zr:closed circle) Ar+ ions/cm2. Back calculation (Ba:open square, Zr:open circle) 40
Figure 2.8 XPS scan for (a) BC and (b) BCY 41
Figure 3.1DH formation and D2 consumption in a single pulse (100μL, 5% D2) over YSZ in dry H2 at a) 200 °C and b) 650 °C, DH and DHO formation and D2 consumption in wet H2 at c) 300 °C and d) 700 °C 54
Figure 3.2 Relative peak area of D2 and DH as a function of temperature for (a) YSZ, (b) GDC in dry H2, D2, DH and DHO for (e) YSZ, (f) GDC in wet H2. 55
Figure 3.3 Surface exchange reaction rates for H2/D2 isotope exchange over YSZ, GDC and M/BZ (M=Ni, Cu and Pt) in dry H2, over YSZ, GDC and Pt/YSZ in wet H2. 58
Figure 4.1 X-ray diffraction patterns of (a) BZ, (b) 0.6Cr/BZ, (c) BC and (d) 0.6Cr/BC 70
Figure 4.2 Normalized ethylene yields versus time on stream over a) 0.2Cr/BZ and b) 0.2Cr/BC 71
Figure 4.3 Arrhenius plot of ethylene formation rate over Cr/BZ and Cr/BC at 1 minute on-stream. 73
Figure 4.4 Selectivity to ethylene over Cr/BZ and Cr/BC as a function of temperature at 1 minute on-stream 74
Figure 4.5 a) Temperature programmed oxidation (TPO) data showing CO2evolution (m/e=44) of carbon deposited during ethane dehydrogenation over 0.6Cr/BZ and 0.6Cr/BC at 575°C. b) Amount of carbon deposited (g/m2) over Cr/BZ and Cr/BC as a function of temperature. 75

Figure 4.6: a) Normalized ethylene yields versus time on stream over 0.6CrBC at different residence time; 0.06, 0.13, 0.31 and 0.63 sec at 575oC. b) Ethylene formation rate and the amount of carbon deposited as a function of residence time at 575oC. 77
Figure 4.7 Arrhenius plot of ethylene formation rate over Cr/BC and 10CrAl at residence time of 0.13 sec. 78
Figure 4.8 a) Normalized ethylene yields versus time on stream over 0.6CrBC at 575 ^{o}C in the presence of H2. b) The amount of carbon deposition and selectivity to ethylene at 1minute on-stream (inserted figure) as a function of concentration of H2, ... 80
Figure 4.9 XPS spectra for a) 10Cr/Al b) 0.2Cr/BZ and c) 0.2Cr/BC. 82
Figure 4.10 Normalized ethane conversion to ethylene versus time on stream over reduced 0.6Cr/BZ and oxidized 0.6Cr/BZ 84
Figure 5.1 X-ray diffraction patterns of BZ, BZY05 and BZY20. 97
Figure 5.2 Energy dispersive X-ray spectroscopy: (a) Co nanoparticles, (b) Pt nanoparticles, (c) supported Co and Pt over BZ. 98
Figure 5.3 Transmission electron micrograph of (a) as prepared cobalt nanoparticles, (b) cobalt nanoparticles, supported Pt and Co catalyst over BZ (c) before reaction and (d) after reaction for 3h. 99
Figure 5.4 (a) CH4 yield and (b) selectivity to CH4 versus temperature over 1Co/Al, 0.2Pt1Co/Al, 1Co/BZ and 0.2Pt1Co/BZ. 100
Figure 5.5 . XPS data: (a) and (b) 1Co/Al2O3, (c) and (d) 1Co/BZ (e) 0.2Pt1CoBZ before reaction and (f) 0.2Pt1CoBZ after reaction for 24h. 103
Figure 5.6 CH4 yield versus temperature over 0.2Pt1Co over BZ, BZY05 and BZY20 104
Figure 5.7 (a) CH4 yield versus time over 0.2Pt1Co/BZ at 300 and 350 ^{o}C and (b) temperature programmed oxidation (TPO) showing CO2 evolution (m/e 44) of carbon deposited during CO2 methanation at 300 and 350 ^{o}C. 107
Figure 5.8 temperature programmed oxidation (TPO) showing CO2 evolution (m/e 44) of carbon deposited during CO2 methanation at 300 and 350 ^{o}C. 108

List of Tables

Table 2.1 Crystallographic parameters and BET surface areas. 29
Table 2.2 Activation energy of H2/D2 surface exchange. 30
Table 3.1 Activation energy of H2/D2 surface exchange. 53
Table 4.1BET surface areas. 68
Table 4.2 XPS data 69

List of Symbols

E	open circuit potential (V)
E_b	Electron binding energy (eV)
E_o	reversible potential (V)
E_i	primary energy of ion (keV)
E_f	energy of backscattered ion (keV)
F	Faraday's constant (96485 C/mol)
R_o	overall surface exchange reaction rate (mol D $\cdot m^{-2} \cdot s^{-1}$) of Eqn. (15)
R	gas constant (8.314 J/mol-K)
T	temperature (K or ^oC)
f_g	fraction of deuterium isotope in gas phase of Eqn. (15)
f_o	fraction of deuterium isotope in oxide phase of Eqn. (15)
h, k ,l	Miller index
h	Planck constant (6.63 x 10^{-34} m^2 kg/s)
k^2	HS-LEIS factor
m_1, m_2	masses of the primary ion and scattering surface atom
pX	partial pressure of component X
S	surface area of proton conducting phase of Eqn. (15)
t	time (s) of Eqn. (15)
v	Frequency of radiation (s^{-1})
δ	oxygen non-stoichiometry
λ	wavelength of the incident wave
d	Inter planar crystal lattice spacing (Å)
θ	angle (degrees)
τ_r	Average residence time in the reactor of Eqn. (15)
ϕ	Work function of X-ray photoelectron spectroscopy (XPS)
•	positive charge relative to the lattice in Kröger-Vink notation
′	negative charge relative to the lattice in Kröger-Vink notation
X	no net charge relative to the lattice in Kröger-Vink notation

Abstract

Solid oxide fuel cells (SOFCs) are the promising energy technology to generate electricity from chemical fuel, with no discharge of pollutant. Much effort has been made to enhance the performance of it, while little knowledge regarding anodic reaction of SOFCs is available, still ongoing debating[1-4]; the overall performance of SOFCs is the output originating from multiple kinetic steps, including surface electro-catalysis and bulk ion-electron transport. In this study, H_2/D_2 pulse isotopic exchange experiment is utilized to gain insight into the hydrogen oxidation mechanism in the anode of proton conducting and also oxygen conducting SOFCs, especially, H_2 surface exchange reaction rate on corresponding proton and oxygen conducting electrode materials is determined.

In next chapter, the possibility of a proton conducting ceramic as a support material for catalytic reaction is discussed; non-oxidative ethane dehydrogenation and CO_2 methanation. This study not only shows the potential of proton conducting oxide as support for catalytic reaction, also open new reaction pathways through proton incorporation in the support material[11]. Furthermore, the use of a proton conducting support opens the possibility of creating electrochemical reactors systems for cogeneration of electricity and fuel[12-16]. Hydrogen obtained from alkane dehydrogenation would be utilized as fuel for the proton conducting solid oxide fuel cell with the product olefin generated at the cell anode. Also, hydrocarbon fuel production would be expected via CO_2 methanation in the reverse mode of SOFCs, solid oxide electrolyzer cell.

1. Introduction

1.1 Background and Motivation

Solid oxide fuel cells (SOFCs) are promising technology for the ability to convert the chemical energy to electrical energy, and no discharge of pollutant. The SOFCs fall into two different types by mobile ions: oxygen anions conducting (SOFCs) and protons (H^+-SOFC). In the former structure, oxygen anions transport from cathode to anode through electrolyte membrane[6-8] under high operating temperature, typically > 1073K, originating from the high activation energy for oxygen anion transport[9]. This high operating temperature facilitates the use of inexpensive transition metal catalyst, while it accelerates degradation and increases balance of plant costs. An alternative to reduce operating temperature is to switch mobile ion to proton with lower activation energy for conduction in ceramics. The proton conducting SOFCs results in higher conductivity in the target temperature range, 773-973 K [10-12] where the use of transition metal is still available and the cost and degradation issues arising out of high operating temperature would be potentially mitigated.

This SOFCs technology can be expanded from generating electricity through hydrogen oxidation to producing fuel by electrolysis of water in reverse mode of SOFCs. This solid oxide electrolyser could also be a route to upgrade the SOFC technology to be more renewable and sustainable such as wind and solar power through reproduction of fuel. In addition, this reversibility allows the SOFCs to be promising alternative to meet the fluctuating energy demand, as it enables to store and deliver surplus electrical energy as chemical fuel as needed[13-16].

In recent years, hydrogen energy technology as environmental friendly system is attracting much attention due to the growing environmental concerns such as global warming. For example, when hydrogen is used in fuel cell to generate electricity, the only product is harmless water with

no CO_2 emission[17,18]. In spite of these potentials of hydrogen such as high gravimetric energy density and no carbon emission, the main production method of hydrogen still rely on fossil fuel such as natural gas steam reforming, and the technical barrier and economic limitation regarding generation and distribution restricts the widespread use of hydrogen energy technology[19,20]. Thus synthetic hydrocarbon has been proposed as an alternative to hydrogen energy or new form of hydrogen carrier, offering high H/C ratio and convenient storage and transportation[21,22].

The SOFCs technology also enables to the use of hydrocarbon fuel such as natural gas, methanol, ethanol, and gasoline with internal reformer carried out with SOFCs [23-25], as the operating temperature of SOFCs is in the range of that used in reforming reaction [26]. The integration with reforming system into the SOFCs stack can remove the requirement of the external reformer, leads to the reduction of cost and improved overall efficiency[27,28].

It should be noted that SOFC performance is determined by a combination of many kinetic steps, including surface electro-catalysis and bulk ion-electron transport. Thus, a fundamental understanding of anodic kinetics in SOFCs is necessary to level SOFCs system up to be operated by hydrocarbon fuel, also to produce hydrocarbon fuel in reverse mode of it, electrolyzer.

1.2 SOFC Operation

Solid oxide fuel cells (SOFCs) consist of three main component: an anode, an electrolyte and a cathode. For example, figure 1.1 shows the schematic and operating principle of a proton conducting SOFC. H_2 is dissociated in the anode, generating protons and supplying electrons to the external circuit, equation 1.2.1. The protons then migrate through the electronically insulating, but permitting proton conduction, oxide electrolyte to the cathode. Product water is then formed at the cathode, consuming electrons from external circuit, equation 1.2.2.

Anode $H_2 \rightarrow 2H^+ + 2e^-$ 1.2.1

Cathode $\frac{1}{2} O_2 + 2H^+ + 2e^- \rightarrow H_2O$ 1.2.2

Overall ½ $O_2 + H_2 \rightarrow H_2O$ 1.2.3

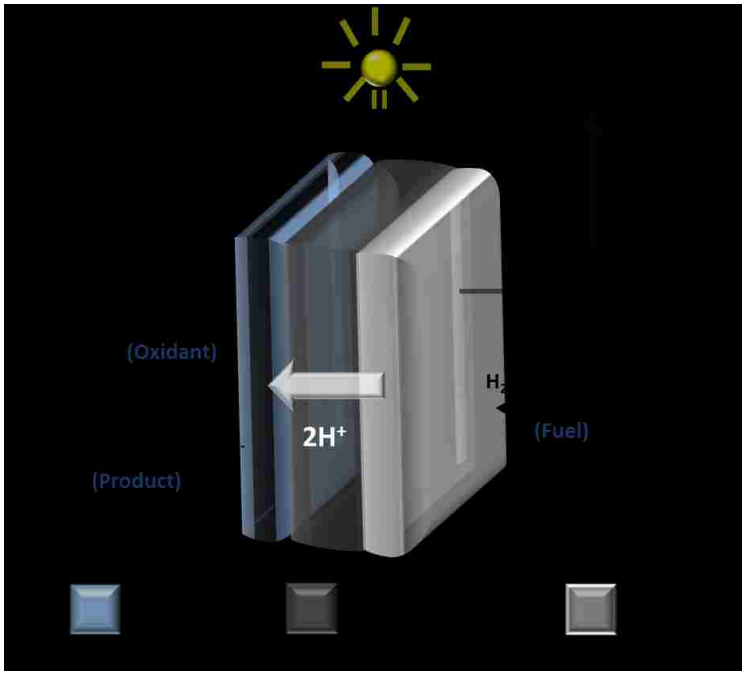

Figure 1.1 Schematic diagram of proton conducting SOFC during operation

The thermodynamic driving force for the SOFC is the electrochemical potential difference for hydrogen across the cell. The maximum theoretical cell potential occurs at open circuit potential (OCP), it is described by the Nernst equation under the condition that the cell is in electrochemical equilibrium and only protons are conducted through the electrolyte, equation 1.2.4 [29].

$$E = \frac{RT}{2F}\ln\left(\frac{pH_{2,anode}}{pH_{2,cathode}}\right) = E_0 + \frac{RT}{2F}\ln\left(\frac{pO_{2,cathode}^{0.5} \cdot pH_{2,anode}}{pH_2O_{cathode}}\right) \quad 1.2.4$$

, where E_0 is the reversible potential, pH_2, pO_2 and pH_2O are the partial pressures at the respective electrodes and R, T and F have their usual meanings. An analogous expression can be written for the theoretical Nernst potential across an oxygen ion conducting electrolyte in H_2 fuel, equation 1.2.5 [30].

$$E = \frac{RT}{4F}\ln\left(\frac{pO_{2,cathode}}{pO_{2,anode}}\right) = E_0 + \frac{RT}{2F}\left(\frac{pO_{2,cathode}^{0.5} \cdot pH_{2,anode}}{pH_2O_{anode}}\right) \quad 1.2.5$$

In this equation, the Nernst potential is the difference in the electrochemical potential of oxygen across the cell. The proton conducting materials can be differentiated from oxygen conducting one through different trend in cell potential with varying hydrogen and oxygen electrochemical potential difference across the cell. For example, the driving force for a pure proton conducting materials is relatively insensitive to small changes in water partial pressure of H_2O/H_2 fed to the cell anode due to a small change in equilibrium pH_2. In contrast, a small change in pH_2O leads to a large change in equilibrium pO_2, which result in significant change in driving force for oxygen ion conductor. For a mixed proton and oxygen ion conducting material, the measured trend will lie in between Proton and oxygen conductor.

One final consideration is the presence of any electronic charge carriers in the electrolyte. These electronic carries, either *p*- or *n*-type, represent an internal 'short' across the membrane, reducing the driving force across the cell. In this case, the cell potential will be offset lower than the predicted Nernst potential, although it will still follow the trend predicted for the primary ionic charge carriers. *p*- and *n*-type conductivity can be differentiated based on trend in total conductivity with increasing or decreasing pO_2, section 1.3.

1.3 Perovskite Oxide and Transport Mechanism

Perovskite-structured oxides have the typical chemical formula of $ABO_{3-\delta}$, where A, B and denotes two different cations respectively and "δ" the oxygen non-stoichiometry. The full stoichiometry of oxygen, δ, occurs when the total positive charge of cations balance the negative charge on three oxygen anions. Figure 1.2 visualizes the structure of ideal cubic perovskite with placing B-site cation in the oxygen octahedral geometry on the corner, A-site cation in center of cube. The perovskite oxides are generally composed of an alkali earth or transition metal for A-site cations and a transition or rare earth metal for B-site cations.

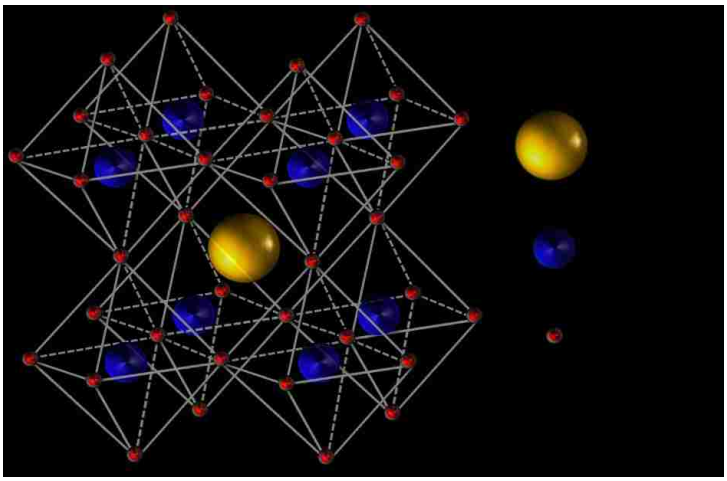

Figure 1.2 Ideal cubic perovskite

The perovskite oxides are the most attractive materials for SOFC application since the oxides exhibit a large variety of properties: electric or ionic conductivity and catalytic activity in regards of several reactions. Furthermore, it offers the structural stability against high temperature, high concentration of dopants on A and B site and oxygen vacancy, influencing on the above mentioned properties of perovskite oxides [31]. The oxygen vacancy formation is function of temperature and *p*O2, as well as formed as the result of the charge compensation required from intrinsically reduction of B-site cations or aliovalent cation doping.

Equation 1.2.6 & 7 are the example of Oxygen vacancy and electronic charge formation in $BaCeO_3$ via reduction of B-site cation and the introduction of aliovalent doping into the B-site cation. Here, Kröger-Vink notation[32] is used to illustrate the point defect in the crystal lattice: X, (•) and (′) are neutral, positive and negative charges relative to the original lattice , respectively.

$$2Ce_{Ce}^{X} + O_{O}^{x} \leftrightarrow 2Ce_{Ce}^{'} + V_{O}^{\bullet\bullet} + 1/2O_2 \qquad 1.2.6$$

$$Y_2O_3 + 2Ce_{Ce}^{X} + O_{O}^{x} \xrightarrow{BaCeO_3} 2Y_{Ce}^{'} + V_{O}^{\bullet\bullet} + 2CeO_2 \qquad 1.2.7$$

Where $Ce_{Ce}^{'}$ and $Y_{Ce}^{'}$ are Ce^{3+} and Y^{3+} on the Cerium lattice site respectively, resulting in net negative charge relative to base lattice. As described in equation 1.2.8, charge compensation can be achieved via two different ways, depending on the environment of the materials. At high *p*O2,

electronic charge formation dominates via the reduction of B-site cations, serves as a negative charge carrier (electron hole). This negative charge results in the internal 'short circuit' in SOFC operation with electronic conduction. In contrast, as pO_2 decreases, the electronic conductivity decreases, the charge compensation mechanism is shifted to oxygen vacancy formation. The concentration of the oxygen vacancy can be further increased by introduction of aliovalent dopant, equation 1.2.7.

In contrast to the case of B-site cation with a mixed valence state in above example, perovskite oxide with fixed valence state of B-site cation forms *p*-type conduction at the expense of electrons, associated with transport of electron holes, Equation 1.2.8.

$$1/2O_2 + 2V_O^{\bullet\bullet} \leftrightarrow O_O^x + 2h^{\bullet} \qquad 1.2.8$$

This hole formation mechanism dominates at high oxygen partial pressures. At high pO_2 the concentration of holes increases, while the concentration of electrons decreases. In wet atmosphere, this hole can be existed in proton as electron holes are consumed upon water incorporation, equation 1.2.9.

$$H_2O_{(g)} + 2h^{\bullet} \leftrightarrow 1/2O_2 + H^{\bullet} \qquad 1.2.9$$

This oxygen vacancy also plays an important role for ionic conduction since it offers the route for oxide ion conduction though hoping mechanism from their original site to adjacent oxygen vacant site, proton formation occurs through the incorporation of water on oxygen vacant site, equation 1.2.10. In addition, the proton formation reaction can be simply described as incorporation of H_2, equation 1.2.11. Protons in oxides are stabilized by the electron density of nearby oxygen ions and the incorporated proton may be considered as hydroxide ions on an oxide ion sites, $OH_O^{\bullet}$ in Kröger-Vink notation[10,10,33].

$$H_2O_{(g)} + V_O^{\bullet\bullet} + O_O^x \leftrightarrow OH_O^{\bullet} \qquad 1.2.10$$

or as incorporation of H_2

$$H_{2(g)} + 2O_O^x \leftrightarrow 2OH_O^\bullet + 2e^- \qquad 1.2.11$$

Considering this first reaction, the proton concentration may be determined by the concentration of oxygen vacancies. On the other hand, protons might be dissolved to compensate the dopants during synthesis of the oxides, so vacancies might not be the prerequisite for protons. In addition, oxygen vacancies are competing with the formation of protons; dry reducing gases favor oxygen vacancy formation while humidification and high pH_2 favor proton incorporation. Proton conduction occurs via hopping of a proton between oxide ions (the so called Grotthuss mechanism), as well as rotational motion of the hydroxyl unit, figure 1.3 [10].

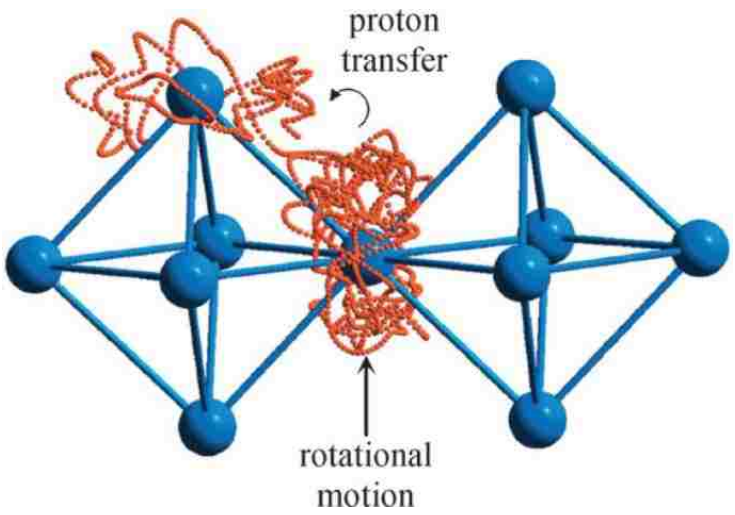

Figure 1.3 Trace of proton (orange): rotational motion and proton transfer[10]

1.4 Hydrogen Oxidation

Anodic reaction in SOFCs consists of multiple steps; gas diffusion of reactant and product, adsorption and desorption of species, surface diffusion of adsorbed species and intermediates, charge transfer between solid phases, and catalytic and electro-catalytic reaction step. It is commonly accepted that fuel oxidation occurs at the TPD (triple phase boundary) between electrode, electrolyte and gas phase[34]. In case of Ni/YSZ, the fuel is oxidized in anode, the liberated electron flows through external circuit to cathode. The oxygen anion transported through electrolyte to active site reacts with hydrogen adsorbed on Ni to form water, diffuses out

of the anodes [34]. In contrast to the common concept, the details of hydrogen oxidation kinetics in the SOFC anodes was not identified in working device due to the complicated microstructure of cermet anode and convoluted impedance measurement method.

Possible anodic reaction pathways for H_2 oxidation was supposed by Bessler et al, as shown in figure 1.4[35]: (a) hydrogen spillover from Ni surface to either oxygen ion or hydroxyl ion on YSZ surface, (b) Charge transfer reaction with and without oxygen ion spillover from YSZ to Ni, (c) hydroxyl spillover from YSZ surface to Ni surface, (d) charge transfer reaction by hydrogen interstitial, (e) all charge transfer and chemical reaction occurring only on YSZ surface. Many efforts has been made to elucidate the anodic reaction mechanism with the combination of experimental and simulation results, while there are still ongoing debates regarding fuel oxidation mechanism, in addition, even where fuel oxidation reaction starts is not clear[4].

Mizusaki et al.[3,36] utilized Ni electrodes micro-patterned on YSZ surface to resolve the complexity of cermet anode structure, clearly identified that the hydrogen oxidation reaction in the Ni, H_2-H_2O system occurs around TPB through almost linear relationship between the TPB length and electrode conductivity (defined as the inverse of area specific resistance). Furthermore, they reported the dependence of electrode conductivity on pH_2 and pH_2O, indicating that the rate determining step is either a dissociative adsorption of hydrogen or surface diffusion of adsorbed species on Ni surface, with the independence of open YSZ surface area.

In contrast, the simulation results by Goodwin et al.[37], where three alternative reaction pathways (Oxygen spillover from YSZ surface to Ni surface, hydrogen spillover from Ni surface to YSZ surface through a single channel & dual channel) were considered, showed that the experimental results of Mizusaki et al.[3,36] can be explained by hydrogen spillover mechanism. Furthermore, de Boer[4] proposed a charge transfer process, including proton incorporation with oxygen in the bulk oxide and protonation of adsorbed hydroxide ions to form water as rate determining step.

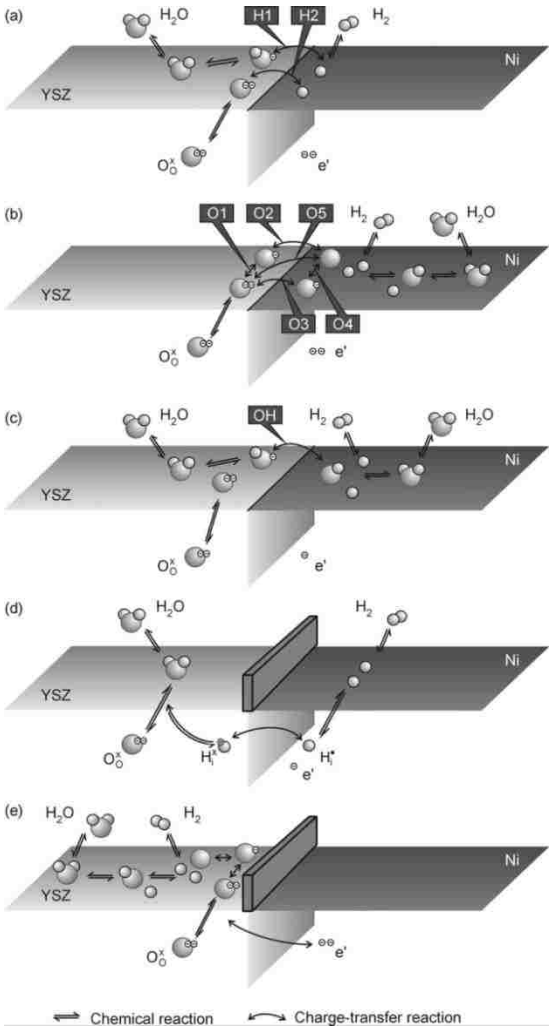

Figure 1.4 Possible anodic reaction pathway at a Ni/YSZ TPB (a-e) [35]

Similar research works as Mizusaki et al.[3,36] were reported by Bieberle et al[38], where not only micro patterned electrode, but modeling and simulation approach were utilized to study anode kinetics in Ni, H_2-H_2O system. They also observed the dependence of electrode conductivity on the length of TPB and kinetic enhancement in the increase of pH_2O. Their simulation results fitted with experimental data indicates that the rate determining step might be not only the adsorption /desorption of hydrogen but also the removal of O^{2-} from electrolyte. This experiment was reviewed by Bessler et al. [1] with several possible reaction pathways, described in figure 1.4, proposed two rate determining step according to temperature: while the reaction rate is limited by

the spillover of hydrogen from Ni surface to hydroxyl ions on YSZ at low temperature, this is co-limited by the spillover of hydrogen to oxygen ions on the YSZ surface, hydroxyl diffusion on there and H_2O desorption from YSZ at high temperature. As above mentioned, most of proposed reaction mechanisms were obtained from the deconvolution and fitting of electrochemical impedance data under varying operation environments, modeling and simulation study, further experiments are required to get direct measurement of anodic reaction in SOFCs.

1.5 Material Choice

The electrolyte materials for SOFC application require several properties: 1) high ionic conductivity, 2) low electronic conductivity, 3) stability under oxidizing and reducing environments and 4) compatibility with high concentration of dopant to enhance the conductivity and stabilit[4]y [31,33,34].

From this point of view, perovskite structured alkaline cerates and zirconates are the most candidates for proton conducting electrolyte for H^+-SOFC application[39]. Iwahara and coworkers [16,40] reported the excellent proton conductivity of $SrCeO_3$ and $BaCeO_3$, and the conductivity enhancement through aliovalent doping (Y and Yb) in the host. In contrast, these cerates have very low stability due to decomposition to carbonates in low CO_2 and to hydrates at high water activities, equation 1.2.12 & 13 [41].

$$BaCeO_3 + H_2O \rightarrow Ba(OH)_2 + CeO_2 \qquad 1.2.12$$

$$BaCeO_3 + CO_2 \rightarrow BaCO_3 + CeO_2 \qquad 1.2.13$$

The weakness on stability might be challenging on a real SOFC application. Haile and Iwahara reported that $BaCeO_3$ can be stabilized by the substitution of zirconium for cerium on the B-site, $BaCe_{1-x}Zr_xO_{3-\delta}$ [42,43]; however, these oxides normally require very high sintering temperature to make dense ceramics. Tao and Irvine[44,45] found that the addition of ZnO can significantly reduce the sintering temperature of Y_2O_3 doped-$BaZrO_3$ from 1700 to 1325 ^oC, the similar effect was

also reported by Haile group[46]. Furthermore, Azimova and McIntosh[29] reported the sintering temperature can be reduced by Cobalt doping, while high concentration of cobalt doping leads to electronic conductivity and chemical instability.

The series of $BaCe_{1-x}Zr_{1-y}(Yb,Y)_YCo_xO_{3-\delta}$ can be chosen as ultimate electrolyte candidate for proton conducting SOFC application, while $BaCeO_3$ (BC), $BaCe_{0.9}Y_{0.1}O_{3-\delta}$ (BCY), $BaZrO_3$ (BZ) and $BaZr_{0.9}Y_{0.1}O_{3-\delta}$ (BZY) are chosen to explore the effect of B-site cations, dopants and the oxygen vacancy on the kinetics in $BaCe_{1-x}Zr_{1-y}(Yb,Y)_YCo_xO_{3-\delta}$. Furthermore, supported transition metal catalyst on $BaZrO_3$ (M/BZ, M= Co, Pt, Ni and Cu) are examined to study the kinetics on transition metal in porous ceramic-metallic (cermet) structure of working device.

This perovskite structured oxides are also considered as candidates for oxygen conducing electrolyte due to their various advantages as above mentioned, while, van Gool supposed that the closed packing structure from A and O in ABO_3 might make oxygen transport difficult[47]. In addition, the perovskite structure very often exhibits p-type electronic conduction under oxidizing atmosphere such as air at elevated temperature. CaTiO3 and SrTiO3 based solution are the typical example where electronic conduction (p-type and n-type in high and low pO_2, respectively), deriving mixed ionic conduction [48].

Fluorite type oxides, consisting of tetravalent cations, are considered as an alternative material for oxygen conducting electrolyte since the electronic conduction is rarely observed in many fluorite-type oxide under very high oxygen activity (eg. pO_2=1). Furthermore, they exhibit significantly high oxygen ion conduction. Fluorite type structure is a face centered cubic arrangement of cations, with anions occupying all the tetrahedral sites. The most widely used electrolyte materials in the fluorite group are stabilized zirconates (Y_2O_3-ZrO_2) and doped ceria. Thus we have chosen these two electrolyte materials for this kinetic study in oxygen conducting SOFC anode, along with supported transition metal on both oxide (M= Pt, Ni and Cu, denoted M/YSZ or GDC and M in the following).

1.6 Powder Synthesis

There are several synthesis methods in the field of solid state chemistry, the most common one is the ceramic method (or called solid state reaction method). The procedure consists of grinding of stoichiometric amount of the corresponding starting raw compounds and then sintering at relatively high temperature and longer dwelling time. Furthermore, this method demands repeated procedure due to the low homogeneity of the obtained product.

As more efficient method, the sol-gel method are used more and more frequently since the technique enable pure material synthesis at lower sintering temperature compared to ceramic methods. The most obvious advantage is that the reagents are mixed in atomic level, leading the higher reaction rate and decreased sintering temperature. The starting material is colloidal solution (called sol) that acts as the precursor for an integrated network (called gel) of either discrete particles or network polymer. This technique is also available for perovskites synthesis with oxide or salts of the metals, being dissolved in the solution containing complexing agent (citric acid, e.g.). The solution then heat up to form gel and subsequently organic part is decomposed by heating, leading the formation of fine and even distribution of different metal in the resulting powder[49].

Similar method was developed by Pechini in 1967 to prepare precursor polymeric resin. A mixture of cations of corresponding starting materials is formed in organic complexing agent (citric acid or ethlyenediaminetetraacetic acid, EDTA) and glycol solution. The cations become a chelate, and formed polymer resin is then decomposed at 573K. Here, glycol solution plays a role to reduce the segregation of the cations through polymerization process[50]. In this study, the modified pechini method without glycol has been chosen.

1.7 X-Ray Diffraction

X-ray diffraction (XRD) is the most important characterization tool in solid state chemistry and material science since many solid state reaction produce polycrystalline powder to have the unique x-ray diffraction pattern, which can be used for finger print characterization of crystalline material and determination of their crystal structure.

When X-rays are incident on an atom, the electronic cloud moves like any electromagnetic waves. These movements of them re-radiate the wave with the same frequency (blurred slightly due to a variety of effects). These re-emitted wave interfere with each other either constructively or destructively (overlapping waves either add together to produce stronger peaks or subtract from each other to some degree), the overlapped waves produce diffraction pattern. This is Bragg's analysis, equation 1.2.14, where *n* is an integer, λ is the wavelength of the incident wave, *d* is the spacing between the planes in the atomic lattice, and θ is the angle between the incident ray and the scattering planes.

$$n\lambda = 2d \sin\theta \qquad 1.2.14$$

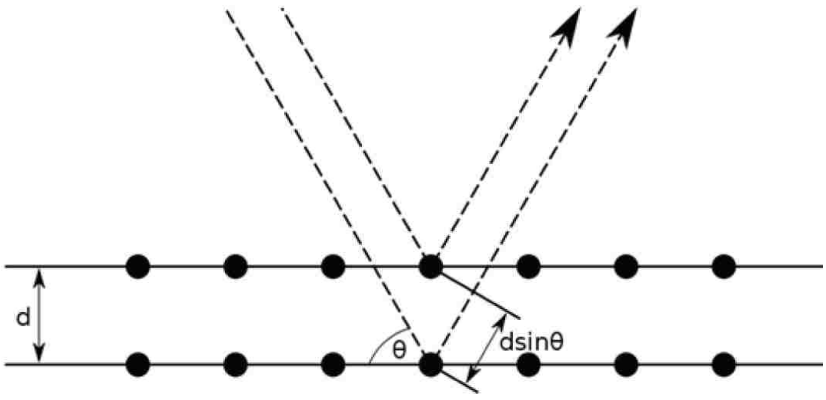

Figure 1.5 Bragg's diffraction

The possible d-spacing defined by the indices *h, k,* and *l* are determined by the shape of the unit cell. Therefore, the possible 2θ values where we have reflection are determined by the unit cell dimensions.

1.8 H2/D2 pulse isotope exchange experiments

As described in sec 1.4, the hydrogen oxidation reaction mechanism and also rate determining step in anodic reaction of SOFC is still obscured, most of proposed conclusion regarding it go on the convoluted electrochemical impedance data and computational modeling and simulation followed by the fitting it with experimental result due to the complicated structure of cermet anodes[1-4,36,37]. Thus, our goal is to obtain the insight in to the hydrogen oxidation mechanism in SOFC anodes through hydrogen surface exchange reaction on electrode materials.

The most representative technique used in heterogeneous catalysis research is transient study since the experiment is performed under transient condition, provides the mechanistic and kinetic information about catalytic reaction. This technique can be classified into two main groups by thermodynamic state change of system: one method to transform the thermodynamic state of system to another one such as TPD and concentration jump method, and another method to remain thermodynamic state of system before and after transient state like state isotopic transient kinetic analysis technique (SSITKA). In the latter case, isotope labeled reactant is employed to obtain reaction pathway and determine reaction mechanism trough replacement of reactant by isothermal switching between streams containing different isotopic labeled counterpart. While these techniques require numerical modeling to analyze the kinetic data as a function of the time on stream and great care to avoid artifacts and errors into the kinetic parameter[57-59].

For rapid evaluation of surface exchange reaction and mechanism, Bouwmeester[60] introduced the pulse isotopic exchange technique, where labeled oxygen isotope reactant was used, the surface oxygen exchange reaction rate of oxide ion conductor was determined to identify candidate materials for SOFC and oxygen transport membrane application.

In this study, the pulse H_2/D_2 isotopic exchange experiment is utilized to evaluate the hydrogen surface exchange reaction rate of proton conducting oxide for H^+-SOFC application, where the determined surface exchange reaction rate offers the insight into hydrogen oxidation

mechanism in H^+-SOFC anodes, the schematic diagram is illustrated in appendix 1. A pulse of D_2/Ar is injected into a stream of H_2/Ar over a powder sample of the material with same partial pressure of each stream to maintain chemical equilibrium. During a pulse, H atoms on the surface and some fraction of the protons in the bulk exchange with D_2 from the gas phase.

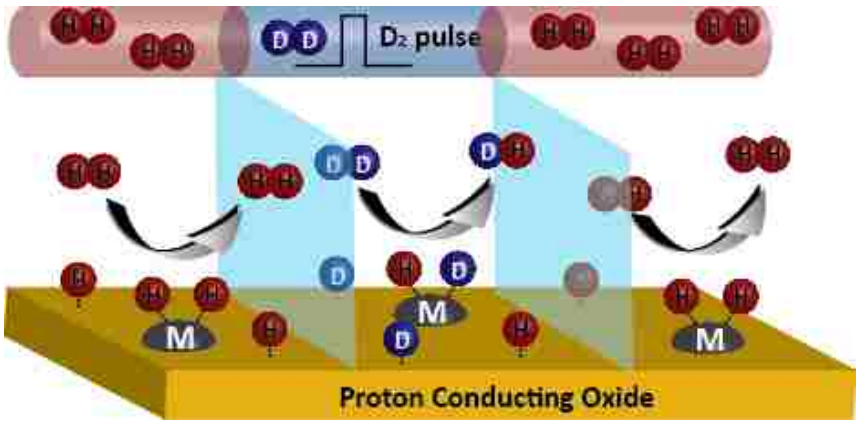

Figure 1.6 schematic representation of pulse H2/D2 isotopic exchangereaction

The surface exchange reaction rate is determined through the quantification of the D_2 consumption in active pulse, following the method that Bouwmeester and coworkers used to ^{18}O-^{16}O exchange[60]. It should be noted that the calculated surface exchange reaction rate represents overall surface exchange reaction rate, *R*o (mol D $\cdot m^{-2} \cdot s^{-1}$), which is assumed to be first order reaction, although we can hypothesize hydrogen incorporation mechanism includes dissociative adsorption of H_2, charge transfer of electrons, and finally proton incorporation with oxygen ion in the oxide.

$$n\frac{\partial f_g}{\partial t} = -Ro \cdot S(f_g - f_o) \qquad 1.2.15$$

Where the overall surface exchange reaction rate is normalized the total surface area, S, of the proton conducting phase, and f_g and f_o are the fraction of deuterium isotope in the gas and oxide phase respectively. It is assumed, and demonstrated in our work, that the bulk and gas-phase

diffusion are negligible. Therefore, the surface exchange reaction rate is calculated with the conversion of D_2 in a reactive pulse under the assumption of the ideal plug flow reactor:

$$\mathrm{Ro} = \frac{\mathrm{n}}{\mathrm{S} \cdot \tau_{\mathrm{r}}} \ln \frac{\mathrm{f}_{\mathrm{g,i}}}{\mathrm{f}_{\mathrm{g,e}}} \qquad 1.2.16$$

In the eqn. 16, τ_r represents the average residence time in the reactor, $f_{g,i}$ and $f_{g,e}$ is the D_2 isotope volumetric fraction in the pulse at the inlet and exit of the reactor, respectively.

The sample size is designed to minimize the influence of bulk ionic transport, it is ensured that the system follows plug flow reactor behavior with no change in reaction rate with reactant flow rate, indicating facile gas phase transport across the stagnant gas boundary layer exterior to the particle. Furthermore, the effect of water on the surface exchange reaction was examined, the sample were equilibrated in wet H_2 at measurement temperature prior to the injection of dry D_2.

1.9 Surface Investigation: High Sensitivity-Low Energy Ion Scattering (HS-LEIS) & X-Ray Photoelectron Spectroscopy (XPS)

The outmost surface investigation is the most important in the fundamental study of heterogeneous catalysis since the reaction takes place on the outermost atomic layer of solid catalyst. Low Energy Ion Scattering (LEIS) is unique analytical tool that provides quantitative compositional information about the outermost atomic layer of a material, while the damage to the sample by the incident ions restricts the widespread application of LEIS. The development of HS-LEIS resolved the issue to damage the materials through the use of such low ion doses, further improved the mass resolution.

Figure 1.7 shows the principle behind HS-LEIS technique. A noble gas ion with a known primary energy E_i is incident on the surface of the materials. The incident ion beam is perpendicular to the surface, collides with an atom on the surface.

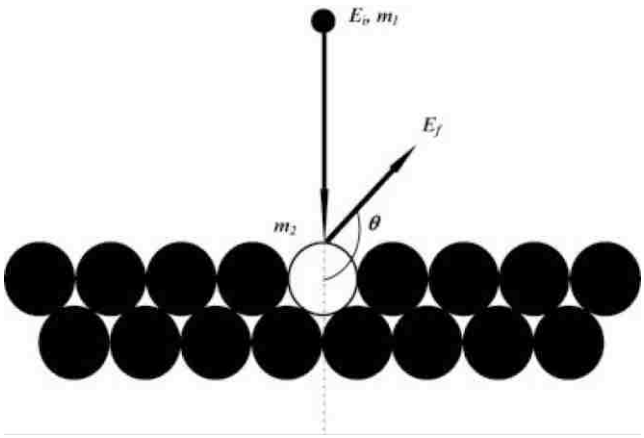

Figure 1.7 Schematic representation of the ion scattering process.

The energy of the backscattered ion (E_f) is determined by the classic laws of mechanics (conservation of momentum and conservation of energy) and is given by

$$E_f = k^2 \left(\frac{m_2}{m_1}, \theta\right) E_i \qquad 1.2.17$$

m_1 and m_2 are the masses of the primary ion and scattering surface atom, respectively, with θ indicating the back scattering angle (determined by the geometry of the instrument). In the HS-LEIS experiment, θ, m_1 and E_i are known and E_f is measured with a dedicated energy analyzer. The factor k^2 is a known function of m_2/m_1 and θ. The k^2 function increases monotonously from 0 for $m_2/m_1 = 1$ to 1 for $m_2/m_1 \rightarrow \infty$ (if $\theta > 90°$). Thus, the mass of the scattering surface atom can be calculated from equation 1.2.17. In the HS-LEIS measurement, different primary ions ($^4HE^+$, $^{20}Ne^+$ and $^{40}Ar^+$) can be chosen to achieve high mass resolution and meet the sensitivity of surface atom[61].

The comparable technique to HS-LEIS is the XPS, offering the information at the depth of several nanometer (~20 layers), while HS-LEIS is suited for the analysis of the outermost atomic layer. XPS provides not only surface compositional information, but chemical state, variation of composition by depth, variation of chemical composition spatially on the surface and thickness of layers. The XPS measurement is performed with irradiation of x-ray on materials under ultra-high

vacuum condition, the number of photo electron generated by a given element result in a discrete peaks. The kinetic energy, E_k, of these photoelectrons is determined by the energy of the x-ray radiation, hv, and the electron binding energy, E_b,

$$E_k = hv\text{-}E_b \qquad 1.2.18$$

The experimentally measured energies of photoelectrons are given by

$$E_k = hv\text{-}E_b\text{-}\phi \qquad 1.2.19$$

Where h, v and ϕ denotes planck constant, frequency of the radiation and work function of spectrometer. All of the information in the XPS spectrum (photoelectron lines, shifts in peak positions, the splitting of a peak due to electrons of different spins, valence band electron lines and Auger lines) can be utilized to obtain the compositional information of a surface[62].

1.10 References

1. Bessler, W. G.; Vogler, M.; Stormer, H.; Gerthsen, D.; Utz, A.; Weber, A.; Ivers-Tiffee, E. *Phys. Chem. Chem. Phys.* **2010***, 12*, 13888-13903.

2. Bieberle, A.; Gauckler, L. J. *Solid State Ionics* **2002***, 146*, 23-41.

3. Mizusaki, J.; Tagawa, H.; Isobe, K.; Tajika, M.; Koshiro, I.; Maruyama, H.; Hirano, K. *Journal of The Electrochemical Society* **1994***, 141*, 1674-1683.

4. Boer, B. d. SOFC Anode Hydrogen oxidation at porous nickel and nickel/yttriastabilised zirconia cermet electrodes, 1998.

5. Dorner, R. W.; Hardy, D. R.; Williams, F. W.; Davis, B. H.; Willauer, H. D. *Energy Fuels* **2009***, 23*, 4190-4195.

6. Stambouli, A. B.; Traversa, E. *Renewable and Sustainable Energy Reviews* **2002***, 6*, 433-455.

7. Yamamoto, O. *Electrochim. Acta* **2000***, 45*, 2423-2435.

8. Steele, B. C. H. *Journal of Materials Science* **2001***, 36*, 1053-1068.

9. Carter, S.; Selcuk, A.; Chater, R. J.; Kajda, J.; Kilner, J. A.; Steele, B. C. H. *Solid State Ionics* **1992***, 53–56, Part 1*, 597-605.

10. Kreuer, K. D. *Annu. Rev. Mater. Res.* **2003***, 33*, 333-359.

11. Norby, T. *Solid State Ionics* **1999***, 125*, 1-11.

12. Dicks, A. L.; Fellows, R. G.; Martin Mescal, C.; Seymour, C. *J. Power Sources* **2000***, 86*, 501-506.

13. Iwahara, H.; Asakura, Y.; Katahira, K.; Tanaka, M. *Solid State Ionics* **2004***, 168*, 299-310.

14. Iwahara, H. *Solid State Ionics* **1996***, 86–88, Part 1*, 9-15.

15. Iwahara, H.; Uchida, H.; Morimoto, K.; Hosogi, S. *Journal of Applied Electrochemistry* **1989***, 19*, 448-452.

16. Iwahara, H.; Esaka, T.; Uchida, H.; Maeda, N. *Solid State Ionics* **1981***, 3–4*, 359-363.

17. Sakai, T.; Matsushita, S.; Matsumoto, H.; Okada, S.; Hashimoto, S.; Ishihara, T. *Int J Hydrogen Energy* **2009***, 34*, 56-63.

18. He, F.; Song, D.; Peng, R.; Meng, G.; Yang, S. *J. Power Sources* **2010***, 195*, 3359-3364.

19. Song, C. *Catalysis Today* **2006***, 115*, 2-32.

20. Midilli, A.; Dincer, I. *Int J Hydrogen Energy* **2008***, 33*, 4209-4222.

21. - Xie, K.; - Zhang, Y.; - Meng, G.; - Irvine, J. T. S. - *J. Mater. Chem.* , - 195.

22. - Xie, K.; - Zhang, Y.; - Meng, G.; - Irvine, J. T. S. - *Energy Environ. Sci.* , - 2218.

23. Assabumrungrat, S.; Pavarajarn, V.; Charojrochkul, S.; Laosiripojana, N. *Chemical Engineering Science* **2004***, 59*, 6015-6020.

24. Assabumrungrat, S.; Sangtongkitcharoen, W.; Laosiripojana, N.; Arpornwichanop, A.; Charojrochkul, S.; Praserthdam, P. *J. Power Sources* **2005***, 148*, 18-23.

25. Herring, J. S.; O'Brien, J. E.; Stoots, C. M.; Hawkes, G. L.; Hartvigsen, J. J.; Shahnam, M. *Int J Hydrogen Energy* **2007***, 32*, 440-450.

26. Arpornwichanop, A.; Patcharavorachot, Y.; Assabumrungrat, S. *Chemical Engineering Science* **2010***, 65*, 581-589.

27. Fellows, R. *J. Power Sources* **1998***, 71*, 281-287.

28. Aguiar, P.; Chadwick, D.; Kershenbaum, L. *Chemical Engineering Science* **2002***, 57*, 1665-1677.

29. Azimova, M. A.; McIntosh, S. *Solid State Ionics* **2009***, 180*, 160-167.

30. McIntosh, S.; Gorte, R. J. *Chem. Rev.* **2004***, 104*, 4845-4865.

31. Ishihara, T., Ed.; In *Perovskite oxide for solid oxide fuel cells;* Springer: Dordrecht, 2009; .

32. Yashima, M.; Tsuji, T. *Journal of Applied Crystallography* **2007***, 40*, 1166-1168.

33. Norby, T.; Wideroe, M.; Glockner, R.; Larring, Y. *Dalton Trans.* **2004**, 3012-3018.

34. Jiang, S. P.; Yan, Y.; Lu, M., Eds.; In ***Materials for High-Temperature Fuel Cells****;* Wiley: USA, 2013; .

35. Vogler, M.; Bieberle-Hütter, A.; Gauckler, L.; Warnatz, J.; Bessler, W. G. *Journal of The Electrochemical Society* **2009***, 156*, B663-B672.

36. Mizusaki, J.; Tagawa, H.; Saito, T.; Kamitani, K.; Yamamura, T.; Hirano, K.; Ehara, S.; Takagi, T.; Hikita, T.; Ippommatsu, M.; Nakagawa, S.; Hashimoto, K. *Journal of The Electrochemical Society* **1994***, 141*, 2129-2134.

37. Goodwin, D. G.; Zhu, H.; Colclasure, A. M.; Kee, R. J. *Journal of The Electrochemical Society* **2009***, 156*, B1004-B1021.

38. Bieberle, A.; Meier, L. P.; Gauckler, L. J. *Journal of The Electrochemical Society* **2001***, 148*, A646-A656.

39. Norby, T. *Solid State Ionics* **1999***, 125*, 1-11.

40. Iwahara, H.; Uchida, H.; Ono, K.; Ogaki, K. *Journal of The Electrochemical Society* **1988***, 135*, 529-533.

41. Scholten, M. J.; Schoonman, J.; van Miltenburg, J. C.; Cordfunke, E. H. P. *Thermochimica Acta* **1995***, 268*, 161-168.

42. Ryu, K. H.; Haile, S. M. *Solid State Ionics* **1999***, 125*, 355-367.

43. Katahira, K.; Kohchi, Y.; Shimura, T.; Iwahara, H. *Solid State Ionics* **2000***, 138*, 91-98.

44. Tao, S.; Irvine, J. T. S. *Journal of Solid State Chemistry* **2007***, 180*, 3493-3503.

45. Tao, S.; Irvine, J. T. S. *Adv Mater* **2006***, 18*, 1581-1584.

46. Babilo, P.; Haile, S. M. *J Am Ceram Soc* **2005***, 88*, 2362-2368.

47. Gool, W. v. *Philips Res. Rep.* **1965***, 20*, 81.

48. TAKAHASHI, T.; IWAHARA, H. *Energy Conversion* **1971***, 11*, ix.

49. Zakhariev, Z., Ed.; In ***Polycrystalline Materials - Theoretical and Practical Aspects****;* InTech: USA, 2012; .

50. Vaqueiro, P.; López-Quintela, M. A. *Chem. Mater.* **1997***, 9*, 2836-2841.

51. Iablokov, V.; Beaumont, S.; Alayoglu, S.; Pushkarev, V.; Specht, C.; Gao, J.; Alivisatos, A. P.; Kruse, N.; Somorjai, G. A. *Nano Lett.* **2012***, 12*, 3091-3096.

52. Wang, C.; Daimon, H.; Lee, Y.; Kim, J.; Sun, S. *J. Am. Chem. Soc.* **2007***, 129*, 6974-6975.

53. H. E. van Doorn, R.; Kruidhof, H.; Nijmeijer, A.; Winnubst, L.; J. Burggraaf, A. *J. Mater. Chem.* **1998***, 8*, 2109-2112.

54. Shin, H. H.; McIntosh, S. *J. Mater. Chem. A* **2013***, 1*, 7639.

55. Vogel, A. *Textbook of Quantitative Inorganic Analysis;* Longman Scientific and Technical: Longman, Harlow, United Kingdom, 1986; .

56. Levy, P.; Primet, M. *Applied Catalysis* **1991***, 70*, 263-276.

57. Sadovskaya, E. M.; Ivanova, Y. A.; Pinaeva, L. G.; Grasso, G.; Kuznetsova, T. G.; Veen, A. v.; Sadykov, V. A.; Mirodatos, C. *J. Phys. Chem. A* **2007***, 111*, 4498-4505.

58. Kan, C. C.; Kan, H. H.; Van Assche, F. M.; Armstrong, E. N.; Wachsman, E. D. *Journal of The Electrochemical Society* **2008***, 155*, B985-B993.

59. De Souza, R. A.; Chater, R. J. *Solid State Ionics* **2005***, 176*, 1915-1920.

60. Bouwmeester, H. J. M.; Song, C.; Zhu, J.; Yi, J.; van Sint Annaland, M.; Boukamp, B. A. *Phys. Chem. Chem. Phys.* **2009***, 11*, 9640-9643.

61. ter Veen, H. R. J.; Kim, T.; Wachs, I. E.; Brongersma, H. H. *Catalysis Today* **2009***, 140*, 197-201.

62. Conners, T. E.; Banerjee, S., Eds.; In ***Surface Analysis of Paper****;* CRC Press LLC: USA, 1995; .

2. On H_2/D_2 Isotopic Exchange Rate of Proton Conducting Barium Cerates and Zirconates

2.1 Introduction

As stated in Chapter 1, Solid oxide fuel cells (SOFCs) are considered as an important alternative technology for the direct and efficient conversion of chemical to electrical energy. The distinguishing feature of traditional SOFCs is their mode of operation: oxygen anion transport from the cathode to the anode through a dense ceramic electrolyte[1-3]. While their high operating temperature, typically > 1073K and originating from the high activation energy for oxygen anion transport[4], allows the use of inexpensive transition metal catalysts, it accelerates degradation and increases balance of plant costs. One route towards reduced operating temperature is to shift from oxygen anion to proton conducting solid oxide fuel cells(H^+-SOFCs). The lower activation energy for proton conduction in ceramics results in higher conductivity in the target temperature range, 773-973 K [5-7]. Operating in this range would maintain the use of transition metal catalysts, while potentially avoiding some of the cost and degradation issues at higher temperature.

Like this, most prior research into SOFC has focused on enhancing electrolyte conductivity in [8-11], with little knowledge available regarding hydrogen or water dissociation kinetics. SOFC performance is determined by a combination of many kinetic steps, including surface electrocatalysis and bulk ion-electron transport. Recent work by Sun at al [12] indicates that H_2 dissociation is the rate limiting step for H_2 oxidation on patterned Pt-$BaZr_{0.1}Ce_{0.7}Y_{0.1}Yb_{0.1}O_{3-\delta}$. In this work we utilize H_2/D_2 pulse isotope exchange experiments to quantify the H_2 surface exchange reaction on proton conducting electrolyte materials $BaCeO_3$ (BC), $BaCe_{0.9}Y_{0.1}O_{3-\delta}$ (BCY), $BaZrO_3$ (BZ) and $BaZr_{0.9}Y_{0.1}O_{3-\delta}$ (BZY), and Co, Pt, Ni, and Cu on $BaZrO_3$ (M/BZ, M= Co, Pt, Ni and Cu) under dry anode conditions.

2.2 Experimental

$BaCeO_3$ (BC), $BaCe_{0.9}Y_{0.1}O_{3-\delta}$ (BCY), $BaZrO_3$ (BZ) and $BaZr_{0.9}Y_{0.1}O_{3-\delta}$ (BZY) powder were synthesized utilizing a modified Pechini method [13], chapter 1.6. Supported Co, Pt, Ni, Cu on $BaZrO_3$ catalyst (M= Co, Pt, Ni and Cu, denoted M/BZ in the following) were fabricated using the incipient wetness impregnation procedure[14]. Aqueous solutions of Ni, Cu (>99% pure, Sigma St. Louis, MO, USA), and Co (>99% pure, Acros Organics, New Jersey, USA) were prepared, and the concentration determined by redox titration. Platinum chloride (98% pure, Alfa Aesar, Ward Hill, MA, USA) was dissolved in ammonium hydroxide to form a 1.25mM solution. 1 wt% of each metal added to BZ powder. After drying at 100 ^oC for 10h, the powders were calcined in air at 500 ^oC for 10h. These powders were then reduced under flowing hydrogen at 800 ^oC for 2h.

The synthesized materials were characterized by powder X-ray diffraction with Cu Kα radiation and fixed slit width (MiniFlex (II), Rigaku, The Woodlands, TX, USA). Diffraction patterns were recorded in the 2θ-range of 20^o-70^o with a step size of 0.02^o and a counting time of 0.2 min/degree. Rietveld structural refinement was carried out using the GSAS package with the EXPGUI interface[15]. The BET surface area (ASAP2020, micrometrics, Norcross, GA, USA) was measured using N_2 gas as the absorbent after samples were degassed at 300 ^oC for 10h. SEM was performed using a field emission scanning electron microscope (Hitachi 4300 SE/N Schottky Field Emission, Tokyo, Japan). Prior to measurement, the samples were oxidized to remove surface contaminants at 800 ^oC for one hour in a flow of 50mL/min 19.5 – 23.5 vol% O_2/N_2 (GTS-Welco, Allentown, PA,USA), and then reduced at 800^oC under flowing 3 vol% H_2O / 5 vol% H_2 / Ar (UHP gases, < 1ppm O_2, GTS-Welco, Allentown, PA, USA) for one hour followed by reduction at 400 ^oC in a flow of 50mL/min 5 vol % H_2 / Ar.

The surface cations stoichiometry was determined by a combination of high sensitivity low Energy Ion Scattering (HS-LEIS, QTAC[100], Chestnut Ridge, NY, USA) and X-ray photoelectron spectra (Scienta ESCA-300). The surface pre-treatment was performed in the same way as for the

SEM characterization. HS-LEIS measurements were first conducted with a series of low doses of 4 keV Ne^+ to determine surface composition (1.03×10^{15} ions/cm^2, on BZ, BaO_2, ZrO_2, BZY and Y_2O_3). This was followed by a higher dose density of 2 keV Ar^+ to create a depth profile (4.7×10^{16} ions/cm^2 with total ion dose density of 1.76×10^{18} ions/cm^2). Further surface investigation was performed with an even lower ion dose on a different part of the sample ; 4 keV Ne^+ (1.65×10^{14} ions/cm^2) with 2 keV Ar^+ (9.5×10^{14} ions/cm^2) sputtering dose with a total ion dose density of 8.6×10^{15} ions/cm^2. This second set of conditions was utilized to minimize the surface damage from ion dose and probe the outermost surface.

X-ray photoelectron spectra measurements were performed to investigate the surface composition of BC and BCY, the spectra were obtained on a Scienta ESCA-300 with monochromatic X-ray (beam spot, 5mm × 1mm) generated by Al Kα source (E = 1486 eV). The residual pressure of the analysis chamber was < 1×10^{-8} Torr.

The H_2/D_2 isotopic exchange reaction rate was determined using the pulse experimental setup. Quartz glass wool was used to hold the 10mg powder samples diluted with $SrTiO_3$ in the center of a quartz tube (i.d. 4mm, 300mm long). Gas flows were regulated by mass flow controllers (Brooks, 4850 series, Exton, PA, USA) with exchange experiments conducted in the temperature range of 25-600 ^oC. Prior to measurement the samples were heated to 800 ^oC in a flow of 50mL/min dry air with < 0.5 ppm CO_2 and subsequently reduced at the same temperature for one hour under flowing 50ml/min 3 vol% H_2O / 5 vol% H_2 / Ar (wet H_2). The sample was then equilibrated at the measurement temperature in a flow of 50mL/min 5 vol % H_2 / Ar (dry H_2), 100μL pulses of 5 vol % D_2/Ar (dry D_2) were injected into the reactor, separated by 90-s intervals of 5 vol% H_2/Ar, using a computer controlled 6-way valve with pneumatic actuator (Swagelok model 131 SR). To study the exchange reaction in the presence of water (which will increase the proton concentration in the sample), the powder samples were equilibrated in wet H_2 at measurement temperature prior to injection of D_2. The D_2 pulse was dry. The total flow rate was varied from 50 to 150 mL/min. Within this range, the flow rate did not influence on the surface

reaction rate indicating that the reactor operates with plug flow. The DH (m/e=3) and D_2 (m/e=4) concentrations in the reactor effluent were continuously analyzed (sampling frequency, $1.67s^{-1}$) using a residual gas analyzer (RGA) fitted with a quadropole analyzer and associated Faraday and secondary electron multiplier detectors (Cirrus 2, MKS Instruments UK Ltd). It was observed that the H_2 (m/e =2) signal did not vary significantly during the pulse due to the relatively short duration of the pulse compared with the gas residence time in the RGA chamber. As such, only the DH and D_2 signals were recorded during measurements to increase the sampling frequency. The amount of D_2 consumed in a reactive pulse was obtained by the difference in average peak area between reactive and blank experiments. This procedure was repeated in steps of 25°C.

Experiments were conducted without a powder sample and with only $SrTiO_3$ (STO) to quantify the amount of D_2 in an unreacted pulse, and verified that STO was unreactive towards D_2/H_2 exchange, respectively. Five pulses were injected in 90-s interval, in the temperature range 25-800 °C. The mean value of the DH signal measured before the initial pulse was used as baseline, the peak area was calculated by numerical integration, and the obtained peak area was normalized relative to the baseline. No significant change in peak area was detected until 600 °C for the STO sample or until 700°C for the blank reactor, where the conversions of D_2 were less than 3%. In the case of blank reactor, this represents homogeneous gas-phase exchange occurring at the leading and trailing edges of the pulse. The maximum temperature utilized in this study was 600°C, and we thus consider STO as an inactive sample diluent and do not consider gas-phase homogeneous exchange. STO was utilized as a diluent mixed with the active phase of interest to lower the isotope conversion and extend the range of temperatures accessible in this study. STO was mixed by dry milling with the active material in the ratio of 20:1.

2.3 Results

The synthesized powders were characterized by X-ray diffraction, Figure 2.1. The patterns for BC and BCY were indexed to an orthorhombic perovskite (space group *Pmcn*) [16-19]. BZ and BZY

were indexed to a cubic perovskite structure (space group *Pm-3m*) [20-22]. BET surface areas ranged from 1.64 m^2/g for BCY, to 2.97 m^2/g for BZY, Table 1. Metals supported on BZ (M/BZ, M = Co, Ni, Cu, and Pt) were characterized with SEM, figure 2.2, showing that the metal exists as small particles distributed across the BZ surface. The surface areas of Co/BZ, Ni/BZ, Cu/BZ and Pt/BZ were 1.26 m^2/g, 2.06 m^2/g, 1.98 m^2/g and 1.84 m^2/g, respectively.

Figure 2.3(a-b) is representative data showing the change in recorded DH and D_2 signals by isotopic exchange reaction with BZ at 200 ^oC and 550 ^oC in dry H_2 flow. DH formation was not observed at 200 ^oC, and the measured D_2 is equal to that for the blank reactor. In contrast, significant DH formation is observed at 550 ^oC and was accompanied by corresponding reduction in the D_2 area. In wet H_2 figure 2.3(c-d) , no exchange was observed at 300 ^oC, but noticeable DH and DHO formation were observed at 750 ^oC. There was no significant difference between the peak area of DH and DHO, the sum of DH and DHO area corresponded to the reduction in the D_2 area at 750 ^oC. No D_2O signal was not detected in our study.

H_2/D_2 isotope exchange reaction experiments were conducted as a function of temperature for BZ, BC, BZY and BCY respectively, Figure 2.4(a-d). The data points represent the relative peak area of D_2 and DH, each data point was obtained from the average integral area of five pulses in a single isothermal experiment. The surface exchange reaction was observed above 225 and 175 ^oC in BZ and BZY, and above 250 ^oC in BC and BCY, with DH formation increasing rapidly with increasing temperature up to 550, 425, 375 and 375^oC in BZ, BZY, BC and BCY. The conversion of D_2 reached above 88% at the before mentioned temperature. The exchange reaction experiments were also conducted in wet H_2, figure 2.4(e-f). The surface exchange reaction in wet H_2 was observed at above 400 ^oC in BZ and BC, significantly higher than in dry H_2. The conversion of D_2 in BZ and BC reached 71.3 and 93.1 % at 725 and 575 ^oC respectively. The standard variation between pulse areas in each isothermal experiment was calculated to vary between 0.4 and 3 %. Error bars are smaller than the symbol size in figures 2.3 and 4.

Sample	Composition	Tcalc [^{0}C]	Space group	Lattice constant			BET [m^2 / g]
				a [Å]	b [Å]	c [Å]	
BC	$BaCeO_3$	1100	*Pmcn*	8.7845(6)	6.2387(0)	6.219(5)	2.47
BCY	$BaCe_{0.9}Y_{0.1}O_{3-\delta}$	1100	*Pmcn*	8.7700(8)	6.2427(6)	6.2198(8)	1.64
BZ	$BaZrO_3$	1300	*Pm-3m*	4.2048(1)	4.2048(1)	4.2048(1)	2.01
BZY	$BaZr_{0.9}Y_{0.1}O_{3-\delta}$	1300	*Pm-3m*	4.1993(0)	4.1993(0)	4.1993(0)	2.97

Table 2.1 Crystallographic parameters and BET surface areas.

Sample	Activation energy (kJ/mol) in dry H_2	Activation energy (kJ/mol) in humidified H_2
BC	87.7 ± 16.5	131.4 ± 21.7
BCY	101.3 ± 28.1	
BZ	48.2 ± 5.0	61.1 ± 9.5
BZY	46.4 ± 6.1	
Co/BZ	38.8 ± 2.3	
Ni/BZ	24.4 ± 1.3	
Cu/BZ	37.1 ± 6.4	
Pt/BZ	-	32.8 ± 2.0

Table 2.2 Activation energy of H2/D2 surface exchange.

Figure 2.1 X-ray diffraction patterns of BC, BCY, BZ and BZY

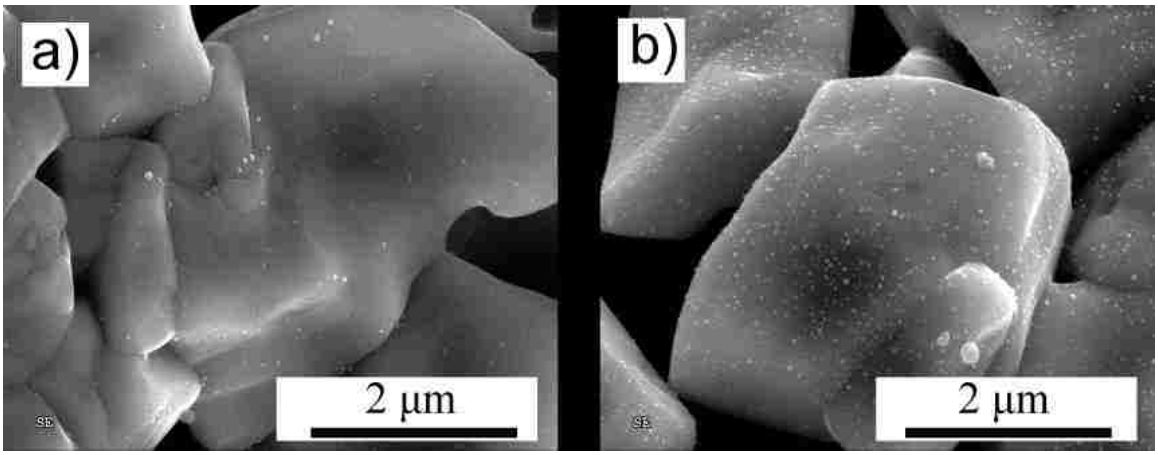

Figure 2.2 SEM micrographs a) Ni/BZ and b) Pt/BZ

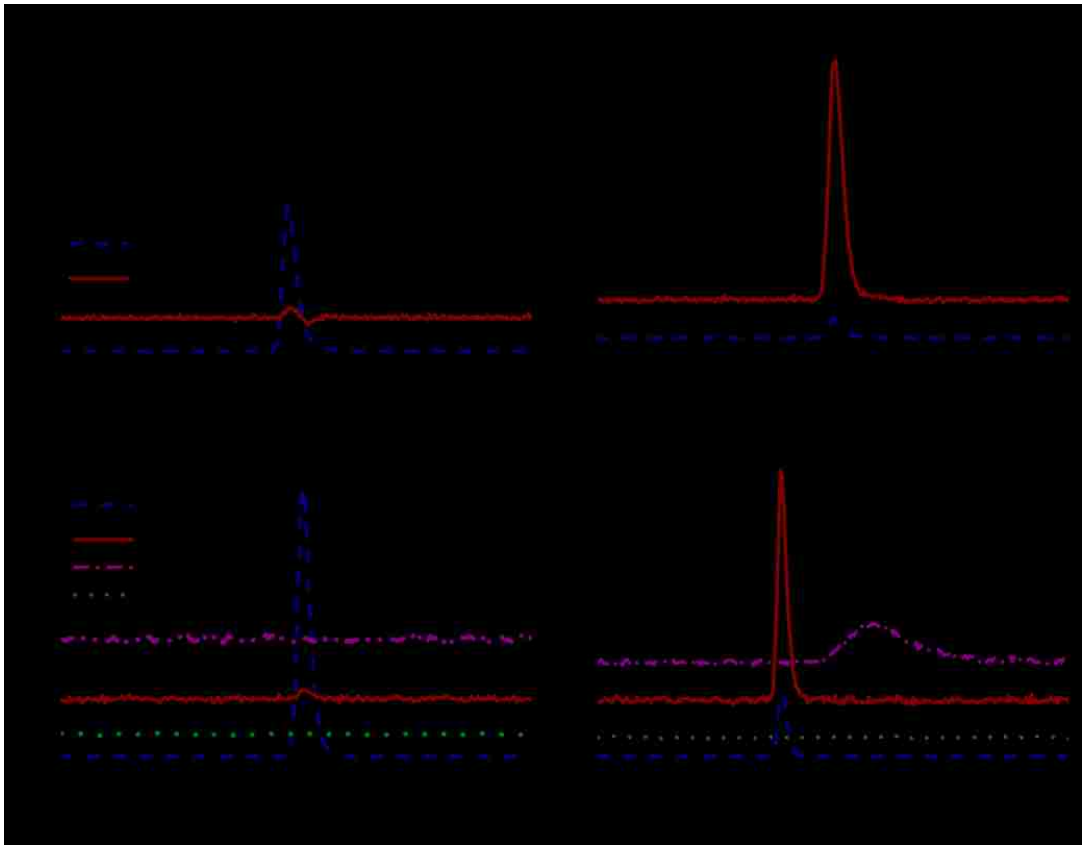

Figure 2.3 DH formation and D2 consumption in a single pulse (100μL, 5% D2) over BZ in dry H2 at a) 200 °C and b) 550 °C, DH and DHO formation and D2 consumption in wet H2 at c) 300 °C and d) 750 °C

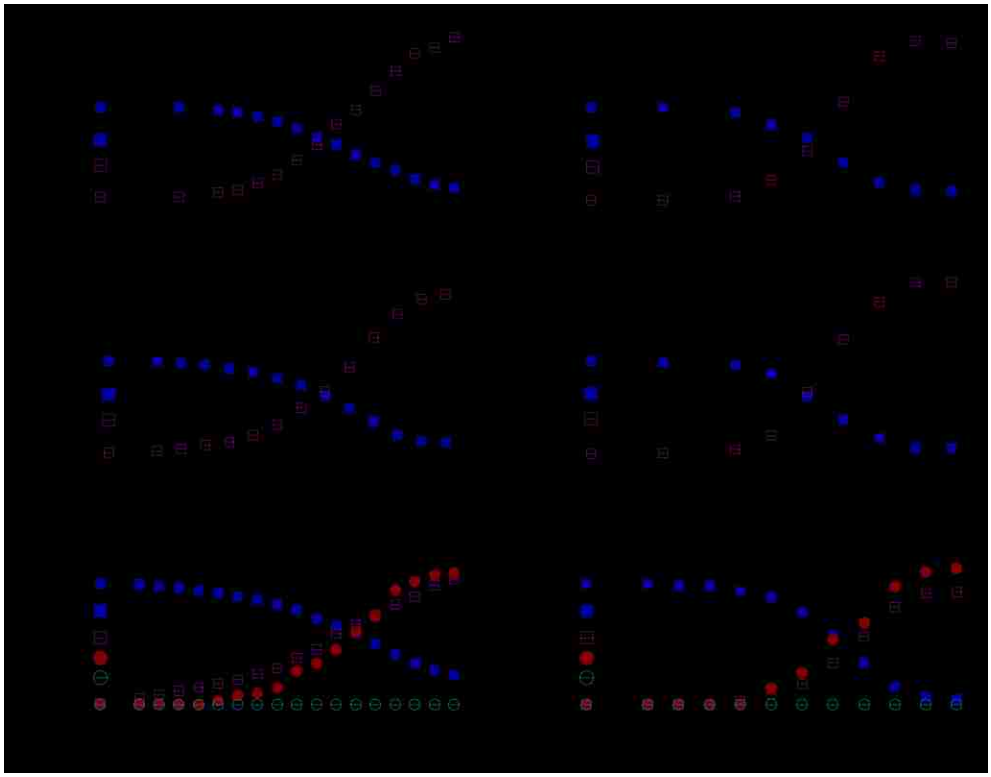

Figure 2.4 Relative peak area of D2 and DH as a function of temperature for (a) BZ, (b) BC, (c) BZY and (d) BCY in dry H2, relative peak area of D2, DH and DHO for (e) BZ, (f) BC in wet H2.

Figure 2.5 shows the overall reaction rates calculated from the raw pulse data for the oxides, along with the supported metal catalysts (M/BZ, M=Co, Ni, Cu, Pt), as a function of inverse temperature. Only relatively small differences in the surface exchange reaction rates of BZ, BZY, BC and BCY were observed in the temperature range studied. For example, the reaction rates were 2.44, 3.12 × 10^{-5} mol/m^2·s at 350, 325 °C in BZ and BZY, 3.17 and 5.75 × 10^{-5} mol/m^2·s at 300 °C in BC and BCY, respectively. In contrast, significant differences were observed between the bare oxide and supported metal catalysts except for Cu/BZ, with activity following the trend Pt/BZ>Ni/BZ >Co/BZ>Cu/BZ≈BZ. An overall reaction rate of 1.08 × 10^{-4} mol/m^2·s was obtained on BZ at 475 °C, with the similar reaction rates of 1.00 and 1.07 × 10^{-4} mol/m^2·s obtained at the lower temperatures of 175, 150 and 75°C for Co/BZ and Ni/BZ, respectively. It should be noted that the rate of the exchange reaction on Pt/BZ was not obtained due to complete H_2/D_2 exchange even at 25 °C. The dashed line in Figure 2.5 thus represents a minimum rate for this reaction.

The reported overall reaction rate under wet conditions is the total consumption rate of D_2. It was observed that the overall reaction rates in wet H_2 were noticeably slower in BZ and BC compared to the case of dry H_2. For example, the overall reaction rate of BZ and BC in wet H_2 were 2.36 and 8.41 × 10^{-5} mol/m^2·s at 550 and 525 °C respectively, while they were 2.44 and 6.98 × 10^{-5} mol/m^2·s at 350 and 325 °C in dry H_2. While the direct comparison of overall reaction rate of Pt/BZ between humidified and dry H_2 wasn't available, it could be indirectly identified that the reaction rate in wet H_2 was significantly slower than in dry H_2. The activation energies for the exchange reaction were calculated by fitting to the Arrhenius equation, with the values ranging from 24.4 ± 1.3 (Ni/BZ) to 101.3 ± 28.1(BCY) in dry H_2, from 32.8 ± 2.0 (Pt/BZ) to 131.4 ± 21.7 (BC) in humidified H_2 (Table 2).

HS-LEIS measurements for BZ and BZY were performed using BaO_2, ZrO_2, and Y_2O_3 as calibration samples for quantification of the relative surface coverage of each element Figure 2.6(a-c). It should be noted that all samples were analyzed with 4 keV He^+ (4.0 × 10^{14} He^+ ions/cm^2) to check the contamination on the surface of powder samples, but no significant

indication of carbon was observed. Figure 2.6 shows the spectra of each sample, including the calibration samples, demonstrating clear separation of the Ba and Zr peaks, but overlap between Zr and Y. Note that in the following discussion we utilize the term fractional coverage to reference only the fractional cation abundance on the surface. The fractional surface coverage of cations was calculated using two methods: either by assuming the reference samples represents 100% coverage of the element or by back-calculation from depth profiling assuming that the signal intensity plateaus at the bulk value. This second method has the advantage that calibration samples are not required. A Ba fractional surface coverage of 80.5% was obtained using the first calculation method from an initial scan (1.03×10^{15} ions/cm^2), Figure 2.7. This fractional coverage is in good agreement with prior reports [23]. However, it should be noted that the total signal intensity for this first measurement was lower than for subsequent measurements due to this surface carbonate layer.

Following this, an initial sputter of 2 keV Ar^+ (4.7×10^{16} ions/cm^2) to remove the carbonate layer present on the outer-most surface was performed. The measured Ba surface coverage was then measured to decrease to 72.9%. The depth profile measurement of BZ was conducted by repeated sputtering with Ar ion dose (4.7×10^{16} Ar^+ ions/cm^2). The fraction of Ba decreases as the sputtering number increases, reaching a plateau 62.7 %, based on calculation using the reference samples, figure 2.7(a). To further probe the outermost surface composition, surface analysis was performed with a lower ion dose, 4keV Ne^+ (1.65×10^{14} ions/cm^2), followed by a depth profile with 2 keV Ar^+ (9.5×10^{14} ions/cm^2). Slightly higher Ba surface coverage (87.1%) was obtained in this measurement; however, a clear depth profile was not generated due to the significantly reduced sputtering ion dose density. Back-calculation from assuming that the plateau value represents 50% Ba leads to a value of 71.1% Ba surface coverage for the outermost surface of BZ, Figure 2.7(a). In the case of BZY, accurate calculation was not available due to the overlap of Zr and Y peaks. However, under the assumption that ion scattering from the 10 at-% Y

does insignificantly differ from Zr, the calculation with calibration sample brought fractional coverage of 83.6 % Ba at the outmost surface with caveat that the Zr and Y peaks overlap.

The cerates, BC and BCY, could not be analyzed utilizing HS-LEIS due to overlap of the Ce and Ba peak positions. As an alternative measure, the Surface composition these samples was investigated by XPS (X-ray Photoelectron Spectra), with BaO_2, Y_2O_3, and CeO_2 used as calibration samples for quantification, Figure 2.8(a-b). Quantification was achieved by using the area of main peaks that do not overlap, Ba 3d, Ce 3d, and Y 3d. The resulting calculated, Ba fractional surface coverages were 72.7% and 73.9% in BC and BCY respectively.

2.4 Discussion

The solid state ionics community typically considers two steps for the generation and incorporation of a mobile ionic species in a solid: a surface reaction step followed by bulk transport. In this case, the powder equilibrated in H_2 is a large source of protons for exchange with D_2 in the pulse. Ensuring that the measured reaction rate in this study is the true surface reaction rate was a focus of the design of the experiments presented here. Experiments were conducted as a function of reactant flow rate, from 50 to 150 ml/min, to verify no change in reaction rate with gas flow rate, indicating that the system follows plug flow reactor behavior. No observed change in reaction rate with flow rate also indicates facile gas-phase transport of reactants or products across the stagnant gas boundary layer exterior to the particle.

We have utilized a pulse isotope reactor system rather than a step switch from unlabeled to labeled reactant in order to minimize the influence of bulk ionic transport. A step change from H_2 to D_2 followed by equilibration of the particles in D_2 inherently convolutes surface reaction and

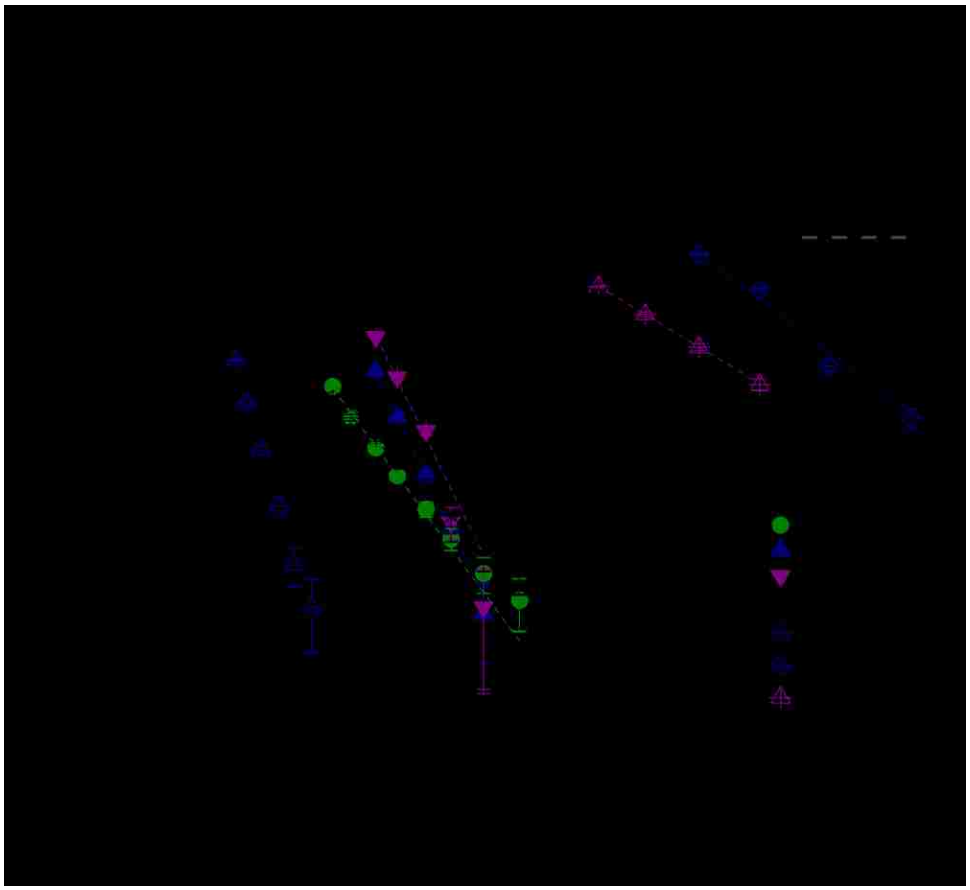

Figure 2.5 Surface exchange reaction rates for H2/D2 isotope exchange over BZ, BZY, BC, BCY and M/BZ (M=Co, Ni, Cu and Pt) in dry H2, over BZ, BC and Pt/BZ in wet H2.

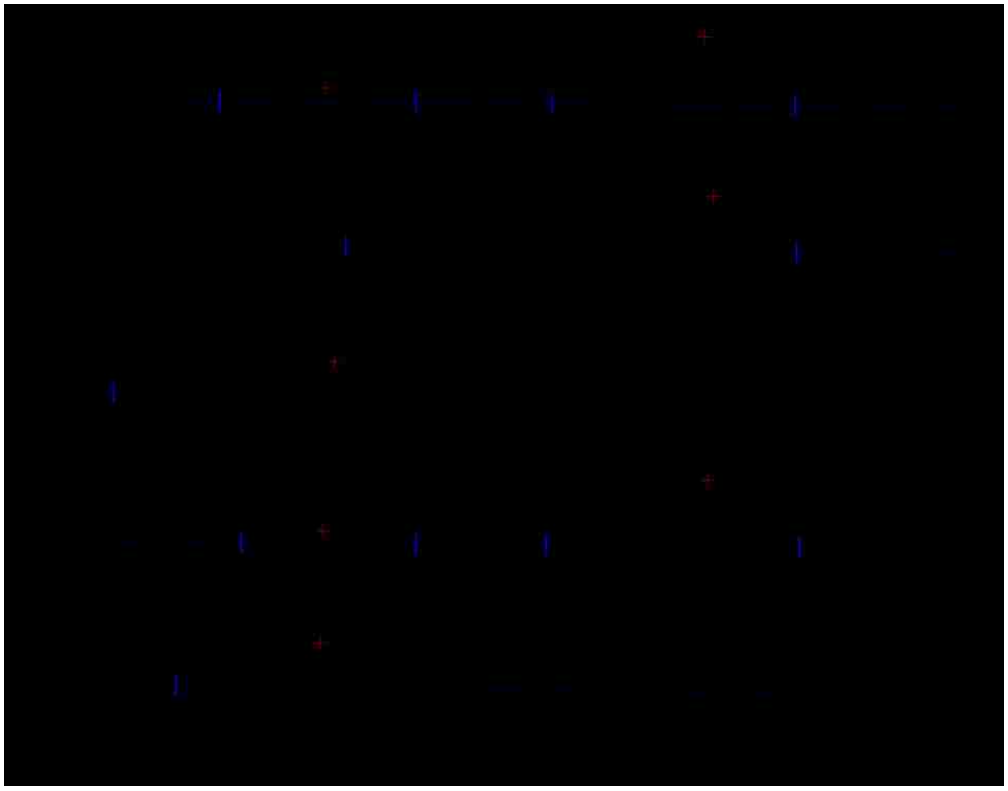

Figure 2.6 HS-LEIS spectrum of (a) BZ, (b) BaO2, (c) ZrO2, (d) BZY, (e) Y2O3 with4 keV Ne+ (1.03 × 1015 ions/cm2)

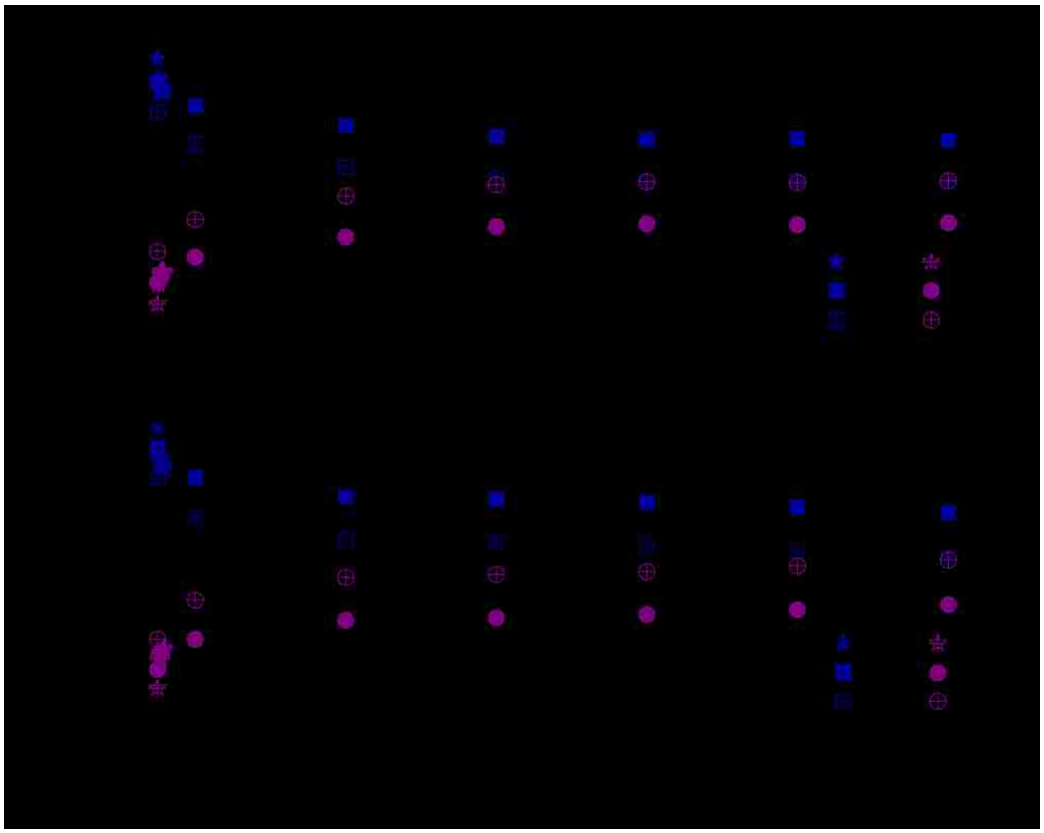

Figure 2.7 Depth profile measurement of (a) BZ and (b) BZY by repeated sputtering with Ar ion dose : 9.5 × 1014 (Ba:closed star, Zr:open star), 4.7× 1016 (Ba:closed square, Zr:closed circle) Ar+ ions/cm2. Back calculation (Ba:open square, Zr:open circle)

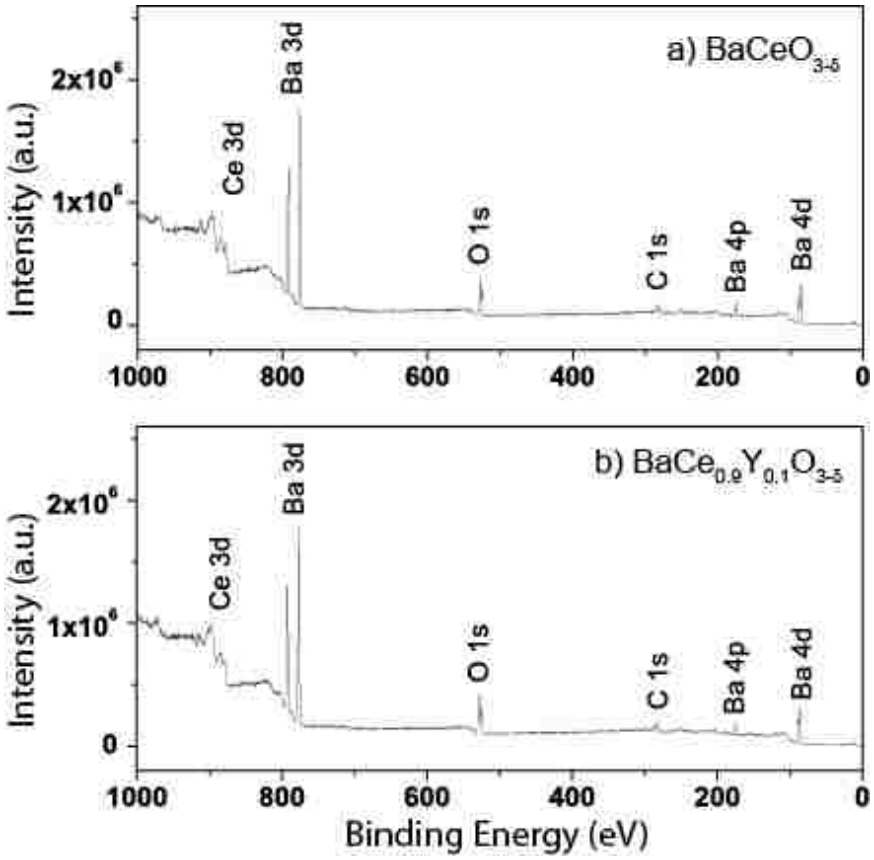

Figure 2.8 XPS scan for (a) BC and (b) BCY.

bulk transport; once the surface adsorbed H is depleted, further exchange with D_2 occurs with protons diffusing from the particle bulk. While possibly providing data on ionic transport rates, this convolution significantly complicates analysis. Our approach does, however, require appropriate sizing of the gas pulse in order to minimize the analysis convolution.

External mass transport of gas to the particle surface would create a reaction rate that is dependent on the gas flow rate through the changing thickness of the external laminar boundary layer. We observe no change in reaction rate with gas flow rate. The absence of exterior gas transport or interior ionic transport limitations is further confirmed by the dramatic differences in reaction rate observed upon the addition of catalytically active transition metals to the oxide surface. The use of the same sized particles for each experiment ensures that the exterior gas transport would be the same. As such, an external mass transport limited reaction rate would be constant with a change in surface composition. This argument also holds with regard to ionic transport: a change in surface composition would not influence a bulk transport limited rate. This discussion is similar to that utilized for the development of our related technique to measure the methane oxidation activity of perovskite oxides [24].

A previous analogous study regarding the oxygen isotope exchange reaction[25,26] clearly demonstrated a bulk interaction. While the amount of ^{16}O increased with reaction temperature, the amount of $^{18}O^{16}O$ initially increased upon increasing reaction temperature, reaching a maximum, and then declining at the highest measurement temperatures. This decline is due to bulk incorporation of the isotopic tracer into the oxide powder, and its subsequent loss from the gas phase. Thus a failure to close the isotope mass balance is a strong indicator of significant bulk exchange. A similar trend was not observed in our measurements: in all cases the isotope mass balance was closed at all temperatures. It is important to note that based on the consideration above, the current study reports the true surface exchange rate of D_2 with surface bound H and OH.

The reported proton concentration in BCY and BZY is between 8 and 10 % at pH_2O = 0.02atm and the temperature range considered in this study[5]. Thus, under the assumption that the concentration of protons in perovskite materials is 9 %, the number of proton is 2.76×10^{-6} mol in the powder sample (10mg) used in this study. A single pulse contains 2.0×10^{-7} mol of D_2 indicating that 4.0×10^{-7} mol of DH can be formed. In case of all pure samples, the conversion between about 10 to 90% was obtained, implying that 2.0 and 18×10^{-8} mole of D_2 were participated in the reaction. When compared to the amount of proton in samples, this amount is extremely low (1.4 and 13.0% of the number of proton in powder samples at 10 and 90 % conversion respectively). This is a final, if indirect, indication that our measured exchange reaction rate is probing the surface reaction.

Data analysis is the next concern Bouwmeester utilized a two-parameter fitting procedure in order to extract both a surface reaction rate constant and bulk ionic diffusivity from similar isotopic pulse experiments using $^{18}O_2/^{16}O_2$ [25]; however, as discussed above, the influence of bulk transport on our measurements is negligible. Indeed, fitting our data with this procedure resulted in a conclusion that the surface reaction rate dominates. As such, all of the data was fit assuming simple first order kinetics for the isotopic exchange reaction.

One surprising observation was the similarity of the observed rates between the oxides. It is commonly accepted that catalytic activity of perovskites is dominated by B-sited transition metal cations [23]. Furthermore, we may anticipate a difference in measured rate due to differences in bulk proton concentration between samples. In particular, we would anticipate higher proton concentration upon Y-doping [27]. This is where detailed surface composition analysis is essential to any discussion of observed rates over these mixed metal oxides.

The HS-LEIS and XPS data both indicate significant Ba enrichment on the surface of the phase pure powder samples. It should be noted that HS-LEIS and XPS have different penetration depth into the sample, with HS-LEIS only probing the outermost atomic layer, preventing direct

comparison between the reported Ba-enrichment for the zirconates and cerates. Our reported fractional surface coverage of Ba on BZ is in good agreement with the literature[23], and the depth profile clearly demonstrates significant Ba enrichment on the zirconates. Absolute quantification of the surface coverage by depth profile analysis or via reference samples leads to some discrepancy likely due to the different concentration of elements on the surface between BZ and reference samples[28,29], differences in sample roughness or preferential sputtering of elements. Nevertheless, we can confidently state that all of the samples show significant Ba surface enrichment. We thus interpret the lack of measureable difference in surface exchange rate between the pure zirconates and cerates to be due to these surface kinetics being dominated by hydrogen dissociation on the relatively low activity BaO sites that cover a significant fraction of all of the surfaces. Therefore, these materials do not show the typical dependence of activity on B-site cation. Thus surface enrichment of Ba is supported by other work[30] that reports Ba loss from perovskites during material preparation due to the high sintering temperatures and low melting point of BaO. Clearly this first stage of material loss is surface enrichment. Surface enrichment by the alkaline earth component has also been reported for numerous other SOFC candidate materials [31].

With the exception of Cu, all of the supported metal catalysts demonstrate significantly higher reaction rates than the bare oxides. It is clear from our results that hydrogen dissociation in H^+-SOFCs must occur on the metal component of the anode and that the oxide is comparatively inert towards the reaction. This is a similar scenario to that of Ni-YSZ composite electrodes for hydrogen oxidation in traditional oxygen anion based SOFCs, where Ni is considered the catalytically active component[32]. We can hypothesize that the H^+-SOFC anode reaction mechanism consists of H_2 dissociation on the metal, followed by hydrogen spillover onto the ceramic surface; however, further work is required to confirm this. Our results also clarify the previous work of Azimova and McIntosh that indicated that higher performance of Ni-based H^+-

SOFC anodes when compared to Cu-based anodes was due to a difference in electrocatalytic activity towards hydrogen incorporation [33]. This is clearly shown in Figure 2.5.

A significant reduction of reaction rate was observed when the sample was previously equilibrated in wet H_2. We suggest that this is due to a surface coverage of OH originating from H_2O blocks some of the sites for D_2 dissociation. As shown in Figure 2.4, around half of the D atoms on the surface combine with this absorbed OH to form DHO. The observed activation energy (32.8 ± 2.0 kJ/mol) on Pt/BZ in wet H_2 is in good agreement with the activation energy (40.5 kJ/mol) for water desorption obtained in the literature[34], further indicating that the decreased reaction rate can be attributed to water desorption.

The activation energy was calculated by Arrhenius fitting of single dashed lines through the overall exchange reaction rate of each samples. BZ and BZY have the lowest measured activation energy of the pure oxides, (48.2 ± 5.0 and 46.4 ± 6.1 kJ/mol) with both zirconates showing significantly lower activation energy than the cerates, Table 2. Despite similar trends with surface coverage of Ba, significant differences in activation energy between cerates and zirconates may be due to the different crystal structure or the influence of underlying atoms on chemisorption to the surface atomic layer.

If we assume that the measured kinetics for the supported metal catalysts are dominated by hydrogen dissociation on the metal, there are some limited literature reports available for direct comparison with our results. Magnusson[35] performed H_2/D_2 exchange on α-Al_2O_3 supported Cu and Ni catalysts. While the reported activation energy (73.3 kJ/mol, for an Eley-Rideal mechanism) of hydrogen dissociation on Cu did not match our result, the measured trend of higher activity of Ni compared with Cu supports our result. Liao and Sun[36] calculated, the activation energy for hydrogen chemisorption on stepped surfaces of Ni and Cu to be 24.12 and 65.61 kJ/mol in Ni(410) and Cu(410) in better agreement with our result. This activation energy was for a reaction pathway representing H_2 approaching the outside edge of a terrace.

Sun et al recently concluded that hydrogen dissociation is the rate-limiting step for hydrogen oxidation at the Pt–BZCYYb interface[12]. This conclusion was reached by analysis of electrochemical impedance data obtained from patterned electrodes under a variety of measurement conditions. This conclusion is somewhat at odds with the work described herein, where we directly measure H_2 dissociation rates and find that Pt is highly active for this reaction. Our conclusion fits with the literature on transition metal catalysis[37] and the measured reaction rate is certainly higher than the rate of bulk proton transport [5], indicating that the rate limiting process for Pt-based electrodes is more likely to involve the ceramic component. The activation energies reported by Sun et al [12], between 54.03 and 62.72 kJ/mol, also disagree with those previously reported by Montano et al[38], 22.18 kJ/mol for HD formation on Pt(111). Further work is required to measure the rates of the other reaction steps (absorbed species spillover, electron transfer, and proton incorporation) and to integrate our results into electrode studies.

2.5 Conclusion

While the pulsed isotope experiments utilized in this study were demonstrated to effectively measure the H_2/D_2 surface exchange rate on a range of proton conducting ceramics, the measured rate was dominated by the similar surface composition. One must be careful to fully analyze the surface composition when reporting the surface exchange rate of mixed metal oxide. In this case, Ba-enrichment at the surface may be unavoidable due to the high sintering temperatures required for these materials, and the relatively high volatility of BaO. With respect to their use in cermet electrodes, it is clear that, with the exception of Cu, the metal component of the electrode will dominate the observed exchange kinetics. While we may hypothesize a hydrogen-spillover mechanism, further work is required to understand the role of H_2O, the exact nature of the active site, and the location and rates of the electrochemical charge-transfer steps.

2.6 References

1. Stambouli, A. B.; Traversa, E. *Renewable and Sustainable Energy Reviews* **2002***, 6*, 433-455.

2. Yamamoto, O. *Electrochim. Acta* **2000***, 45*, 2423-2435.

3. Steele, B. C. H. *Journal of Materials Science* **2001***, 36*, 1053-1068.

4. Carter, S.; Selcuk, A.; Chater, R. J.; Kajda, J.; Kilner, J. A.; Steele, B. C. H. *Solid State Ionics* **1992***, 53–56, Part 1*, 597-605.

5. Kreuer, K. D. *Annu. Rev. Mater. Res.* **2003***, 33*, 333-359.

6. Norby, T. *Solid State Ionics* **1999***, 125*, 1-11.

7. Dicks, A. L.; Fellows, R. G.; Martin Mescal, C.; Seymour, C. *J. Power Sources* **2000***, 86*, 501-506.

8. Ito, N.; Iijima, M.; Kimura, K.; Iguchi, S. *J. Power Sources* **2005***, 152*, 200-203.

9. Fabbri, E.; Bi, L.; Pergolesi, D.; Traversa, E. *Adv Mater* **2012***, 24*, 195-208.

10. Hibino, T.; Hashimoto, A.; Suzuki, M.; Sano, M. *Journal of The Electrochemical Society* **2002***, 149*, A1503-A1508.

11. Boehm, E.; McEvoy, A. J. *Fuel Cells* **2006***, 6*, 54-58.

12. Sun, W.; Liu, M.; Feng, S.; Liu, W.; Park, H. C.; Liu, M. *Phys. Chem. Chem. Phys.* **2013***, 15*, 3820-3826.

13. H. E. van Doorn, R.; Kruidhof, H.; Nijmeijer, A.; Winnubst, L.; J. Burggraaf, A. *J. Mater. Chem.* **1998***, 8*, 2109-2112.

14. Levy, P.; Primet, M. *Applied Catalysis* **1991***, 70*, 263-276.

15. Larson, A. C.; Von Dreele, R. B. , 1985.

16. Knight. Kevin S.; Bonanosb. Nicholas *Journal of Materials Chemistry* **1994***, 4*, 899-901.

17. Knight. K.S. *Solid State Ionics* **2001***, 145*, 275-294.

18. Takeuchi, K.; Loong, C. K.; Richardson Jr., J. W.; Guan, J.; Dorris, S. E.; Balachandran, U. *Solid State Ionics* **2000***, 138*, 63-77.

19. Glöckner, R.; Islam, M. S.; Norby, T. *Solid State Ionics* **1999***, 122*, 145-156.

20. Stokes, S. J.; Islam, M. S. *J. Mater. Chem.* **2010***, 20*, 6258-6264.

21. Braun, A.; Duval, S.; Ried, P.; Embs, J.; Juranyi, F.; Strässle, T.; Stimming, U.; Hempelmann, R.; Holtappels, P.; Graule, T. *J. Appl. Electrochem.* **2009***, 39*, 471-475.

22. Duval, S. B. C.; Holtappels, P.; Vogt, U. F.; Stimming, U.; Graule, T. *Fuel Cells* **2009***, 9*, 613-621.

23. Rosink, J. J. W. M.; Jacobs, J. P.; Brongersma, H. H. *AIP Conf. Proc.* **1996***, 378*, 44-51.

24. van den Bossche, M.; McIntosh, S. *Journal of Catalysis* **2008***, 255*, 313-323.

25. Bouwmeester, H. J. M.; Song, C.; Zhu, J.; Yi, J.; van Sint Annaland, M.; Boukamp, B. A. *Phys. Chem. Chem. Phys.* **2009***, 11*, 9640-9643.

26. Zhu, J.; van Ommen, J. G.; Bouwmeester, H. J. M.; Lefferts, L. *Journal of Catalysis* **2005***, 233*, 434-441.

27. Kreuer, K. D. *Solid State Ionics* **1999***, 125*, 285-302.

28. W. Wong-Ng, R. S. R. *Physica C: Superconductivity* **1994***, 233*, 97-101.

29. Chaisuka, C.; Boonpitaka, P.; Panpranotb, J.; Mekasuwandumronga, O. *Catalysis Communications* **2011***, 12*, 917-922.

30. Shima, D.; Haile, S. M. *Solid State Ionics* **1997***, 97*, 443-455.

31. Baumann, F. S.; Fleig, J.; Konuma, M.; Starke, U.; Habermeier, H.; Maier, J. *Journal of The Electrochemical Society* **2005***, 152*, A2074-A2079.

32. Bessler, W. G.; Vogler, M.; Stormer, H.; Gerthsen, D.; Utz, A.; Weber, A.; Ivers-Tiffee, E. *Phys. Chem. Chem. Phys.* **2010***, 12*, 13888-13903.

33. Azimova, M. A.; McIntosh, S. *Journal of The Electrochemical Society* **2011***, 158*, B1532-B1538.

34. Rinnemo, M.; Deutschmann, O.; Behrendt, F.; Kasemo, B. *Combust. Flame* **1997***, 111*, 312-326.

35. Magnusson. Jeppe *Ind. Eng. Chem. Res.* **1987***, 26*, 877-881.

36. Liao, T.; Sun, Q. *physica status solidi (b)* **1997***, 200*, 491-498.

37. Hammer, B.; Norskov, J. K. *Nature* **1995***, 376*, 238-240.

38. Montano. Max, Bratlie. Kaitlin, Salmeron. Miquel,Somorjai. Gabor A. *J. Am. Chem. Soc.* **2006***, 128*, 13229-13234.

3. Insights into hydrogen oxidation on SOFC anode materials by isotopic exchange

3.1 Introduction

Like proton conducting SOFC, there is an ongoing debate regarding the details of fuel oxidation in the anode of oxygen conducting SOFC. Geometrically well-defined patterned electrodes have been utilized to remove complications regarding micro-structure[1-4]; however even these well-devised experimental systems lead to different proposed rate determining steps.

Mizusaki et al. [4]concluded that the rate determining step is either a dissociative adsorption of reactants or a surface diffusion of absorbed species on the Ni surface. In contrast, de Boer[2]proposed a charge transfer process, including proton incorporation with oxygen in the bulk oxide and protonation of absorbed hydroxide ions to form water. Bieberle proposed an important role for the removal of O^{2-} to a hydroxylated surface extending from the Ni/YSZ/Gas triple phase boundary[1]. The most recent comprehensive combined experimental and modeling study by Bessler et al. [3] concluded that hydrogen spillover from the Ni surface at the triple phase boundary is the primary rate limiting process.

All of these previous studies are based on deconvolution and fitting of electrochemical impedance spectra, typically under varying operating conditions. Isotopic labeling enables a wide range of techniques to probe the reaction mechanism. The most widely utilized technique in the SOFC field is perhaps depth profiling to determine surface exchange and self-diffusion coefficients in mixed ion-electron conductors[5]. With respect to the anode reaction mechanism, Horita et al. utilized D_2O and $^{18}O_2$ labelling combined with secondary ion mass spectrometry imaging with to directly observe the movement of oxygen and hydrogen. They performed this work for cathode systems[6-8] and to probe the triple phase boundary between Ni or Cu and yttria-

stabilized zirconia (YSZ) .[9]. In this latter case they reported that a thin oxide layer formed on the Ni and Cu is active for oxygen exchange, and in a further study observed oxygen spillover from the NI to the YSZ [10]. Alternatively isotope labeling has been used to compare the impedance spectra of a Ni/YSZ point electrode in H_2+H_2O and D_2+D_2O atmospheres [11], concluding that a change of rate determining step with increasing temperature from a process involving hydrogen species on the Ni surface to oxygen and/or hydroxide species.

In this study we present work that seeks to directly measure the hydrogen dissociation rate on the most common SOFC anode materials by H_2/D_2 isotopic exchange[12], utilizing a technique anaologous to the $^{18}O_2$ pulsing technique of Bouwmeester and coworkers[13]. The deuterium gas exchanges with hydrogen adsorbed on the material surface to measure the isotopic surface dissociation rate. Such direct measurements can provide data for current and future model verification

3.2 Experimental

Details of the H_2/D_2 pulse isotope exchange experiment and data analysis is described in a previous report[12]. Commercial 8-mol% yttria stabilized zirconia (YSZ, TZ-8YS, TOSOH, Japan) and $Gd_{0.2}Ce_{0.8}O_{2-x}$ (GDC, GDC20-TC, Fuel Cell Materials, OH, USA) powders were utilized. Supported Pt, Ni, Cu on pure oxide (1 wt-%, M= Pt, Ni and Cu, denoted M/YSZ or M/GDC) were fabricated using the incipient wetness procedure[12,14]. BET surface areas (ASAP2020, micrometrics, Norcross, GA, USA) were measured using N_2 gas as the absorbent after samples were degassed at 300 ^oC for 10h. The active material was mixed with $SrTiO_3$ by dry milling in the ratio of 1:1 for YSZ and GDC, and 20:1 for M/YSZ to lower the isotopic conversion and extend the range of accessible temperatures. All powder samples were sieved to obtain the 106-150 μm size.

The powder samples were held by quartz glass wool in the center of quartz tube (i.d. 4 mm, 300 mm long) and were pretreated in a flow of 50 mL/min dry air with < 0.5 ppm CO_2 at 800 °C to remove carbonates, and subsequently reduced in the flow of 50 ml/min 3 vol-% H_2O / 5 vol-% H_2 / Ar (wet H_2). Prior to pulsing with D_2, the gas composition was maintained at the wet H_2 conditions given above or changed to 50 mL/min 5 vol-% H_2 / Ar (dry H_2) at the measurement temperature. 100 μL pulses of 5 vol-% D_2/Ar (dry D_2) were injected into the reactor, separated by 90-s intervals of wet or dry H_2, corresponding to 'wet' or 'dry' data reported below. The DH (m/e=3) and D_2 (m/e=4) outlet concentrations were continuously measured (sampling frequency, 1.67s^{-1}) using a residual gas analyzer (RGA, Cirrus 2, MKS Instruments UK Ltd). Five pulses were injected in 90-s interval at each temperature. The exchange reaction rate was calculated as the average amount of D_2 consumed in a reactive pulse, obtained by the difference in average peak area between reactive and blank experiments. This procedure was repeated in steps of 25 °C in the temperature range 25-700 °C.

3.3 Results and discussion

Figure 3.1(a-b) shows the variation of recorded D_2 and DH signals by isotope exchange reaction with YSZ at 200 and 650 °C in dry H_2. No exchange is observed at 200°C however significant DH formation is observed at 650 °C and was accompanied by corresponding reduction in the D_2 area. Figure 3.1(c-d), shows similar data for reaction in wet H_2. D_2 consumption is not observed at 300 °C, but significant DH and DHO formation are observed at 700 °C. The sum of the DH and DHO areas corresponds to the reduction in the D_2 area. The quantity of DH and DHO formed were very similar and no D_2O formation was observed in this study. The observed lag in detection of DHO is due to increased residence time for DHO in the silica capillary for the RGA.

H_2/D_2 isotope exchange reaction experiments with YSZ and GDC were performed as a function of temperature, Figure 3.2(a-b). The surface exchange reaction was observed above 200 °C in YSZ and GDC, gradually increased DH formation was observed with increasing

Sample	In dry H_2 (kJ/mol)	In wet H_2 (kJ/mol)
YSZ	32.9 ± 3.0	84.4 ± 15.4
GDC	41.8 ± 7.3	88.2 ± 10.7
Cu/YSZ	40.5 ± 8.8	
Ni/YSZ	23.0 ± 1.1	27.0 ± 3.17
Ni/GDC	19.4 ± 1.1	25.6 ± 6.26
Pt/YSZ	-	46.7 ± 1.7

Table 3.1 Activation energy of H2/D2 surface exchange.

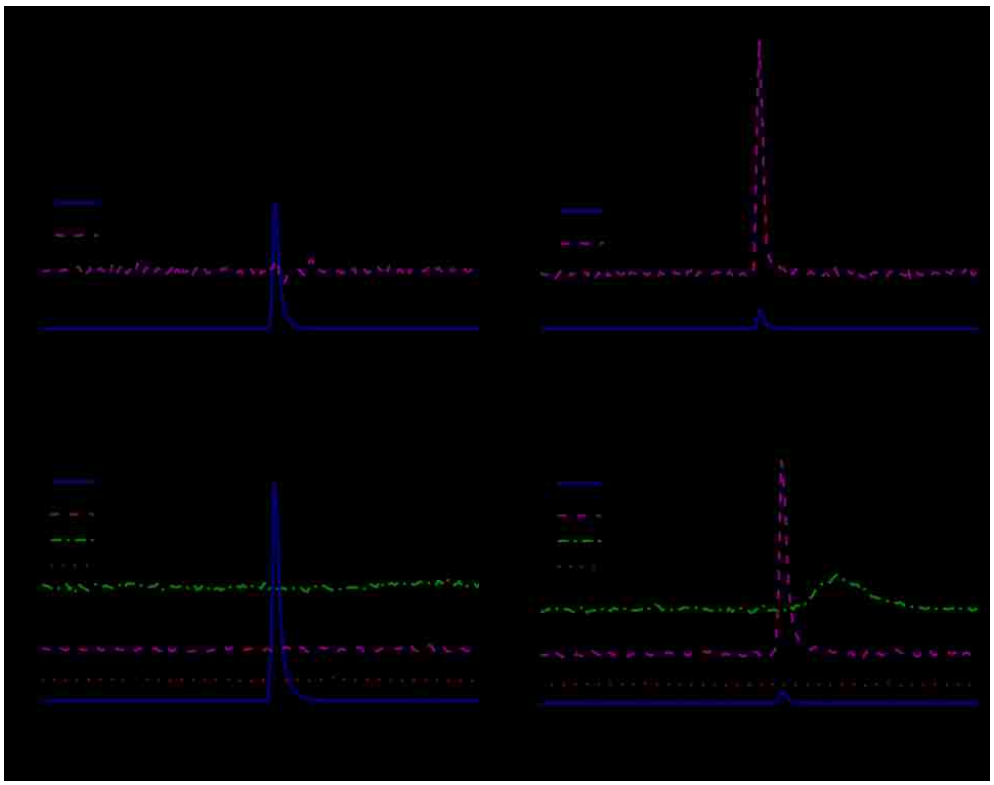

Figure 3.1DH formation and D2 consumption in a single pulse (100μL, 5% D2) over YSZ in dry H2 at a) 200 °C and b) 650 °C, DH and DHO formation and D2 consumption in wet H2 at c) 300 °C and d) 700 °C

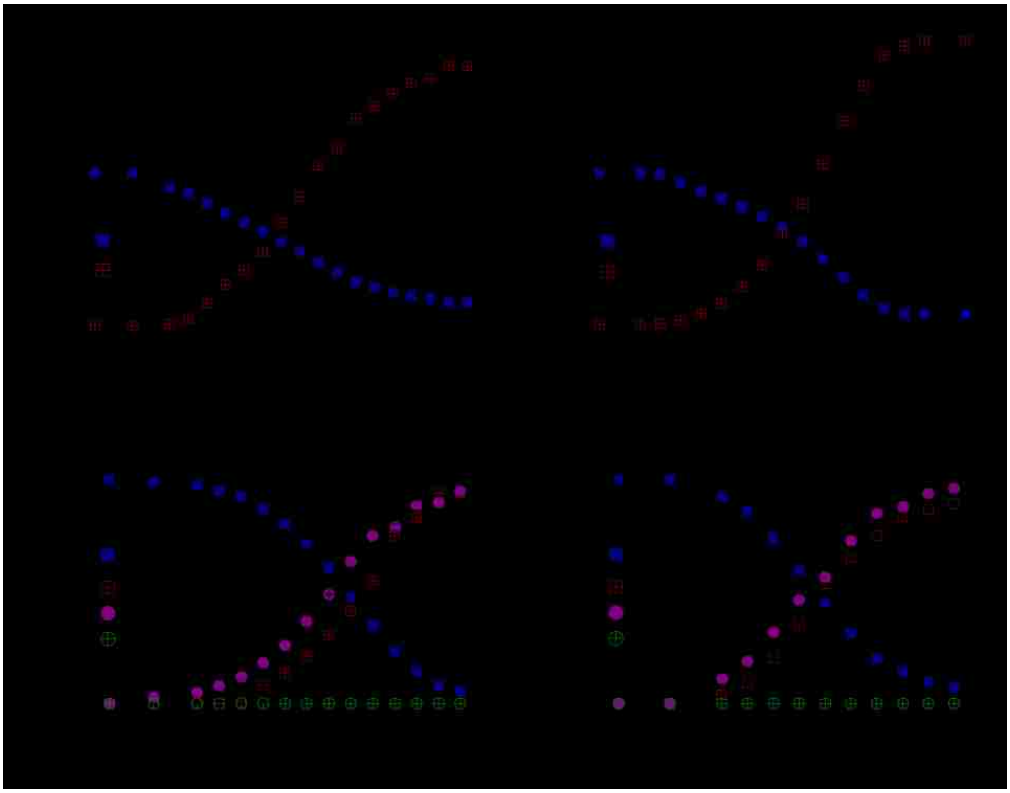

Figure 3.2 Relative peak area of D2 and DH as a function of temperature for (a) YSZ, (b) GDC in dry H2, D2, DH and DHO for (e) YSZ, (f) GDC in wet H2.

temperature up to 625 °C for YSZ, or 525 °C for GDC. The conversion of D_2 on YSZ and GDC reached 84.3 % and 92.0 %, respectively, at the upper measurement temperature. Figure 3.2(c-d) shows equivalent data for isotope exchange in wet H_2; isotopic exchange with YSZ and GDC was observed above 350 °C, significantly higher than in dry H_2. D_2 conversion in YSZ and GDC reached above 92% at 700 and 625 °C respectively.

Figure 3.3 shows the overall reaction rate calculated from the raw pulse data, normalized by the surface area (14.6, 6.42, 14.1, 12.5, 13.6 and 6.29 m^2/g for YSZ, GDC, Cu/YSZ, Ni/YSZ, Pt/YSZ and Ni/GDC), for the oxide, along with the supported metal catalysts (M/YSZ or GDC, M=Cu, Ni, Pt) as a function of inverse temperature. Table 1 shows that the activation energies for the exchange reaction calculated by fitting to the Arrhenius equation, with the values ranging from 19.4 ± 1.1 (Ni/GDC) to 41.8 ± 7.3(GDC) in dry H_2, from 46.7 ± 1.7 (Pt/YSZ) to 88.2 ± 10.7 (GDC) in wet H_2 (Table 2).

Higher exchange rates were observed over GDC than YSZ; for example, the surface exchange reaction rates in YSZ and GDC were 1.89 and 3.90 ($\times 10^{-5}$ $mol/m^2 \cdot s$) at 375 °C. With the exception of Cu/YSZ, the supported metals showed significantly higher reaction rates than the bare oxides. The exchange reaction on Pt/YSZ was not obtained due to complete H_2/D_2 exchange even at 25 °C, thus the minimum rate was represented by a dashed line in figure 3.3. This reinforces the concept that hydrogen dissociation occurs on the metal component of the anode and is not the rate determining step. Indeed, our results suggest that H_2 dissociation on the oxide is unfavorable and plays no important role in the anode mechanism. This agrees with the conclusion of previous work [3,15-17] that indicates a mechanism whereby dissociated hydrogen atoms on the metal component spillover from the metal to oxygen or hydroxide species on the oxide. It should be mentioned that Shishikin et al. [15,16] considered that oxygen spillover from oxygen enriched YSZ to Ni surface is also plausible for hydrogen oxidation.

Note also that in our data Ni/GDC shows higher exchange rates than Ni/YSZ samples and GDC shows higher rates that YSZ. This clear role of the oxide indirectly supports an alternative reaction mechanism based on hydrogen dissociation on the oxide surface or it may simply indicate enhancement of hydrogen spillover from the metal to GDC when compared with YSZ. As noted, the rate of exchange on the bare oxide is significantly lower than that on the metal, suggesting that the majority of hydrogen dissociation would occur on the metal surface in metal/oxide composite electrodes. Thus the increase in rate for GDC is not an additional direct exchange pathway from the bare GDC.

Modeling studies by Shishikin et al[18] and V. Papaefthimiou et al.[19], both suggest that CeO_2 and GDC may be active for hydrogen oxidation in the anode. Recently, Chueh et al.[20] reported experimental work to verify a catalytic role for samaria-doped ceria (SDC) in SDC-metal anodes. They investigated two different structures; one with well-defined Pt electrodes on top of a thin SDC film and one with the PT embedded in SDC. The almost identical surface resistance between samples was interpreted as direct evidence for SDC being the active component, and that the triple phase boundary between metal/oxide/gas plays a minimal role. This is in contrast with our finding that the bare oxides show significant lower hydrogen surface exchange rates when compared to samples with metal on the surface. Assuming similar rates would be observed for SDC and GDC, this leads to the conclusion that the rate determining step in the electrode measurements of Chueh et al.[20] is neither hydrogen dissociation on the oxide surface nor spillover from the metal to the oxide. Perhaps oxidation of the hydrogen on the SDC surface is rate determining. This would fit with the work of Bieberle [21] who suggest that the rate determining step in Ni/YSZ systems is the extraction of oxygen from the bulk YSZ to form a surface adsorbed species (with associated formation of a bulk oxygen vacancy and electron donation to the Ni); as shown in our work, hydrogen dissociation is facile on Ni.

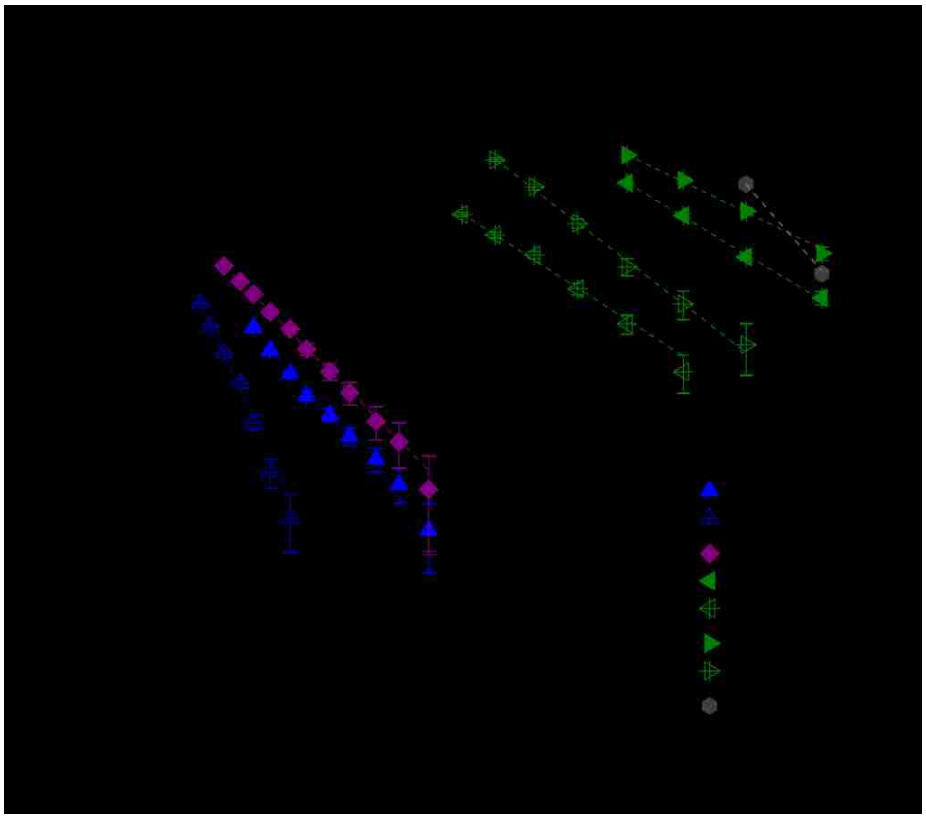

Figure 3.3 Surface exchange reaction rates for H2/D2 isotope exchange over YSZ, GDC and M/BZ (M=Ni, Cu and Pt) in dry H2, over YSZ, GDC and Pt/YSZ in wet H2.

The work of Bessler et al.[3] suggests that hydrogen spillover from Ni to surface hydroxyl or oxide ions is the rate determining step in Ni/YSZ anodes, and that the oxygen extraction steps occur through the formation of hydroxyl anions. Our work suggests that there should be a measurable difference in this spillover rate between YSZ and GDC.

The overall reaction rate for all of the samples was significantly slower in wet H_2 compared to dry H_2. We suggest that surface coverage of OH originating from H_2O dissociation[22] blocks sites for D_2 dissociation, reducing the observed rate. T. Horita et al. reported enhanced isotope oxygen surface exchange by a thin oxide layer formed by H_2O on the Ni and Cu mesh electrodes. Therefore one would speculate that the oxide layer might block the active site for D_2 dissociation, while the absence of D_2O formation as a product indirectly indicates that surface coverage of OH is more likely to block the active sites. The activation energy (46.7 ± 1.7 kJ/mol) obtained on Pt/YSZ in wet H_2, Table 1, is similar to that reported for water desorption in the literature (40.5 kJ/mol) [23], implying that water desorption may lead to the reduced reaction rate. In contradiction to this observed decrease in rate, literature reports on working SOFC electrodes [1,3,4] suggest that an increase in H_2O partial pressure enhances electrode performance. Bessler et al.[3] suggest that this result is due to the influence of electrode potential on rate; however, this observed enhancement is seen at low electrode overpotentials.

In activation energy calculation by Arrhenius fitting of single dashed lines through the overall exchange reaction rate of each sample, there was no significant difference between YSZ and GDC in dry and wet H_2, Table 2, indicating that similar activation energy can be attributed to identical crystal system [24,25]. The activation energy of the other supported metal catalyst (Ni/YSZ or GDC, Cu/YSZ) was discussed in our previous study [12]. Especially, lower activation energy of Ni/GDC than Ni/YSZ also indicates possibility of direct adsorption on the ceria surface of Ni/GDC.

3.4 Conclusion

To study the kinetics in anode of SOFC, the pulsed isotopic experiment was employed. It was identified that surface exchange reaction takes place only on transition metal, while oxygen conducting ceramics (YSZ and GDC) act as inert for the reaction in our measurement. Therefore, hydrogen-spillover mechanism can be supposed for hydrogen oxidation reaction in SOFC anodes, further work is required for the detail about the electrochemical charge-transfer steps, the role of H_2O and exact nature of the active site.

3.5 References

1. Bieberle, A.; Meier, L. P.; Gauckler, L. J. *Journal of The Electrochemical Society* **2001***, 148*, A646-A656.

2. Boer, B. d. SOFC Anode Hydrogen oxidation at porous nickel and nickel/yttriastabilised zirconia cermet electrodes, 1998.

3. Bessler, W. G.; Vogler, M.; Stormer, H.; Gerthsen, D.; Utz, A.; Weber, A.; Ivers-Tiffee, E. *Phys. Chem. Chem. Phys.* **2010***, 12*, 13888-13903.

4. Mizusaki, J.; Tagawa, H.; Isobe, K.; Tajika, M.; Koshiro, I.; Maruyama, H.; Hirano, K. *Journal of The Electrochemical Society* **1994***, 141*, 1674-1683.

5. Kilner, J. A.; De Souza, R. A.; Fullarton, I. C. *Solid State Ionics* **1996***, 86–88, Part 2*, 703-709.

6. Horita, T.; Yamaji, K.; Ishikawa, M.; Sakai, N.; Yokokawa, H.; Kawada, T.; Kato, T. *Journal of The Electrochemical Society* **1998***, 145*, 3196-3202.

7. Horita, T.; Yamaji, K.; Sakai, N.; Yokokawa, H.; Kawada, T.; Kato, T. *Solid State Ionics* **2000***, 127*, 55-65.

8. Horita, T.; Yamaji, K.; Sakai, N.; Xiong, Y.; Kato, T.; Yokokawa, H.; Kawada, T. *J. Power Sources* **2002***, 106*, 224-230.

9. Horita, T.; Yamaji, K.; Kato, T.; Sakai, N.; Yokokawa, H. *Solid State Ionics* **2004***, 169*, 105-113.

10. Horita, T.; Yamaji, K.; Kato, T.; Kishimoto, H.; Xiong, Y.; Sakai, N.; Brito, M. E.; Yokokawa, H. *J. Power Sources* **2005***, 145*, 133-138.

11. Norby, T.; Kofstad, P. *High Temperature Electrochemistry: Ceramics and Metals; proceedings of the 17th Riso International Symposium on Materials Science* **1996**, 381-386.

12. Shin, H. H.; McIntosh, S. *J. Mater. Chem. A* **2013***, 1*, 7639.

13. Bouwmeester, H. J. M.; Song, C.; Zhu, J.; Yi, J.; van Sint Annaland, M.; Boukamp, B. A. *Phys. Chem. Chem. Phys.* **2009***, 11*, 9640-9643.

14. Levy, P.; Primet, M. *Applied Catalysis* **1991***, 70*, 263-276.

15. Shishkin, M.; Ziegler, T. *J. Phys. Chem. C* **2009***, 113*, 21667-21678.

16. Shishkin, M.; Ziegler, T. *J. Phys. Chem. C* **2010***, 114*, 11209.

17. Weng, M. H.; Chen, H. T.; Wang, Y. C.; Ju, S. P.; Chang, J. G.; Lin, M. C. *Langmuir* **2012***, 28*, 5596-5605.

18. Shishkin, M.; Ziegler, T. *J. Phys. Chem. C* **2010***, 114*, 21411.

19. Papaefthimiou, V.; Shishkin, M.; Niakolas, D. K.; Athanasiou, M.; Law, Y. T.; Arrigo, R.; Teschner, D.; Hävecker, M.; Knop-Gericke, A.; Schlögl, R.; Ziegler, T.; Neophytides, S. G.; Zafeiratos, S. *Advanced Energy Materials* **2013***, 3*, 762-769.

20. Chueh, W. C.; Hao, Y.; Jung, W.; Haile, S. M. *Nature materials* **2012***, 11*, 155.

21. Bieberle, A.; Gauckler, L. J. *Solid State Ionics* **2002***, 146*, 23-41.

22. Mogensen, M.; Skaarup, S. *Solid State Ionics* **1996***, 86–88, Part 2*, 1151-1160.

23. Rinnemo, M.; Deutschmann, O.; Behrendt, F.; Kasemo, B. *Combust. Flame* **1997***, 111*, 312-326.

24. Lama, D. G.; Walsöe De Reca, N. E. *Journal of Materials Science* **2000***, 35*, 5563-5567.

25. Guan, X.; Zhou, H.; Wang, Y.; Zhang, J. *J. Alloys Compounds* **2008***, 464*, 310-316.

4. Proton Conducting Perovskites as Supports for Cr Catalysts in Short Contact Time Ethane Dehydrogenation

4.1 Introduction

Alkane dehydrogenation to produce light olefins from C_2-C_4 saturated hydrocarbon feedstock, is a key reaction in the chemical industry, especially as we seek to fully utilize natural gas resources from fracking. The most commonly utilized process for ethylene production is energy intensive non-catalytic steam cracking at high temperature[1-3]. In the last decades, catalytic oxidative ethane dehydrogenation has received increasing attention as it operates at reduced temperature and can potentially provide higher ethylene yields[4,5]; however, the oxidizing atmosphere leads to a number of issues such as significant loss of produced hydrogen as water, and undesirable complete oxidation to CO_2[3].

Non-oxidative alkane dehydrogenation over supported metal catalysts has been investigated as an alternative. Finely dispersed platinum and chromium supported on high surface area oxides are the most commonly studied catalysts[1,6]. Among those, supported Cr_2O_3 over Al_2O_3 catalysts are widely used as commercial catalyst on account of the outstanding property for alkane dehydrogenation[7]. The support material plays an important role in determining reaction selectivity in these systems with unsupported catalysts yielding low ethylene selectivity and rapid deactivation via carbon deposition[8,9]. Carbon deposition is common on these catalysts, requiring the reactor to be cycled for regenerations, for example in the CATOFIN® process. A reduction in operating temperature provided by a more active catalyst would lead to longer on-stream times.

In this study, our primary focus is the possible use of a proton conducting ceramic as a support material for these reactions. The use of a proton conducting support can potentially open up a new reaction pathway. As explained in chapter 1.3, the incorporated proton may be

considered as hydroxide ions on an oxide ion sites, $OH_O^{\bullet}$ in Kröger-Vink notation. This incorporation mechanism is analogous to the well-studied Mars van-Krevelen mechanism for oxygen in oxidation catalysis. Developing catalytic systems that can utilize this pathway may dramatically enhance the activity of supported heterogeneous catalyst for reactions involving hydrogen, particularly when hydrogen spillover to the support is expected to play an important mechanistic role. We have previously demonstrated that hydrogen spillover from metals to the support is the most likely mechanism of proton incorporation in these materials[10,11].

In this work, we study barium cerates and zirconates, which are among the most promising proton conducting oxides[12], as supports for Cr catalysts in ethane dehydrogenation. In addition to measuring reaction rates and selectivity, the influence of support material on Cr oxidation state was determined. The reaction was conducted with different residence time to elucidate the carbon formation reaction mechanism from product ethylene over supported Cr catalyst on proton conducting oxides. The influence of water and H_2 on carbon formation during ethane dehydrogenation is discussed.

4.2 Experimental

4.2.1 Sample preparation

$BaCeO_3$ (BC) and $BaZrO_3$ (BZ) powder were synthesized utilizing a modified Pechini method [10,13]. Aqueous solutions of Ba, Ce, Zr (>99% pure, Alfa Aesar, Ward Hill, MA, USA) nitrate salts were prepared and the metal concentration determined by redox titration [14]. The solutions were mixed, in the stoichiometric ratio to fabricate the desired composition, with chelating agent EDTA (99%, Alfa Aesar, Ward Hill, MA) and citric acid monohydrate (99.0-102.0%, Alfa Aesar). The pH was adjusted to > 8.5 by addition of ammonium hydroxide (14.8N, Fisher Scientific) and excess water was evaporated. The resulting homogeneous gel was combusted in

an oven at 300 °C, and the resulting powder sintered for 4h at 1100 °C, or 1300 °C for BC and BZ respectively. Cr catalyst supported on the synthesized pure oxide (0.2-0.6wt-% Cr, denoted 0.2-0.6Cr/BC or BZ in the following) were fabricated using a standard incipient wetness procedure[10,15]. γ-Al_2O_3 (>99% pure, Alfa Aesar, Ward Hill, MA, USA) was employed for Cr catalyst supported on Al_2O_3. Aqueous solution of Cr (>93% pure, Alfa Aesar, Ward Hill, MA, USA) were prepared and the concentration determined by redox titration. 10 wt-% of Cr was deposited on the Al_2O_3 support to maintain approximately constant Cr content per unit surface area of catalyst support between the higher surface area Al_2O_3 and lower surface area perovskite support materials.surface area Al_2O_3 and lower surface area perovskite support materials.

4.2.2 Catalyst characterization

The synthesized materials were characterized by powder X-ray diffraction with Cu Kα radiation and fixed slit width (MiniFlex (II), Rigaku, The Woodlands, TX, USA). Diffraction patterns were recorded in the 2θ range of 20°-70° with a step size of 0.02° and a counting time of 0.2 min/degree. The BET surface area (ASAP2020, micrometrics, Norcross, GA, USA) was measured using N_2 and krypton gas as the absorbent after samples were degassed at 300 °C for 10h. X-ray photoelectron spectra (XPS) measurements were conducted to investigate the oxidation state of supported Cr catalyst. Prior to XPS measurement, samples were oxidized to remove surface contaminants at 800 °C for one hour in a flow of 50mL/min 19.5 – 23.5 vol% O_2/N_2 (GTS-Welco, Allentown, PA,USA), and then reduced at 600°C under flowing 5 vol% H_2 / Ar (UHP gases, < 1ppm O_2, GTS-Welco, Allentown, PA, USA) for one hour.The samples were pressed onto conductive tape with moderate pressure and transferred to a sample holder. The spectra were obtained on a Scienta ESCA-300 with monochromatic X-ray (beam spot, 5mm × 1mm) generated by Al Kα source (E = 1486 eV).

4.2.3 Catalyst testing

Ethane dehydrogenation was conducted with the sieved powder (106-150µm) as a fixed bed in a continuous flow quartz tube reactor. The size of reactor was varied according to sample size for different residence time; i.d. 8mm and 4mm in case of 1g and below 0.2g respectively, with same length of 300mm. Quartz glass wool was used to hold the powder sample in the center of the reactor. Gas flows were regulated by mass flow controllers (Brooks, 4850 series, Exton, PA, USA). Prior to measurement the samples were heated to 800 ^{o}C at a rate of 10 ^{o}C/min in a flow of 100mL/min dry air with < 0.5 ppm CO_2, then held for 1h at this temperature to remove moisture and contaminants on the surface of the powder sample. The powder sample cooled to 600^{o}C under the same flow conditions, and subsequently reduced at 600^{o}C temperature for 1h under flowing 50ml/min 5 vol% H_2 / N_2. The reactor was flushed with nitrogen and cooled to measurement temperature after this pretreatment, prior to feeding the reactant mixture of 5 vol-% Ethane/ N_2 (UHP gases, < 1ppm O_2, GTS-Welco, Allentown, PA, USA) at 150mL/min at measurement temperature. This procedure was repeated with steps of 25 ^{o}C between 475 ^{o}C and 575 ^{o}C.

The concentration of reactants and products were analyzed for 2h at each temperature using on-line gas chromatograph (SRI 8610C, CA, USA) with a 10-port sampling valve and a Haysep D columns. A thermal conductivity detector (TCD) was used to measure the concentration of product eluting from the column. The testing process was also repeated for 0.2Cr/BC using a residual gas analyzer (RGA) fitted with a quadropole analyzer and associated Faraday and secondary electron multiplier detectors (Cirrus 2, MKS Instruments UK Ltd) to qualitatively observe any CO or CO_2 production during the initial few minutes on-stream. To study the influence of residence time, the sample size was varied from 0.1g to 1g. The effect of hydrogen on ethane dehydrogenation was investigated by addition of hydrogen from 1 to 10 vol% into ethane flow. Following reaction at each temperature, the carbon deposited on the sample was measured by a temperature programmed oxidation procedure (TPO) prior to measurement at the

next temperature. The tested samples were cooled to room temperature in flowing N_2 prior to TPO. TPO was performed by flowing 100mL/min 10 vol-% O_2 in Ar through the catalyst and ramping the temperature by 10 ^oC /min from 25 ^oC to 800 ^oC. The CO_2 (m/e=44) concentrations in the reactor effluent was monitored (sampling frequency, $1.67s^{-1}$) using a residual gas analyzer (RGA) fitted with a quadropole analyzer and associated Faraday and secondary electron multiplier detectors (Cirrus 2, MKS Instruments UK Ltd). The amount of deposited carbon was determined by the amount of generated CO_2 calculated from numerical integration of CO_2 peak area. CO_2 peak area was calibrated by using 100μL pulse of CO_2.the deactivated powder sample was burned off by oxidization process at 800 ^oC in a flow of 100mL/min dry air with < 0.5 ppm CO_2.

The reaction rate and ethylene yield were calculated assuming a first order reaction with both being normalized by surface area of loaded powder sample.

$$Y_{C_2H_4}(\%) = \frac{F_{out}[C_2H_4]}{F_{in}[C_2H_6]} \cdot 100\% \quad (4.2.1)$$

Where F_{in} and F_{out} are inlet and outlet molar flow rate. The selectivity to C_2H_4 was determined from Eqs. (2).

$$S_{C_2H_4}(\%) = \frac{[C_2H_4]}{([C_2H_6] + 0.5[CH_4])} \cdot 100\% \quad (4.2.2)$$

Note that only secondary gas product was methane. The ethylene formation rate, $R_{C_2H_4}$ ($molC_2H_4 \cdot m^{-2} \cdot s^{-1}$) of ethane dehydrogenation was evaluated with ethylene yield measured at 1min, normalized the total surface area, S, of the loaded powder sample.

$$R_{C_2H_4} = F_{in}[C_2H_6] \cdot \frac{X_{C_2H_4}}{S}$$

4.3 Results

4.3.1 Catalyst characterization

Figure 4.1 shows the X-ray diffraction patterns of the as-synthesized BC and BZ powders. The patterns for BC and BZ were indexed to an orthorhombic perovskite (space group *Pmcn*) [16-19] and a cubic perovskite structure (space group *Pm-3m*) [20-22], respectively. Note that BC will transform to a cubic structure at the reaction temperatures of interest in this study[17]. XRD analysis could not detect a Cr phase on the supported Cr catalysts due to the low loading. BET surface areas ranged from 1.67 m^2/g for 0.6Cr/BZ to 3.16 m^2/g for 0.2Cr/BC, Table 1. . These give Cr coverages of 0.19, 0.1 and 0.11g/m^2 for 10CrAl, 0.2Cr/BZ and 0.2Cr/BC respectively. The measurement using krypton gas as an absorbent showed 10% lower surface area; 1.89 and 2.20 m^2/g for 0.2 and 0.4 Cr/BZ.

4.3.2 Catalytic performance of Cr/BZ and Cr/BC

Prior to ethane dehydrogenation with catalyst, the possibility of gas-phase homogeneous dehydrogenation was investigated with a blank reactor, including only quartz wool, in the temperature range of 25 - 750 ^oC. no ethane conversion was observed below 650 ^oC; the conversion increased to 3% at 700 ^oC. Similarly, no C_2H_4 formation was observed over 1g of pure BC and BZ support at temperatures below 600 ^oC. The ethane conversion was 0.3% under these conditions and is attributed to a small amount of carbon deposition on the bare support. The low activity over and minimal carbon deposition on the bare support materials indicates that the support materials are inactive for the desired reaction.

Figure 4.2 shows ethylene yield as a function of time over 1g of 0.2Cr/BZ and 0.2Cr/BC. Note that the ethylene yield reported in the figure is for gas-phase products only and is normalized by the total surface area of the powder sample. The initial ethylene yield, measured at one minute on-stream, increased with increasing temperature for all catalysts. For example, the

Sample	Support	Al	BZ			BC		
	Cr loading (wt %)	10	0.2	0.4	0.6	0.2	0.4	0.6
Surface area (m^2/g)		53.7	2.01	2.48	1.67	3.16	2.4	1.76

Table 4.1BET surface areas.

Sample	10CrAl	0.2Cr/BZ	0.2Cr/BC
Surface concentration of Cr (at. %)	1.2	1.5	0.7
Cr^{+6} $2p_{3/2}$	580.4 eV	-	578.9 eV
Cr $2p_{1/2}$	587.7 eV	587.2 eV	587.4 eV
Cr^{+3} $2p_{3/2}$	577.9 eV	577.5 eV	577.3 eV
Cr^{6+}/Cr^{3+}	0.47	0	0.26

Table 4.2 XPS data

Figure 4.1 X-ray diffraction patterns of (a) BZ, (b) 0.6Cr/BZ, (c) BC and (d) 0.6Cr/BC

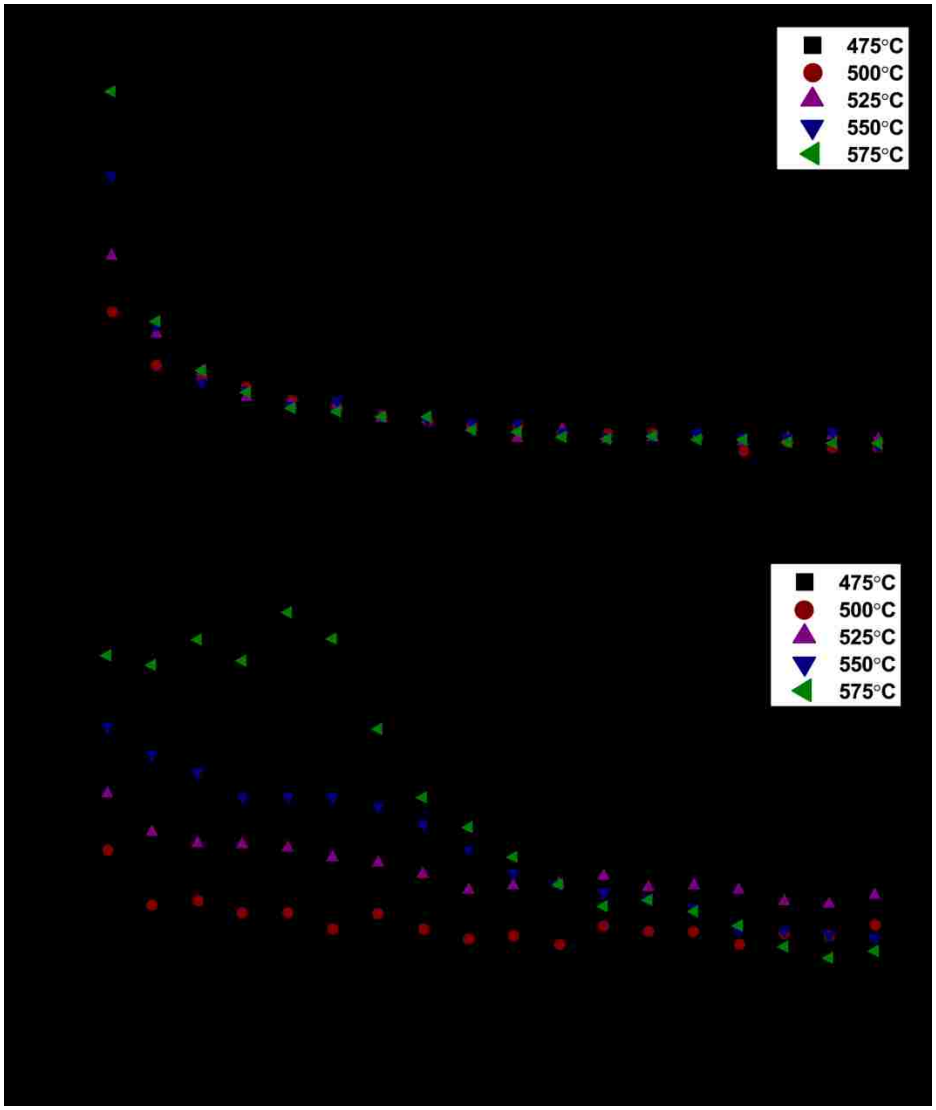

Figure 4.2 Normalized ethylene yields versus time on stream over a) 0.2Cr/BZ and b) 0.2Cr/BC

yield over 0.2% Cr/$BaZrO_3$ was 0.8, 1.2, 1.6, 2.2 and 2.9 % at 475, 500, 525, 550 and 575 ^oC, respectively. As can be observed for 0.2Cr/BZ in Figure 4.2, all of the BZ samples showed rapid deactivation over the two-hour testing period. In contrast, the BC supported catalysts all showed a more gradual deactivation, particularly as the temperature is increased. This is shown in Figure 4.2b, where the 0.2Cr/BC sample is relatively stable for the first 40 minutes.

The C_2H_4 formation rate was calculated from the ethylene yield measured at 1 minute on-stream for all of the catalysts, Figure 4.3. At constant Cr loading, the rates observed for the BZ support were higher than those for BC. In addition, higher Cr loading generally leads to higher formation rate for both supports. The formation rates were 8.3×10^{-8}, 1.0×10^{-7} and 1.2×10^{-7} $mol/m^2 \cdot s$ for 0.2, 0.4 and 0.6Cr/BZ at 525 ^oC, 4.8×10^{-8}, 6.7×10^{-8} and 1.0×10^{-7} $mol/m^2 \cdot s$ for 0.2, 0.4 and 0.6Cr/BC. It is further observed that the activation energy of supported Cr catalysts on BZ was greater than that on BC.

The gas phase hydrocarbon product selectivity to C_2H_4 for each catalyst was calculated for the 1 minute on-stream data, Figure 4.4. The only other gas phase products detected were CH_4 and H_2. The C_2H_4 selectivity of Cr/BZ was maintained above 98%, whereas that of Cr/BC decreased with increasing temperature but was still above 90%. For example, the C_2H_4 selectivity of 0.2Cr/BZ was 99.3, 98.7 and 99.3% at 525, 550 and 575^oC, that of 0.2Cr/BC was 97.6, 97.3 and 94.9. Note that the C_2H_4 selectivity rose with time on stream, reaching 100% at 7 and 30min on stream for BZ and BC, respectively.

As mentioned previously, the selectivity shown in Figure 4.4 is for gas phase products and does not account for carbonaceous deposits. Carbon tolerance is another significant criterion to evaluate the catalysts for potential industrial application. This was evaluated by performing TPO experiments to quantify the amount of carbon deposited; an example of the TPO data is provided in Figure 4.5(a). In all cases, CO_2 evolution was observed as a single peak with a maximum at ~350^oC. This suggests that the deposited carbon is not graphitic. The calculated amount of carbon

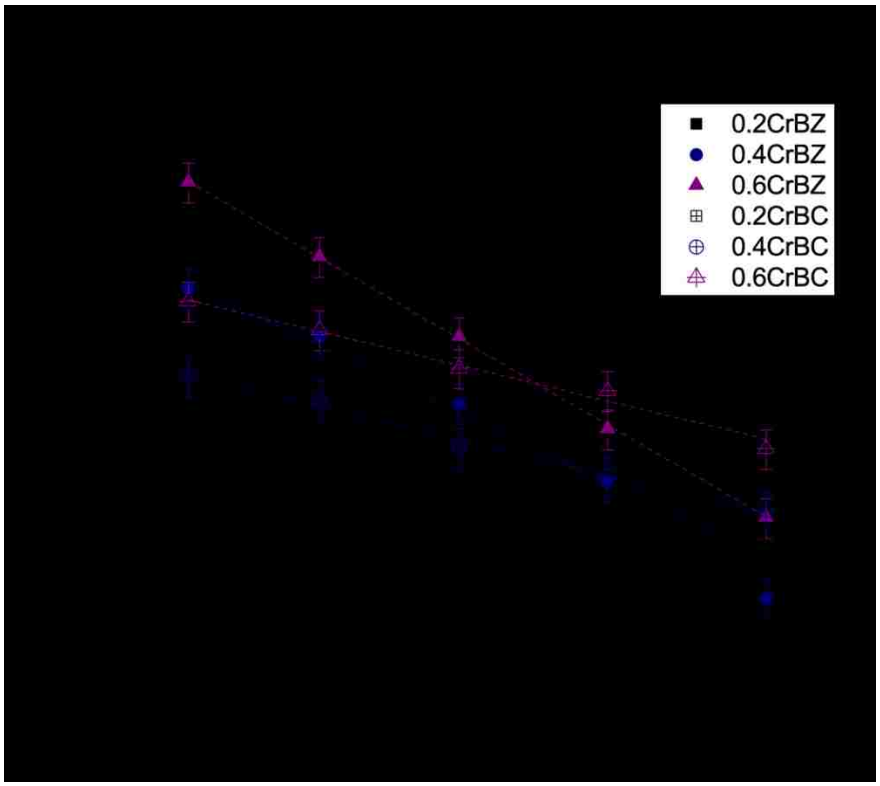

Figure 4.3 Arrhenius plot of ethylene formation rate over Cr/BZ and Cr/BC at 1 minute on-stream.

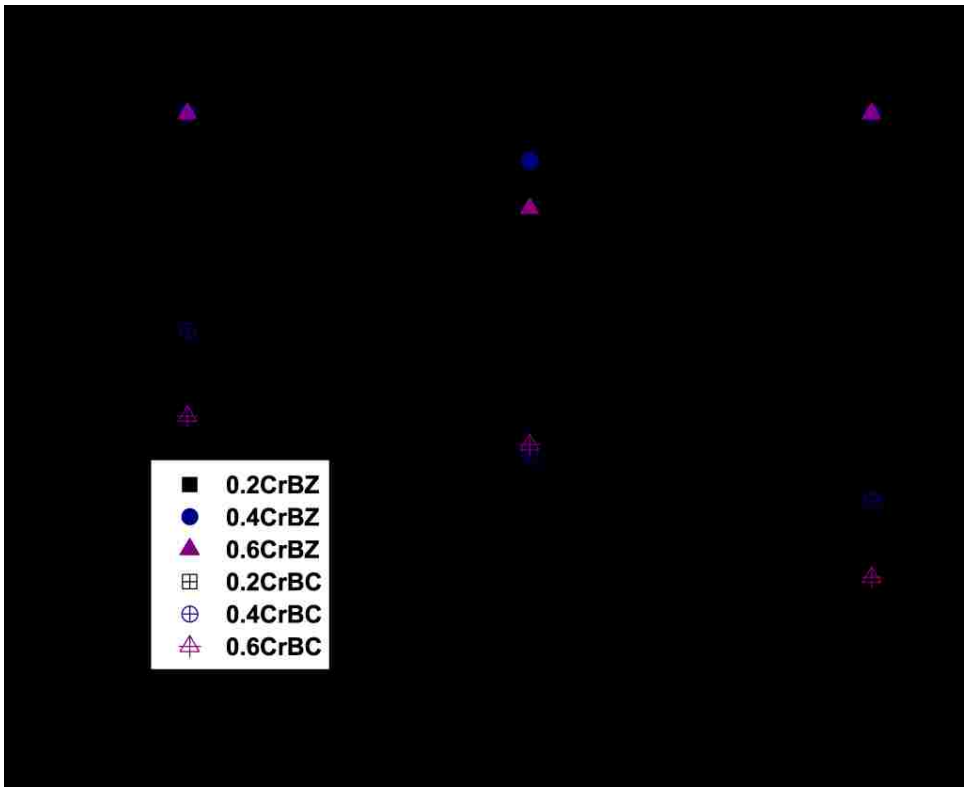

Figure 4.4 Selectivity to ethylene over Cr/BZ and Cr/BC as a function of temperature at 1 minute on-stream

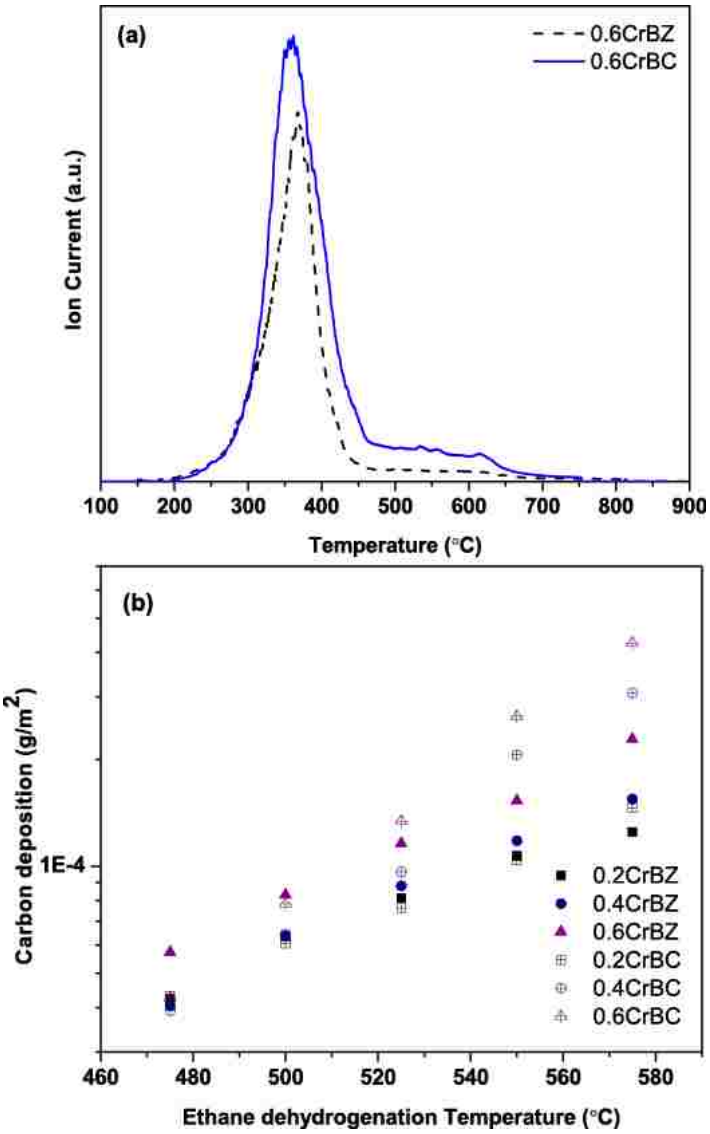

Figure 4.5 a) Temperature programmed oxidation (TPO) data showing CO2evolution (m/e=44) of carbon deposited during ethane dehydrogenation over 0.6Cr/BZ and 0.6Cr/BC at 575°C. b) Amount of carbon deposited (g/m2) over Cr/BZ and Cr/BC as a function of temperature.

deposited on Cr catalysts determined by TPO was normalized by total surface area of the powder sample, Figure 4.5(b). The amount of carbon deposited on all Cr catalysts exponentially increased with increasing temperature, supported Cr catalysts on BC showed significantly larger amount of carbon deposited than that on BZ. For example, the amount of carbon deposited on 0.2, 0.4 and 0.6 Cr/BC were 1.46, 2.88 and 3.97×10^{-4} g/m^2, that for BZ were 1.25, 1.55 and 2.28×10^{-4} g/m^2. The normalized conversion of total ethane feed to coke formation was calculated; the normalized conversion for 0.2, 0.4, 0.6 Cr/BZ were 1.42, 1.76 and 2.60×10^{-2} %, that for 0.2, 0.4, 0.6 Cr/BC were 1.67, 3.28 and 4.53×10^{-2} %. It should be noted that the deactivation time between CrBZ and CrBZ were quite different, thus direct comparison was not available. Note that small amount of CO (m/e=28) was detected in the TPO experiment, this was expected from fragmentation of CO_2 in the mass spectrometry.

4.3.3 The influence of residence time

Figure 4.6 (a) and (b) show the influence of residence time on ethane dehydrogenation with 0.6Cr/BC at 575°C. The initial measurement was conducted at 1min in regardless of variation of residence time. Figure 4.6(a) shows that the C_2H_4 formation at 1min increased with decreasing residence time. The ethylene yields at 1min were 2.8, 8.6, 10.2 and 30.9 % for the residence time of 0.63, 0.31, 0.13 and 0.06 sec, respectively. In contrast, no significant difference of yield was observed between different residence times after 60 minutes on-stream due to catalyst deactivation.

The C_2H_4 formation rate, selectivity and carbon deposition are shown as a function of residence time in Figure 4.6 (b). The increase of residence time leads to significant decrease of the ethylene formation rate and increase of carbon deposition up to 0.31sec. For example, the formation rates of 0.6Cr/BC were 1.57×10^{-6} and 2.2×10^{-7} mol/m^2·s for the residence time of 0.06 and 0.31 sec, respectively, the amounts of carbon deposited 3.0 and 3.9×10^{-4} g/m^2. At longer residence time than 0.31 sec, no significant further variation in the ethylene formation rate

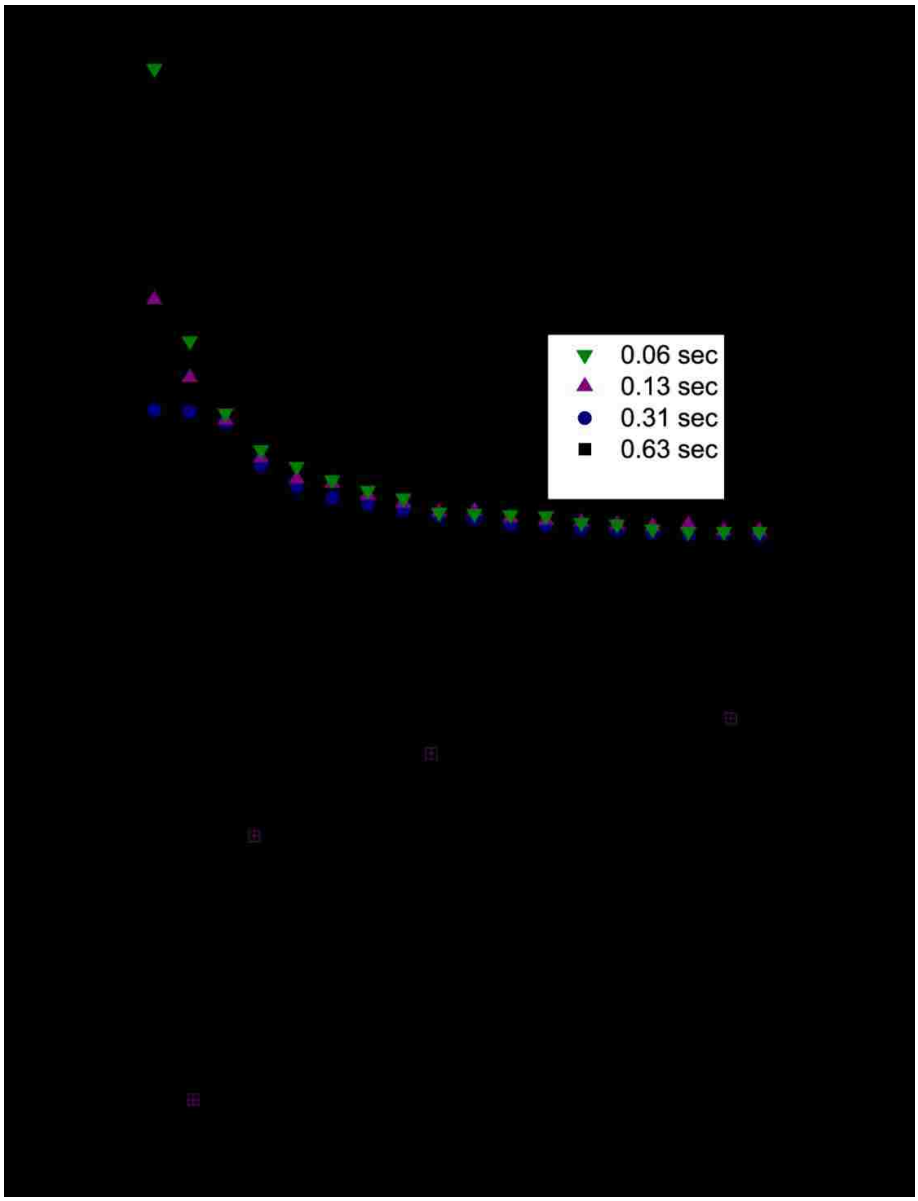

Figure 4.6: a) Normalized ethylene yields versus time on stream over 0.6CrBC at different residence time; 0.06, 0.13, 0.31 and 0.63 sec at 575oC. b) Ethylene formation rate and the amount of carbon deposited as a function of residence time at 575oC.

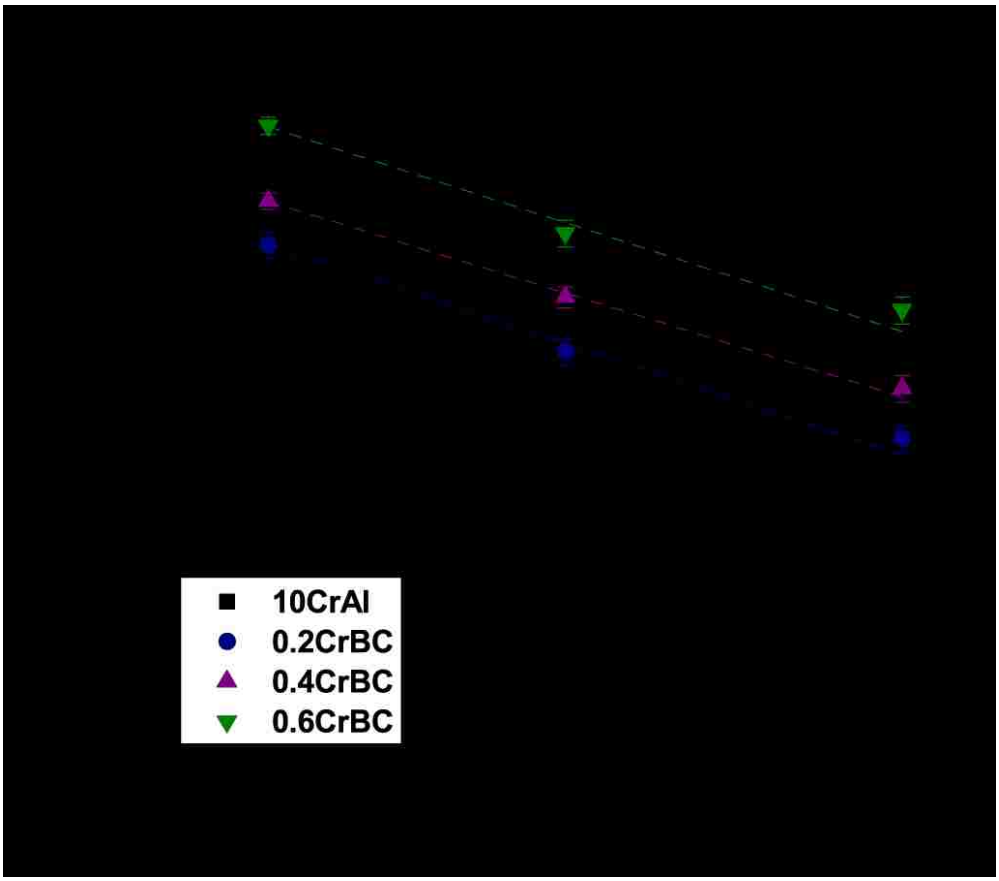

Figure 4.7 Arrhenius plot of ethylene formation rate over Cr/BC and 10CrAl at residence time of 0.13 sec.

and carbon deposition was observed. C_2H_4 selectivity fell approximately linearly with increasing residence time from 100 to 94%, indicating that methane formation rate also increases.

Ethane dehydrogenation was conducted with Cr/BC of 0.2g, residence time of 0.13 sec, the ethylene formation rate was shown as an inverse function of temperature in Figure 4.7. It might seem that there is no difference in temperature dependency of the formation rate between residence time of 0.63 sec and 0.13 sec, but higher temperature dependence of C_2H_4 formation rate was observed in the residence time of 0.13 sec. This supported Cr catalyst on BC was compared with 10 wt-% Cr supported on γ-Al_2O_3 catalyst (10CrAl), which was fabricated in same way as Cr/BC; incipient wetness procedure[10,15]. The ethylene formation rates of 10CrAl were 9.2 $\times 10^{-9}$, 2.9$\times 10^{-8}$, 7.4$\times 10^{-8}$ $mol/m^2 \cdot s$ at 475, 525 and 575 ^oC, these rates were about one order of magnitude lower than 0.6Cr/BZ. The calculated apparent activation energy was 26.3 kcal/mol. This has good agreement with pervious report[8], where 27.5 kcal/mol was obtained in Cr/SiO_2.

4.3.4 The influence of H_2 addition on carbon deposition

Various groups have sought to inhibit carbon deposition by addition of H_2, H_2/O_2, CO_2 or H_2O to the reactor feed [8,23-26]. Figure 4.8 (a) shows the effect of H_2 addition to the feed at varying H_2 content ranging from 0 to 10 vol-% for 0.2g of 0.6Cr/BC at 575 ^oC, residence time of 0.13 sec. In initial measurement at 1min, an increase of H_2 partial pressure results in a decrease of ethylene yield; 15.9, 9.8, 8.5, 8.2, 6.0 and 5.5% for 0, 1, 3, 5, 7 and 10 vol-% H_2, respectively. In contrast, steady state catalytic activity at after 60min shows quite different trend; the yields at 120min 0.8, 0.8, 1.3, 1.8, 2.2 and 2.5%. Note that this is in contrast to the same deactivated rate for all catalysts in the absence of H_2 in the feed.

It should also be noted that for H_2 addition above 5 vol-%, there is a delay in the onset of deactivation, observable as a plateau or increase in yield as a function of time on stream at short times. In addition, H_2 addition leads to a decrease in C_2H_4 selectivity; 99.1, 95.4, 93.7, 91.5, 89.4

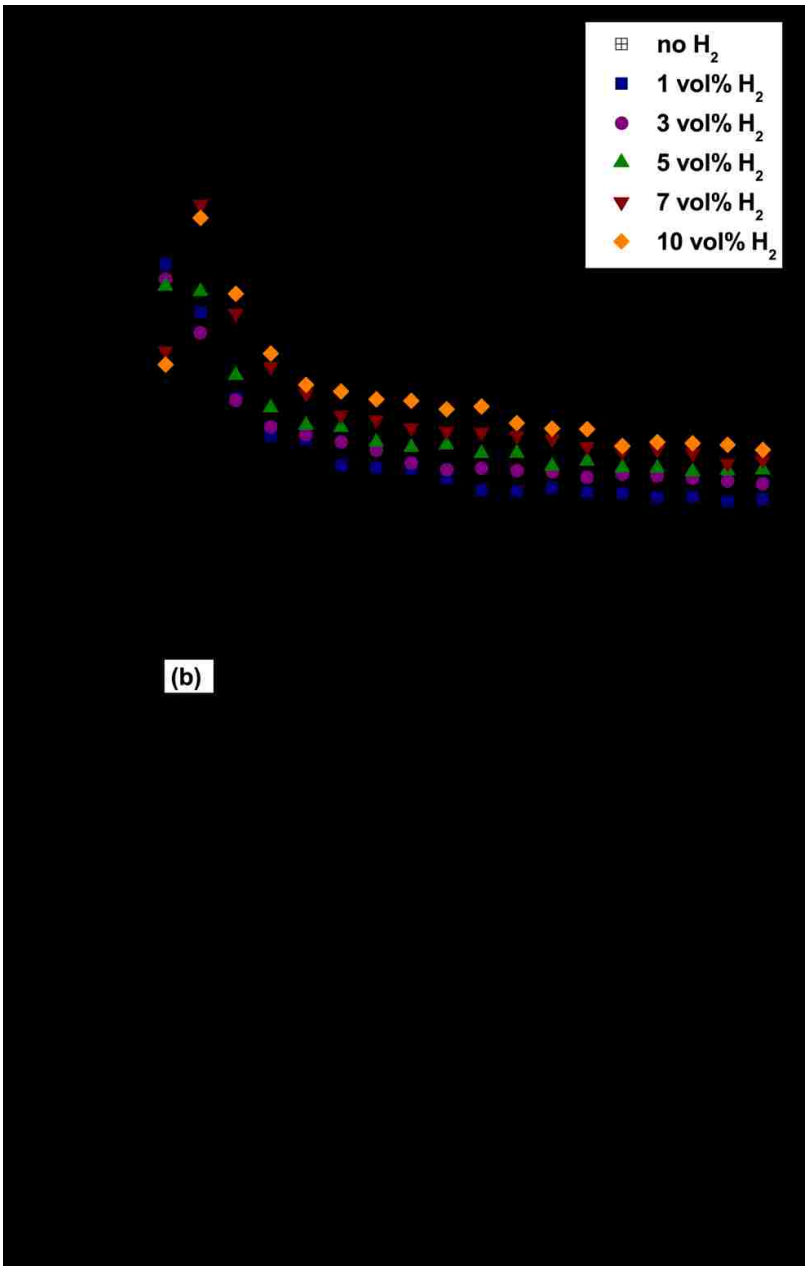

Figure 4.8 a) Normalized ethylene yields versus time on stream over 0.6CrBC at 575 °C in the presence of H2. b) The amount of carbon deposition and selectivity to ethylene at 1minute on-stream (inserted figure) as a function of concentration of H2,

and 87.4 % for 0, 1, 3, 5, 7 and 10 vol-% H_2 addition. TPO was conducted to investigate the amount about carbon deposited on Cr catalysts as a function of H_2 vol-%, Figure 4.8(b). Carbon deposition significantly decreases with increasing H_2 content until 5 vol-% H_2. The amounts of carbon deposited after ethane dehydrogenation for 2hr were 3.7, 2.6, 1.95 and 1.74×10^{-4} g/m^2 for 0, 1, 3 and 5 vol % H_2. No further decrease of carbon deposition was observed above 5 vol-% H_2.

4.3.5 XPS measurement

XPS measurement was performed to investigate the oxidation state of Cr in 0.2Cr/BC, 0.2Cr/BZ and 10CrAl, Figure 4.9. The sample pretreatment prior to XPS was the same as prior to the catalytic function tests. All Cr 2p spectra were comprised of two main peak with binding energy of ~577 and 586 eV, associated with Cr $2P_{3/2}$ and Cr $2P_{1/2}$ photoelectrons, respectively. As shown in Figure 4.9, Cr^{+3} Cr $2P_{3/2}$ overlaps with Cr^{+6} Cr $2P_{3/2}$ in the XPS spectra, thus these were de-convoluted using the CasaXPS program by curve fitting with the mixed Gaussian-Lorentzian peaks. For 0.2Cr/BZ, only one symmetric Cr $2P_{3/2}$peak was observed at 577.5, indicating the presence of only one chemical state; Cr^{3+}. In contrast, 10CrAl and 0.2Cr/BC show an additional peaks characteristic of Cr^{6+} Cr $2P_{3/2}$ at the binding energy of 580.4 and 578.9 eV, respectively[27-29]. The presence of this peak is clear in the 10CrAl sample and is observed as an asymmetry in the 0.2Cr/BC peak at the expected position for the Cr^{6+} Cr $2P_{3/2}$ [27-30]. The XPS derived surface concentration of atomic Cr and the ratios of different chromium oxidation state were summarized in table 2. The ratio was calculated by measuring the area of de-convoluted Cr species' characteristic peak. Due to the low signal-to-noise ratio for the XPS data on 0.2Cr/BC, we also utilized an RGA to probe for Cr^{6+} by observing trace CO_2 production during the initial stages of the reaction over a fresh catalyst. While still not completely conclusive, the combination of these results strongly suggests that Cr^{6+} is present on the fresh 0.2Cr/BC catalyst.

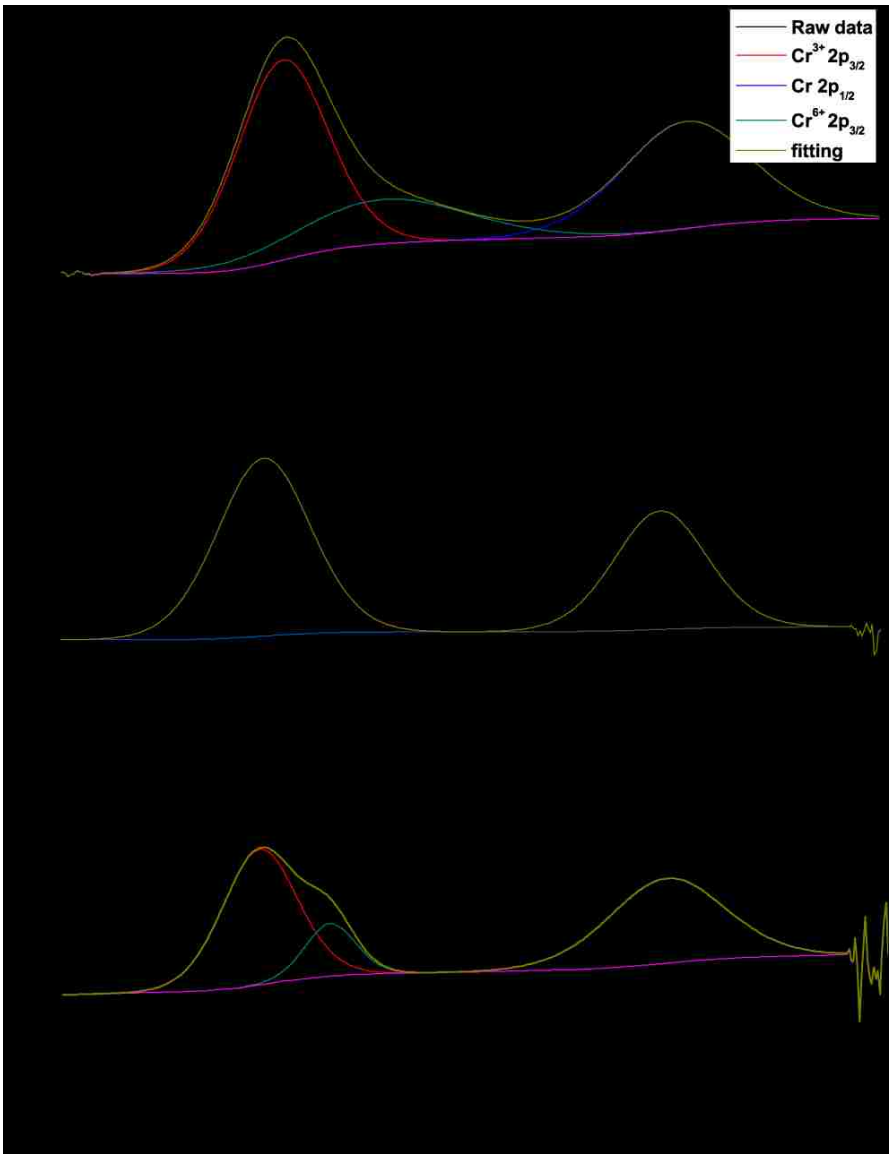

Figure 4.9 XPS spectra for a) 10Cr/Al b) 0.2Cr/BZ and c) 0.2Cr/BC.

4.4 Discussion

Proton conducting oxides, $BaZrO_3$ (BZ) and $BaCeO_3$ (BC) were tested as support materials for Cr catalyst for ethane dehydrogenation. As shown in Figure 4.1, it was demonstrated that pure perovskite crystal structure was obtained; Cr was not observed in supported Cr catalyst (Cr/BZ and Cr/BC) due to low amount of Cr loaded (0.2-0.6wt-%), Figure 4.1(b) and (d). No detrimental effect of the incipient wetness synthesis method on crystal structure was observed below 5 wt-% Cr loading, indicating compatibility of BZ and BC with Cr catalyst.

Our results demonstrate the promise of proton conducting ceramic supports for Cr catalysts in ethane dehydrogenation. In Figure 4.7, the BC-supported catalyst shows more than one order of magnitude higher C_2H_4 formation rate than the 10 wt-% Cr/Al_2O_3 catalyst reported herein, and the 0.5 wt-% Cr on Al_2O_3 supported catalyst reported by Lugo et al[8]. While these catalysts have different total Cr contents, the Cr surface concentrations for both the catalysts in this study were comparable; 0.19 and 0.11g/m^2 for 10CrAl and 0.2Cr/BC respectively. Furthermore, XPS derived Cr atomic surface concentration were 1.2 and 0.7 at-% for the same samples, Table 2. Note that all of the catalysts show high selectivity to ethylene, over 94% of the gas phase product within all range of residence time utilized in this study, indicating that in all cases dehydrogenation of surface CH_3* is more rapid than hydrogenation to CH_4.

We then turn to possible reasons for this higher activity. Lugo et al[8] suggested that similar catalytic activity between Cr/Al_2O_3 and Cr/SiO_2 indicates no significant electronic effect of these supports on the Cr active phase. In contrast, our results clearly show a significant influence of support on Cr in terms of C_2H_4 formation rate, selectivity, and carbon deposition. We propose that the observed higher activity of Cr/BZ compared with Cr/BC can be explained by the XPS data, where the existence of Cr^{6+} was observed only in Cr/BC. This is in agreement with the conclusion of Lugo et al. that more reduced Cr catalysts lead to higher catalytic activity in ethane

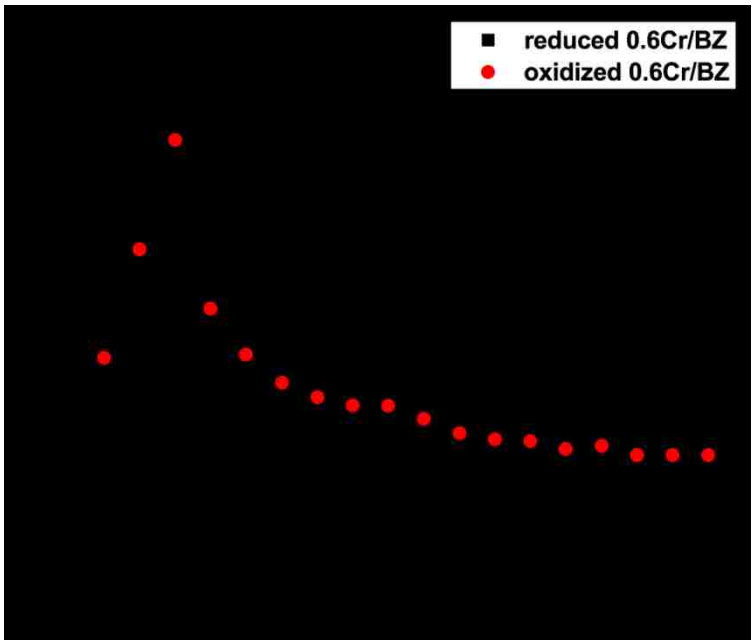

Figure 4.10 Normalized ethane conversion to ethylene versus time on stream over reduced 0.6Cr/BZ and oxidized 0.6Cr/BZ

dehydrogenation. Note that oxidized Cr/BZ showed significantly low ethane conversion to ethylene compared to the reduced one at initial measurement, figure 4.10.

The conversion rapidly increased for first 20 min, then decreased. This implies that the initial state of Cr prior to reduction in hydrogen was mostly Cr^{6+}, which over BZ was easily reduced to Cr^{3+} by hydrogen as by-product of ethane dehydrogenation or deposited carbon. Our XPS results also indicate that Cr might be reduced more easily on BZ than BC.

Our initial hypothesis in this study was that the ability of a proton conducting support to incorporate protons into the bulk may enhance the observed rates for ethane dehydrogenation. We have previously demonstrated that proton incorporation in these materials occurs via hydrogen dissociation on a metal, followed by spill-over onto the oxide surface, with subsequent incorporation into the oxide[10]. We suggest that facile proton transport to and within the proton conducting support materials plays a role in enhancing the observed rate, suggesting the possibility of a proton analogy to a Mars-van Krevelen mechanism. This our hypothesis could also be supported by Galvita et al.'s reports[9] showing that low concentrations of adsorbed hydrogen promoted ethane dehydrogenation by promoting removal of hydrogen from surface ethyl group, C_2H_5*. In our case, it could be that a mobile bulk proton may play a similar role to the adsorbed hydrogen; however, this hypothesis requires further investigation with different supports and a wider range of reactions and reaction conditions to be proven conclusively.

A significant difference between the two proton conducting supports is the relatively gradual deactivation observed for Cr/BC when compared with Cr/BZ, Figure 4.2. At the highest measurement temperature, the Cr/BC catalyst shows no deactivation until 40 minutes on-stream. In contrast, the Cr/BZ catalyst deactivates rapidly. One possibility is that the BC catalyst is more resistant to carbon deposition; however, our TPO results indicate that significantly more carbon was deposited on Cr/BC than Cr/BZ, suggesting that this is not the case. A somewhat similar trend was observed by Olsbye et al[31], who studied ethane dehydrogenation over Cr/Al_2O_3 and

found a maximum in ethylene yield after 10min on-stream. One proposed theory is that large surface hydrocarbons are active for ethane dehydrogenation[32]. However, Olsbye et al[31] conducted Isotopic labeling experiments to demonstrate that this is not the case.

A delayed maximum in ethylene yield was also observed in propane dehydrogenation over Cr/Al_2O_3 [33]. In the study, operando UV-vis spectra showed a decrease of Cr^{6+} CT band with increasing time on-stream, with a simultaneous increase in Cr^{3+} d-d transition band, implying reduction of CrO_3 to Cr_2O_3. We propose that observed relative stability and sustained high ethylene yield observed for Cr/BC, especially at 575 ^oC, is related to the reduction of Cr reduction from Cr^{6+} to Cr^{3+}. This is supported by the XPS data for our samples showing the presence of Cr^{6+} only in Cr/BC; the Cr/BZ catalyst deactivates more rapidly and does not show any Cr^{6+}.

It is not clear if Cr^{6+} is reduced to Cr^{3+} by adsorbed hydrogen or deposited carbon since hydrogen is also produced in ethane dehydrogenation. Nijhuis et al.[33] reported that a small amount of CO_2 was observed by mass spectrometer at the beginning of propane dehydrogenation, mentioning that the CO_2 is formed by the reduction of Cr^{6+} to Cr^{3+}. Any observation of water was not mentioned. In our experiment, simultaneous production of not only small (less than ~ 0.1 vol-%) amounts of CO_2 but also H_2O was detected by mass spectrometry at short times on-stream. Thus it is not clear whether the primary reducing agent is adsorbed hydrogen or carbon. Since our samples were reduced in hydrogen prior to reaction, it seems more likely that carbon is the reducing agent upon introducing ethane.

We then turn to the source of the carbon; directly from ethane or via secondary reaction of product ethylene. Varying the reactor residence time for the Cr/BC catalyst facilitates insight into this process. As the residence time decreases, the amount of product ethylene increases, and the amount of carbon deposited decreases. This suggests that carbon formation is more likely from product ethylene than directly from ethane. Furthermore, Galvita et al.[9] reported that methane formation from product ethylene is more rapid than directly from ethane over supported platinum

over calcined hydrotalcite in the presence of hydrogen, also supporting carbon formation from product ethylene. It should be noted that methane formation directly from ethane prevails in the absence of hydrogen. We carefully propose that hydrogenolysis of ethane might be prevented by proton in oxide, methane and carbon is formed from product ethylene. Therefore, we propose that short contact time is required to optimize ethylene production through inhabitation of secondary reaction of ethylene[4].

Several researchers have investigated how to suppress carbon deposition; for example, addition of H_2O[4] and CO_2 were tried by Lugo et al[8], where water only leads to more rapid deactivation, with no effect of CO_2. Carbon formation rapidly deactivates these catalyst systems, requiring costly cyclic regeneration if this system were to be employed industrially; in our limited cycling the catalyst shows no degradation. Decreased carbon deposition was reported by Galvita et al.[9] upon addition of H_2 to the ethane feed. We examined the influence of H_2 addition on 0.2g of 0.6Cr/BC in the concentration ranging from 0 to 10 vol% in 10% ethane/N_2 feed. Our results are in agreement with the literature[9]. Increasing concentration of H_2 leads to the decreases in initial ethylene yield and selectivity to ethylene, while increased steady state activity. Galvita et al.[9] reported that excess amount of adsorbed hydrogen plays a detrimental role for ethylene formation since it increases the back formation of ethane from C_2H_5*, and hydrogenation of CH_3* to form methane. Our result also shows decrease of the selectivity to ethylene with increasing H_2 contents to 87.4% at 10 vol% H_2. Our experiment using co-fed water into reactant has only detrimental effect on ethane dehydrogenation; significantly lower ethylene production was observed. This has good agreement with Lugo et al[8] and our previous report[10].

4.5 Conclusion

This study clearly demonstrates the potential of proton conducting oxide as a Cr catalysts supports for short contact time ethane dehydrogenation. At residence time 0.13 sec, 0.6Cr/BC

showed more than one order of magnitude higher ethylene formation rate compared to 10Cr/Al in our study, and 0.5% Cr/Al in the literature. XPS measurement indicated that Cr^{3+} is the most active oxidation state for ethane dehydrogenation, and that this oxidation state is more prevalent on a barium zirconate support when compared to barium cerate; however, our results indicate that this is likely rapidly reduced by carbon, leading to a decrease in ethylene formation rate. A significant decrease in ethylene yield and selectivity to ethylene, and increasing carbon deposition, with increasing residence time indicates that product ethylene can be consumed by secondary reactions to form carbonaceous deposits. Addition of H_2 into the reactant feed resulted in the resistance to carbon deposition at the expense of a slight decrease in conversion and selectivity to ethylene. While all of the samples showed deactivation due to coke, the use of the higher activity barium cerate or barium zirconate support materials could enable commercial productivity to be maintained at reduced operating temperatures with associated reduced carbon deposition rates.

4.6 References

1. Bhasin, M. M.; McCain, J. H.; Vora, B. V.; Imai, T.; Pujadó, P. R. *Applied Catalysis A: General* **2001**, *221*, 397-419.

2. Shen, W.; Wang, Y.; Shi, X.; Shah, N.; Huggins, F.; Bollineni, S.; Seehra, M.; Huffman, G. *Energy Fuels* **2007**, *21*, 3520-3529.

3. Shah, N.; Wang, Y.; Panjala, D.; Huffman, G. P. *Energy & Fuels* **2004**, *18*, 727-735.

4. Huff, M.; Schmidt, L. D. *J. Phys. Chem.* **1993**, *97*, 11815-11822.

5. Bañares, M. A. *Catalysis Today* **1999**, *51*, 319-348.

6. Weckhuysen, B. M.; Wachs, I. E.; Schoonheydt, R. A. *Chem. Rev.* **1996**, *96*, 3327-3350.

7. Weckhuysen, B. M.; Schoonheydt, R. A. *Catalysis Today* **1999**, *51*, 223-232.

8. Lugo, H. J.; Lunsford, J. H. *Journal of Catalysis* **1985**, *91*, 155-166.

9. Galvita, V.; Siddiqi, G.; Sun, P.; Bell, A. T. *Journal of Catalysis* **2010**, *271*, 209-219.

10. Shin, H. H.; McIntosh, S. *J. Mater. Chem. A* **2013**, *1*, 7639.

11. Shin, H. H.; McIntosh, S. *ECS Electrochemistry Letters* **2013**, *2*, F88-F91.

12. Norby, T. *Solid State Ionics* **1999**, *125*, 1-11.

13. H. E. van Doorn, R.; Kruidhof, H.; Nijmeijer, A.; Winnubst, L.; J. Burggraaf, A. *J. Mater. Chem.* **1998**, *8*, 2109-2112.

14. Vogel, A. *Textbook of Quantitative Inorganic Analysis;* Longman Scientific and Technical: Longman, Harlow, United Kingdom, 1986; .

15. Levy, P.; Primet, M. *Applied Catalysis* **1991**, *70*, 263-276.

16. Knight. Kevin S.; Bonanosb. Nicholas *Journal of Materials Chemistry* **1994**, *4*, 899-901.

17. Knight. K.S. *Solid State Ionics* **2001**, *145*, 275-294.

18. Takeuchi, K.; Loong, C. K.; Richardson Jr., J. W.; Guan, J.; Dorris, S. E.; Balachandran, U. *Solid State Ionics* **2000**, *138*, 63-77.

19. Glöckner, R.; Islam, M. S.; Norby, T. *Solid State Ionics* **1999**, *122*, 145-156.

20. Stokes, S. J.; Islam, M. S. *J. Mater. Chem.* **2010**, *20*, 6258-6264.

21. Braun, A.; Duval, S.; Ried, P.; Embs, J.; Juranyi, F.; Strässle, T.; Stimming, U.; Hempelmann, R.; Holtappels, P.; Graule, T. *J. Appl. Electrochem.* **2009**, *39*, 471-475.

22. Duval, S. B. C.; Holtappels, P.; Vogt, U. F.; Stimming, U.; Graule, T. *Fuel Cells* **2009**, *9*, 613-621.

23. Virnovskaia, A.; Rytter, E.; Olsbye, U. *Ind. Eng. Chem. Res.* **2008**, *47*, 7167-7177.

24. Yu, C.; Ge, Q.; Xu, H.; Li, W. *Ind. Eng. Chem. Res.* **2007**, *46*, 8722-8728.

25. Tasbihi, M.; Feyzi, F.; Amlashi, M. A.; Abdullah, A. Z.; Mohamed, A. R. *Fuel Process Technol* **2007**, *88*, 883-889.

26. Kogan, S. B.; Schramm, H.; Herskowitz, M. *Applied Catalysis A: General* **2001**, *208*, 185-191.

27. Rao, T. V. M.; Yang, Y.; Sayari, A. *Journal of Molecular Catalysis A: Chemical* **2009**, *301*, 152-158.

28. Rao, T. V. M.; Zahidi, E. M.; Sayari, A. *Journal of Molecular Catalysis A: Chemical* **2009**, *301*, 159-165.

29. Xing, T.; Wan, H.; Shao, Y.; Han, Y.; Xu, Z.; Zheng, S. *Applied Catalysis A: General* **2013**, *468*, 269-275.

30. Cavani, F.; Koutyrev, M.; Trifirò, F.; Bartolini, A.; Ghisletti, D.; Iezzi, R.; Santucci, A.; Del Piero, G. *Journal of Catalysis* **1996**, *158*, 236-250.

31. Olsbyea, U.; Virnovskaiaa, A.; Prytza, Ø .; Tinnemansb, S. J.; Weckhuysen, B. M. *Catalysis Letters* **2005**, *103*, 143-148.

32. Mestl, G.; Maksimova, N. I.; Keller, N.; Roddatis, V. V.; Schlögl, R. *Angewandte Chemie International Edition* **2001**, *40*, 2066-2068.

33. Nijhuis, T. A.; Tinnemans, S. J.; Visser, T.; Weckhuysen, B. M. *Phys. Chem. Chem. Phys.* **2003**, *5*, 4361-4365.

5. High elective CO_2 methanation over supported Co and Pt nanoparticles on proton conducting $BaZrO_3$

5.1 Introduction

Carbon dioxide (CO_2) is very stable; nonflammable and nontoxic, and vast resources, while CO_2 has received great attention as anthropogenic greenhouse-gases warming up the globe, even the concentration of CO_2 in atmosphere is steadily increasing every year as a result of fossil fuel combustion for energy production[1,2]. With reference to this, the international energy oulook (2011) estimated the 53 percent increase in world energy consumption from 2008 to 2035[3]. Thus, as abundant resources, CO_2 utilization for production of substitute natural gas has great environmental and industrial potential due to the reduction of CO_2 buildup as well as replacement of part of the fossil fuel consumption[4]. In this sense, CO_2 methanation is of considerable current interest as a central strategy for fossil fuel replacement to mitigate the recent crude oil crisis[5].

Cobalt based catalyst has been identified to be active for CO_2 hydrogenation[6,7], this catalysts were observed to be promoted by platinum and other precious metals for CO and CO_2 hydrogenation[8]. Recently, the kinetic study was conducted using size and morphology controlled cobalt and platinum nanoparticle supported mesoporous silica to investigate the reaction mechanism, the effect of catalyst size and the introduction of promoter such as Pt[9-11]. This study showed that the individual size controlled Co and Pt nanoparticles resulted in the significant enhancement in CO_2 methanation rather than bimetallic particle, suggesting that the spillovered hydrogen reduce the surface oxide formed on the Co by the CO_2 dissociation step in the reaction. Also, the significant drop in apparent activation energy was observed by Pt addition, implying the kinetic change of CO_2 methanation to transport limited.

In addition to hydrogen migration onto the surface of supports, the particle dispersion, size distribution and oxidation state of metal catalyst also depends on support materials [7,10]. Like this, catalyst supports plays an important role in heterogeneous catalysis. We have clearly demonstrated the significant influence of supports on Cr catalyst in non-oxidative ethane dehydrogenation where proton conducting $BaCeO_3$ and $BaZrO_3$ were utilized as supports for Cr catalysts, showed more than 1 order of magnitude higher ethylene formation rate in comparison to those of supported Cr over γ-Al_2O_3[12]. This enhancement in catalytic activity was explained by facile proton incorporation in proton conducting oxide occurred via hydrogen dissociation on a metal, followed by spillover onto the oxide surface[13].

In this study, we examined the possibility of a proton conducting oxide as a support material for Co catalyst in CO_2 methanation. Also, Size controlled individual Co and Pt nanoparticle was employed to minimize the extra effect of metal catalyst; such as size and dispersion, on the reaction. As a standard support material, γ-Al_2O_3 was employed and compared with proton conducting oxide[14]. We clearly identified that introduction of proton conducting oxide as supports for Co and Pt catalyst in CO_2 methanation resulted in significantly higher CH_4 formation and selectivity to CH_4 compared to the case of γ-Al_2O_3. This supposed new reaction pathway of hydrogen migration, proton transport through the bulk of proton conducting oxide. The presence of proton transport in the bulk was identified using yttrium doped barium zirconate.

5.2 Experimental

5.2.1 Sample preparation

Co nanoparticles with ~15 nm size were prepared by standard Schlenk techniques under an argon atmosphere as reported previously[9]. 1.025 g cobalt carbonyl (Sigma, moistened with 1~10% hexane, ≥90% Co) was dissolved in 6 mL 1,2-dichlorobenzene (Sigma, 99%). All manipulations of $Co_2(CO)_8$ were carried out in a glove box under N_2. 0.3 mL oleic acid (Alfa Aesar, 90%) and

30 mL 1,2-dichlorobenzene (DCB) was added in a 100 ml three-neck flask. The solution was degassed for 20 min and then stirred under argon for another 20 min. The solution was further heated to 170 ^{o}C and $Co_2(CO)_8$ in DCB (0.5 M) was injected quickly into the solution under vigorously stirring. The brown solution turned black indicating the formation of colloidal particles. This solution was kept at 170 ^{o}C for 20 min and allowed to cool to 50 ^{o}C. Co nanoparticles were precipitated by adding 20 mL DCB and 40 mL 2-proponal (ACS Grade), followed by centrifugation (8000 rpm). The precipitated solid was re-dispersed and stored in chloroform (ACS Grade) for further use.

Pt nanoparticles with ~3 nm size were prepared based on the procedure reported in the literature [15]. 80 mg Platinum (II) acetylacetonate (Alfa Aesar, ≥48% Pt) was added in 10 mL 1-octadecene (Alfa Aesar, 90%) with 1 mL oleic acid (Alfa Aesar, 90%) and 1 mL oleylamine (Sigma, 98%). The solution was degassed for 20 min and then stirred under argon for another 20 min. Under vigorously stirring, the solution was then slowly heated to 120 ^{o}C and kept for 30 min to dissolve $Pt(acac)_2$. The temperature was further raised to 200 ^{o}C and the yellow solution turned black indicating the formation of colloidal Pt nanoparticles. This solution was kept at 200 ^{o}C for 30 min and allowed to cool to room temperature. Pt nanoparticles were precipitated by adding 20 mL acetone (Semiconductor grade) and 20 mL methanol (Semiconductor grade), followed by centrifugation (8000 rpm). The precipitated solid was redispersed and stored in chloroform (ACS Grade) for further use.

As supports for Co or Pt catalysts in CO_2 methanation, $BaZrO_3$ (BZ), $BaZr_{0.95}Y_{0.05}O_{3-\delta}$ (BZY05) and $BaZr_{0.8}Y_{0.2}O_{3-\delta}$ (BZY2) were synthesized utilizing a modified Pechini method[13,16]. Aqueous solutions of Ba, Zr and Y (>99% pure, Alfa Aesar, Ward Hill, MA, USA) nitrate salts were prepared and the metal concentration determined by redox titration[17]. The solutions were mixed, in the stoichiometric ratio to fabricate the desired composition, with chelating agent EDTA (99%, Alfa Aesar, Ward Hill, MA) and citric acid monohydrate (99.0-102.0%, Alfa Aesar). The pH was

adjusted to > 8.5 by addition of ammonium hydroxide (14.8N, Fisher Scientific) and excess water was evaporated. The resulting homogeneous gel was combusted in an oven at 300 °C, and the resulting powder sintered for 4h at 1300 °C. Synthesized nanoparticle Co or Pt were supported on the synthesized pure oxide (1wt-% Co, 0.2wt-% Pt denoted 1Co/BZ or 0.2Pt1Co/BZ in the following) using a standard incipient wetness procedure[13,18] where chloroform was utilized as solvent. γ-Al_2O_3 (>99% pure, Alfa Aesar, Ward Hill, MA, USA) was employed for nanoparticle Co or Pt catalyst supported on Al_2O_3.

5.2.2 Catalyst characterization

The synthesized materials were characterized by powder X-ray diffraction with Cu Kα radiation and fixed slit width (MiniFlex (II), Rigaku, The Woodlands, TX, USA). Diffraction patterns were recorded in the 2θ range of 20°-70° with a step size of 0.02° and a counting time of 0.2 min/degree. The BET surface area (ASAP2020, micrometrics, Norcross, GA, USA) was measured using krypton gas as the absorbent after samples were degassed at 300 °C for 10h. TEM imaging was conducted using a 200kV JEOL 2000FX conventional TEM equipped with an Oxford Instruments XEDS system. Co and Pt nanoparticle samples were prepared by drop casting the colloidal solution onto a holey carbon-coated copper grid and allowing the liquid component to fully evaporate. TEM image of supported catalyst were obtained with the powder sample before and after reaction. Prior to TEM imaging, the catalyst before reaction was oxidized to remove surface contaminants at 500oC for one hour in a flow of 50mL/min 19.5 – 23.5 vol% O_2/N_2 (GTS-Welco, Allentown, PA,USA), and then reduced at 450 °C under flowing 5 vol% H_2 / Ar (UHP gases, < 1ppm O_2, GTS-Welco, Allentown, PA, USA) for one hour. The catalyst after reaction was utilized at in CO2 methanation at 300 °C for three hours. The catalyst samples were prepared by adding dry powder onto the grid. X-ray photoelectron spectra (XPS) measurements were performed to investigate the oxidation state of nanoparticle Co supported on BZ and Al_2O_3. Prior to XPS measurement, samples were pretreated by same procedure utilized for TEM sample.

The samples were mounted on double sided carbon tape and transferred to a sample holder. No signal from the carbon tape was visible in XPS. The spectra were obtained on a Thermo Scientific K-Alpha with monochromated Al Kα x-ray source with energy of 1486.6 eV. The beam spot was an ellipse with a major axis of 400 microns and a minor axis of 250 microns.

5.2.3 Catalyst testing

CO2 methanation was performed with sieved powder (106-150μm) as a fixed bed in a continuous flow quartz tube reactor (i.d. 4mm with the length of 300mm). The 20mg catalyst sample was held by quartz glass wool. Gas flows were regulated by mass flow controllers (Brooks, 4850 series, Exton, PA, USA). Prior to measurement the samples were heated to 500 ^{o}C at a rate of 10 ^{o}C/min in a flow of 100mL/min dry air with < 0.5 ppm CO_2, then held for 1h at this temperature to remove moisture and contaminants on the surface of the powder sample. The powder sample cooled to 450^{o}C under the same flow conditions, and subsequently reduced at 450^{o}C temperature for 1h under flowing 50ml/min 5 vol% H_2 / N_2. The reactor was flushed with Ar and cooled to measurement temperature after this pretreatment, prior to feeding the reactant mixture of 3 vol-% CO_2, 9 vol-% H_2 balanced with Ar (UHP gases, < 1ppm O_2, GTS-Welco, Allentown, PA, USA) at 100mL/min at measurement temperature. This procedure was repeated with steps of 25 ^{o}C between 200 ^{o}C and 350 ^{o}C. The initial concentration of reactants, CO_2 (m/e=44), and products, CO (m/e=28) and CH_4 (m/e=16), were monitored (sampling frequency, 1.67s^{-1}) for 10min at each temperature using a residual gas analyzer (RGA) fitted with a quadropole analyzer and associated Faraday and secondary electron multiplier detectors (Cirrus 2, MKS Instruments UK Ltd). The amount of deposited carbon was determined by the amount of generated CO_2 calculated from numerical integration of CO_2 peak area. CO_2 peak area was calibrated by using 100μL pulse of CO_2. The deactivated powder sample was burned off by oxidization process at 500 ^{o}C in a flow of 100mL/min dry air with < 0.5 ppm CO_2.

5.3 Results and Discussion

As a supports for Co-Pt catalysts in CO_2 methanation, pure $BaZrO_3$ (BZ), $BaZr_{0.95}Y_{0.05}O_{3-\delta}$ (BZY05) and $BaZr_{0.8}Y_{0.2}O_{3-\delta}$ (BZY2) were synthesized, the X-ray diffraction patterns for BZ and BZY05 were indexed to an cubic perovskite structure (space group $Pm\bar{3}m$)[19-21], tetragonal structure ($P4mm$) for BZY2 [22,23], figure 5.1.

Figure 5.3 a-b show transmission electron micrographs of as prepared NPs of Co and Pt, used for supported catalyst, showing that the diameters of Co and Pt are ~15 and ~3nm respectively. The micrographs of supported Co and Pt over BZ before and after reaction are shown in figure 5.3 c-d, identifying that Co NPs with corresponding size were well deposited over the surface of BZ, however Pt NPs wasn't readily identified due to extremely small size and low loading, 0.2 wt%. For Pt identification, EDX measurement was not available due to the overlap of Ba, Zr and Pt peaks, figure 5.2. The micrographs of the catalyst sample after reaction for 3 h indicates that no change in particle size during reaction is occurred.

Figure 5.4 a shows CH_4 yield as a function of the temperature over 0.2g of catalyst samples; 1Co/Al, 0.2Pt1Co/Al, 1Co/BZ and 0.2Pt1Co/BZ. It should be noted that the yield and selectivity reported in this study is only for gas-phase products, measured at 10min on-stream. All catalysts are showing increasing trends in CH_4 yield with increasing temperature; 200-350 ^oC. For example, the CH_4 yields over 1Co/BZ were 0.4, 4.5 and 8.3% at 250, 300 and 350 ^oC, respectively. At same loading of Co, BZ shows about four times higher CH_4 yield compared to γ-Al_2O_3; 7.2 and 1.7% at 325 ^oC for 1Co/BZ and 1Co/Al. The addition of Pt leads to significant enhancement in CH_4 yield over both γ-Al_2O_3 and BZ supports, in good agreement with a previous report[10,11].

Figure 5.1 X-ray diffraction patterns of BZ, BZY05 and BZY20.

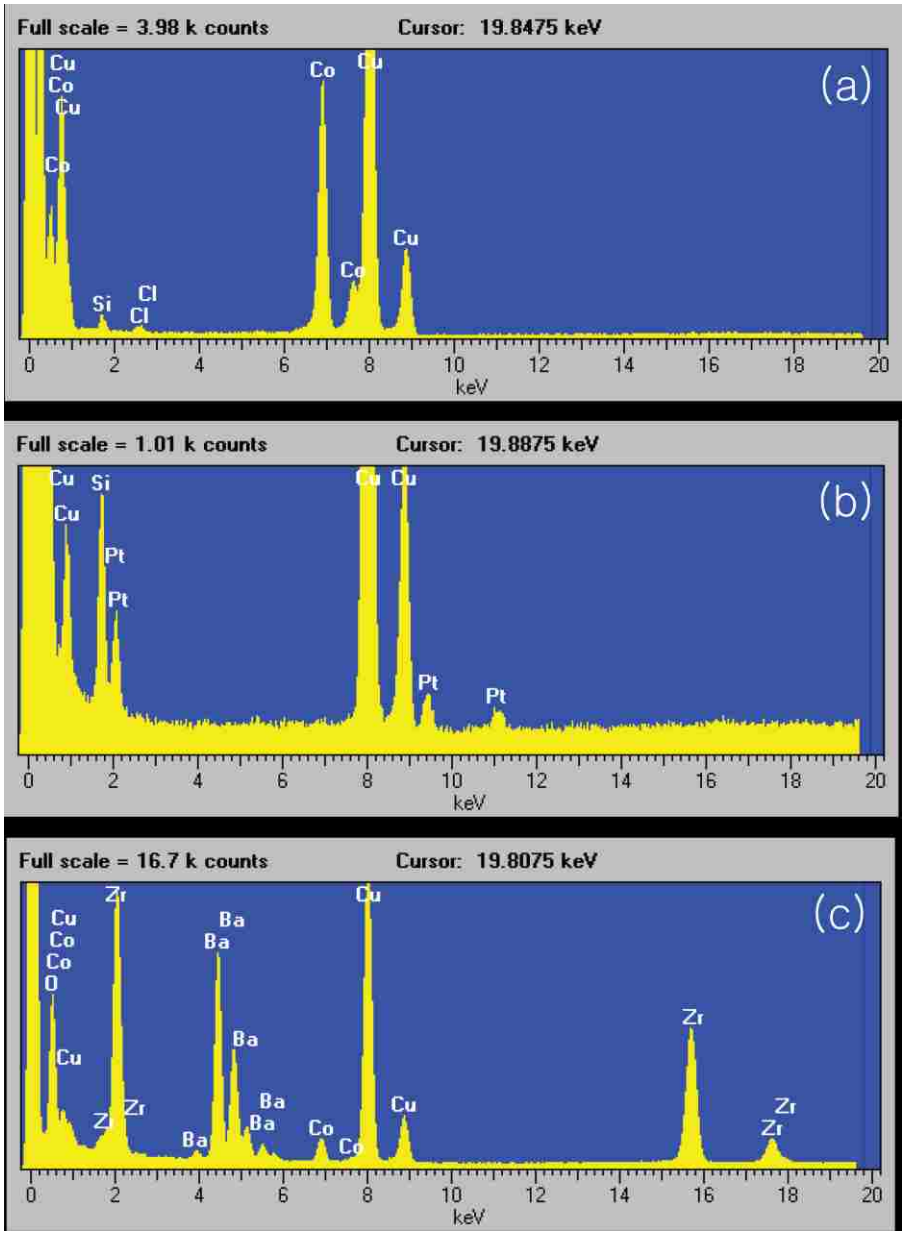

Figure 5.2 Energy dispersive X-ray spectroscopy: (a) Co nanoparticles, (b) Pt nanoparticles, (c) supported Co and Pt over BZ.

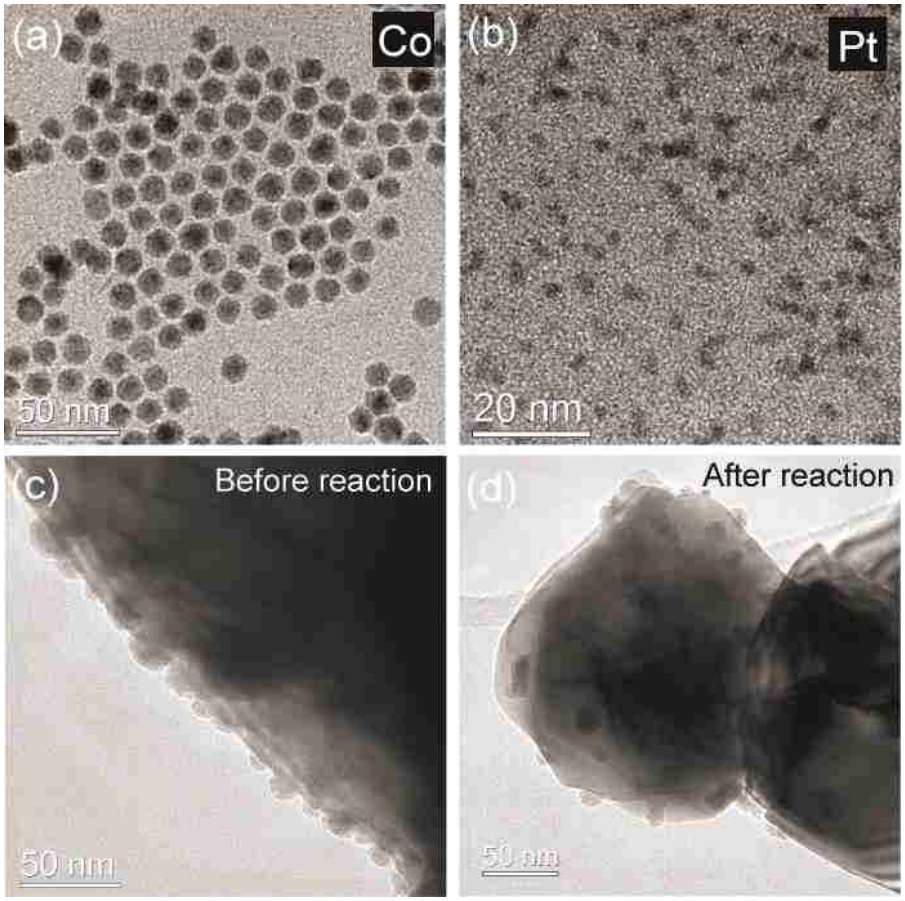

Figure 5.3 Transmission electron micrograph of (a) as prepared cobalt nanoparticles, (b) cobalt nanoparticles, supported Pt and Co catalyst over BZ (c) before reaction and (d) after reaction for 3h.

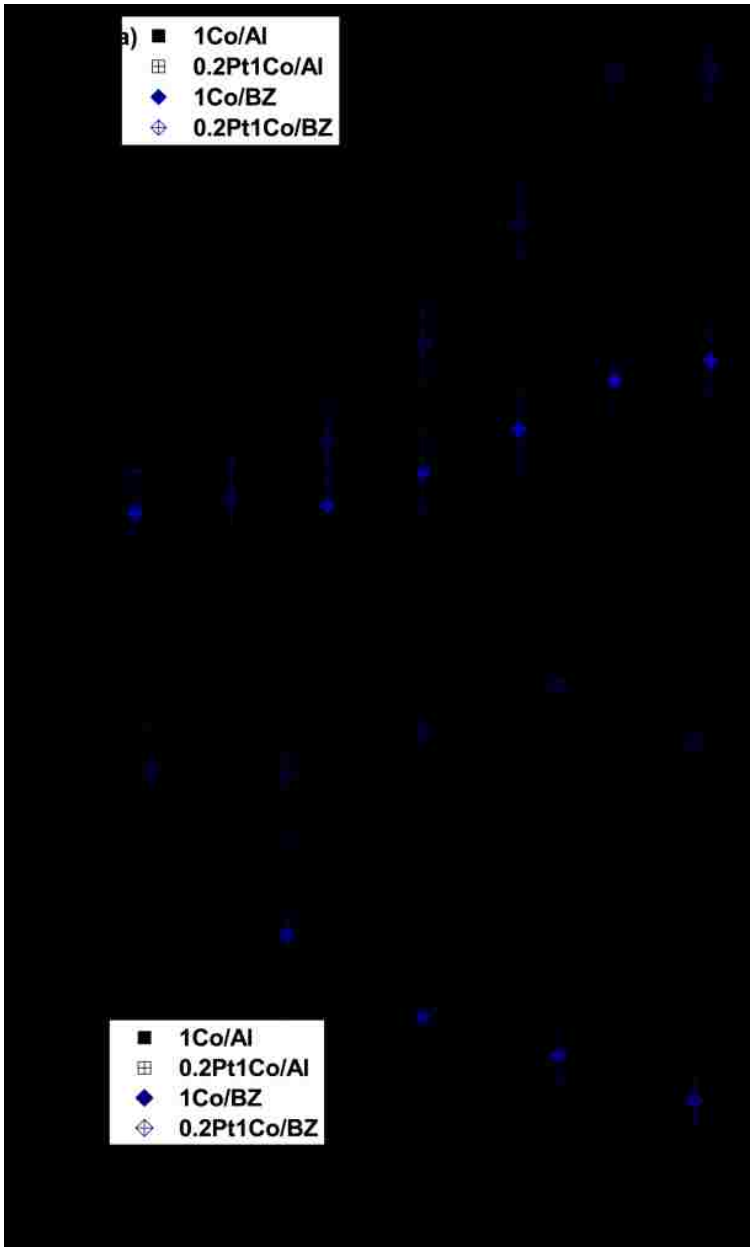

Figure 5.4 (a) CH4 yield and (b) selectivity to CH4 versus temperature over 1Co/Al, 0.2Pt1Co/Al, 1Co/BZ and 0.2Pt1Co/BZ.

Figure 5.4 a shows CH_4 yield as a function of the temperature over 0.2g of catalyst samples; 1Co/Al, 0.2Pt1Co/Al, 1Co/BZ and 0.2Pt1Co/BZ. It should be noted that the yield and selectivity reported in this study is only for gas-phase products, measured at 10min on-stream. All catalysts are showing increasing trends in CH_4 yield with increasing temperature; 200-350 ^oC. For example, the CH_4 yields over 1Co/BZ were 0.4, 4.5 and 8.3% at 250, 300 and 350 ^oC, respectively. At same loading of Co, BZ shows about four times higher CH_4 yield compared to γ-Al_2O_3; 7.2 and 1.7% at 325 ^oC for 1Co/BZ and 1Co/Al. The addition of Pt leads to significant enhancement in CH_4 yield over both γ-Al_2O_3 and BZ supports, in good agreement with a previous report[10,11].

The influence of Pt addition on CO_2 methanation was more significant in case of BZ than γ-Al_2O_3; 3.3 and 2.2 times enhancement for BZ and γ-Al_2O_3 at 325 ^oC in comparison with the catalysts without Pt, respectively. The CH_4 yield of 0.2Pt1Co/BZ was more than 6 folds higher than 0.2Pt1Co/Al; 23.9 and 3.7 % at 325 ^oC. No detectable CO_2 methanation was observed in only Pt (1 wt%) supported catalyst on in our study. In terms of CO production, no significant deference was observed between supported Co and Co-Pt over BZ. This is in good accordance with Beaumont et al.[10,11], reported that observed enhancement in CH_4 methanation over supported Pt and Co catalyst was attributed to the improved dissociative chemisorption of H_2 over Pt, followed by the spillover of dissociated hydrogen. This is also supported by our previous report where Pt/BZ showed significantly higher H_2 surface exchange rate than Co/BZ[13]. In addition, this enhancement in CH_4 yield by Pt addition indicates that Co-Pt is not bimetallic as reported in literature[11] where bimetallic Co-Pt inhibited the reaction due to Pt segregation in reducing atmosphere.

Gas phase selectivity to CH_4 for each catalyst was shown in figure 5.4 b. Note that the only other gas phase products detected were CO, H_2 and water. Except for 0.2Pt1Co/BZ, the CH_4 selectivity of all catalysts decreased with increasing temperature. For example, the CH_4 selectivity of 1Co/BZ was 53.5, 44.8, 40.7 and 35.9% at 275, 300, 325 and 350 ^oC. The

selectivity of 0.2Pt1Co/BZ slightly increased with increasing temperature until 325°C, where the selectivity was 79.8%. Note that CO formation is not affected by Pt addition, implying that CO_2 methanation is not related to reverse water gas shift reaction in CO_2 reduction, CH_4 is not formed through secondary reaction; re-adsorption of CO[11].

XPS measurement was performed to investigate the oxidation state of supported Co over BZ and γ-Al_2O_3 (see supporting information for preparation procedure of sample) figure 5.5. The Co2p and Co3p spectra were fit using peaks from reference samples in Thermo Avantage Data System. In case of 1Co/BZ and 0.2Pt1Co/BZ, Co2p region was not available due to the overlap of Co2p and Ba3d peak. The XPS spectra indicate that Co in all catalysts consists of CoO and Co_3O_4, no metallic Co was observed, figure 5.5. Highly active cobalt oxide in CO_2 hydrogenation were observed in previous literatures; Co_3O_4 on SiO_2[24] and CoO on TiO_2[7]. The addition of Pt led to more reduction of Co; ~65% of CoO fraction in 0.2Pt1Co/BZ and ~11% in 1Co/BZ. This is in good agreement with the report by Beaumont et al.[10]. On the other hand, no co-relation between the fraction of CoO and CO_2 methanation was observed, this suggests that different activity of CO_2 methanation observed in this study is attributed to not different oxidation state of Co but other possible factor such as support.

Beaumont et al.[11] demonstrated hydrogen spillover mechanism in CO_2 methanation using individual size controlled Co and Pt, led to significant enhancement in CH_4 formation. In our study, more significant increase in CH_4 yield by Pt addition and increasing selectivity with increasing temperature in 0.2Pt1Co/BZ suppose new possible pathway of hydrogen migration such as proton transfer through bulk of supports. Different amount Y doped BZ; 0, 5 and 20% Y doped BZ for BZ, BZY05 and BZY20 were utilized to test the presence of proton transport through bulk in CO_2 methanation.

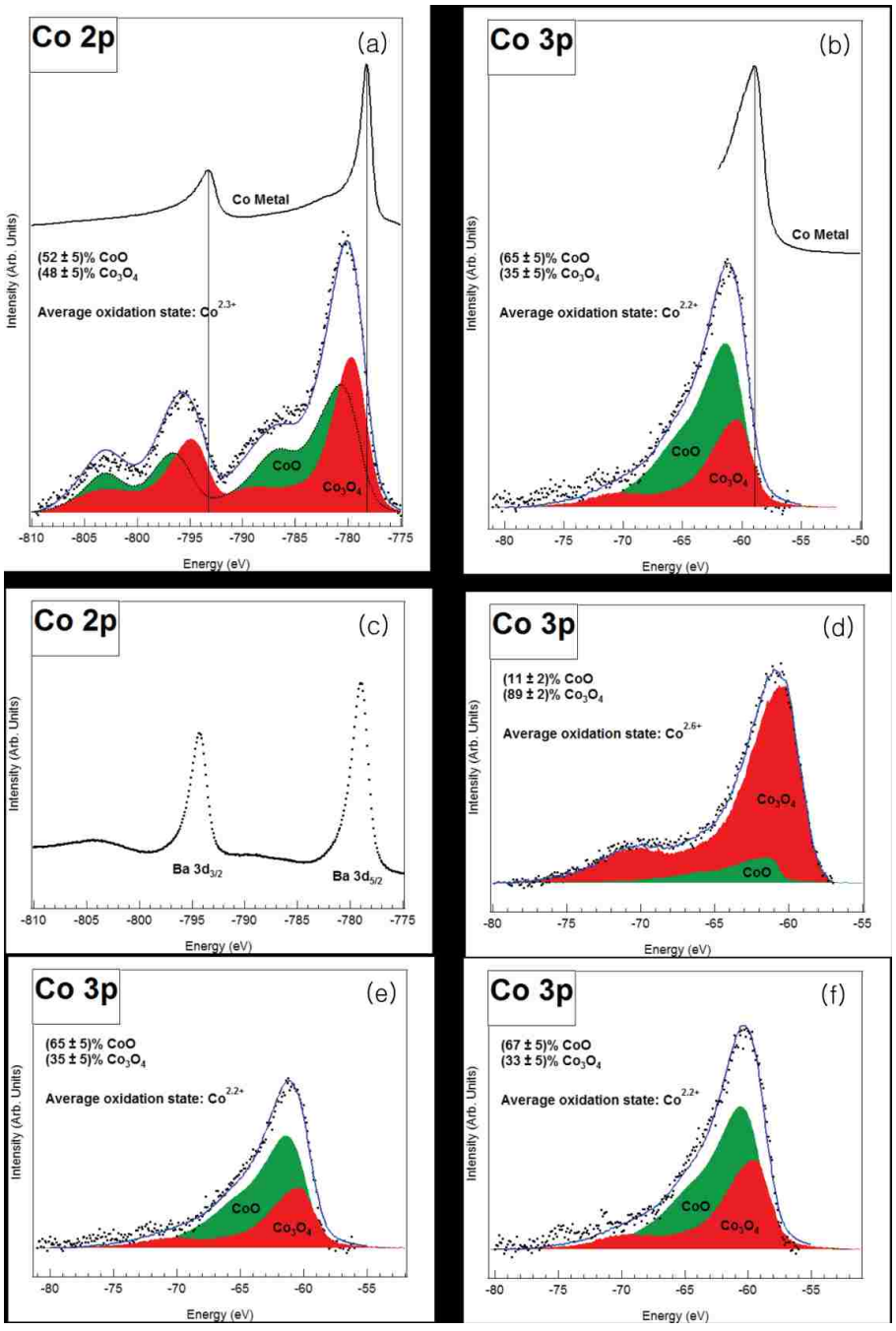

Figure 5.5 . XPS data: (a) and (b) 1Co/Al2O3, (c) and (d) 1Co/BZ (e) 0.2Pt1CoBZ before reaction and (f) 0.2Pt1CoBZ after reaction for 24h.

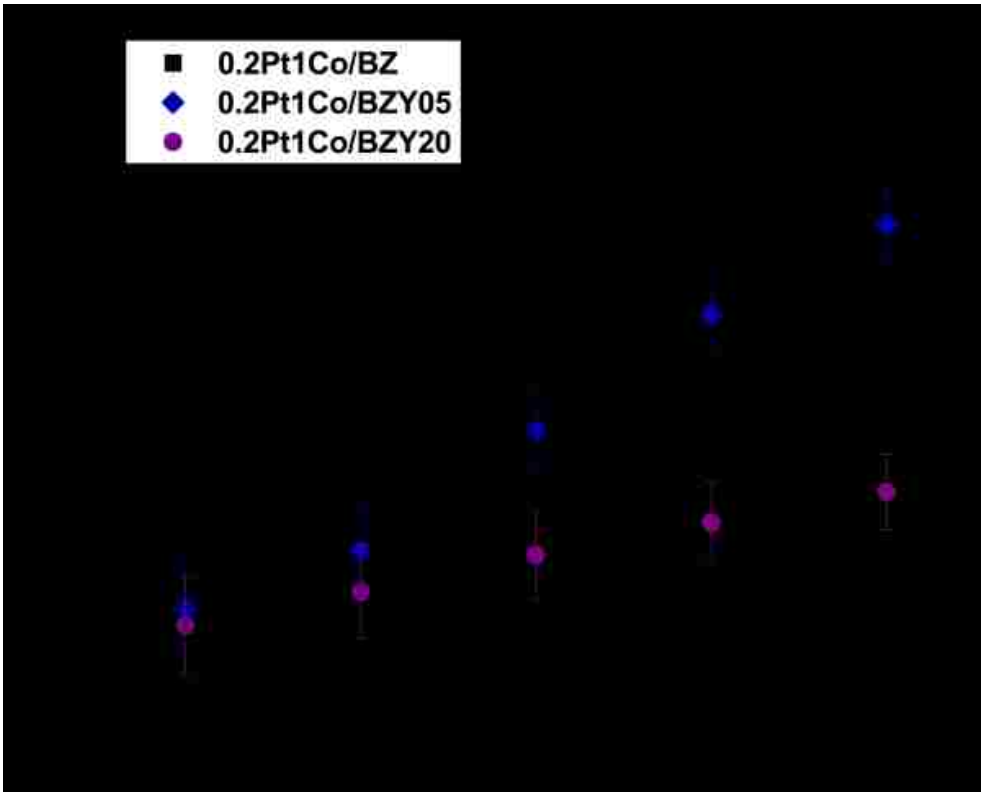

Figure 5.6 CH4 yield versus temperature over 0.2Pt1Co over BZ, BZY05 and BZY20

Figure 5.6 shows CH_4 yield over BZ, BZY05 and BZY2 as a function of temperature. All catalyst shows increasing CH_4 yield with increasing temperature, the effect of Y doping was clearly observed; increasing amount of Y doped resulted in decreases of CH_4 yield; 23.8, 15.5 and 6.5% for BZ, BZY05 and BZY20 at 325 ^oC. In contrast with the improvement in proton conductivity by Y doping into $BaZrO_3$ in solid oxide fuel cell[23], the reduction in CH_4 yield with increasing amount of Y doping might supports the absence of proton transfer through bulk in CO_2 methanation. On the other hand, Yamazaki et al.[25] reported proton trapping phenomena in Y doped BZ by proton-dopant association evidenced by proton nuclear magnetic resonance study. This proton trapping might explains lower CH_4 yield at higher amount of Y doped, reversely supports the catalytic enhancement in CO_2 methanation by proton transfer in bulk. The catalytic enhancement by incorporated proton into the bulk might be also supported by our previous research where supported Cr over BZ showed one order magnitude higher ethylene formation rate in comparison to the one over γ-Al2O3.

The life time test was performed over 0.2Pt1Co/BZ utilized at 300 and 350 ^oC. The CH_4 yield and selectivity to CH_4 was shown in figure 5.6 a. At 350 ^oC, the catalyst was rapidly deactivated to 25.9 and 42.4 % of initial CH_4yield and selectivity to CH_4; 22.2 and 5.7% in CH_4 yield and 73.3 and 31.2% in selectivity to CH_4 at 0 and 3h, respectively. In contrast, 300 ^oC reaction temperatures resulted in significantly gradual deactivation in CH_4 yield and selectivity to CH4; 66.6 and 65.8 % of initial CH_4 yield and selectivity to CH_4 at 24 h. As a primary reason for deactivation, oxidation by water formed in CO_2 methanation over Co catalyst was considered[10,26]. On the other hand, our XPS results shows no change in the oxidation state of Co after 24h in CO_2 methanation, figure 5.7. This supports that the catalyst is unlikely to be deactivated by water. Figure 5.8 shows TPO results of catalyst tested for 3h at 300 and 350 ^oC, respectively. CO_2 evolution was clearly observed as a single peak with maximum at 380 ^oC over the catalyst tested at 350 ^oC. This implies that the deposited carbon is not graphitic. In contrast, no significant CO2

evolution peak was observed in the catalyst utilized at 300 °C. The calculated number of deposited C atom per Co was 0.4 when tested at 350 °C for 3h. This explains no change in CH_4 yield over 0.2Pt1Co/BZ at 350 °C in figure 5.3 a. Thus, we supposed that the deactivation of catalyst is due to carbon deposition formed carbon-oxygen breaking, it seems that accumulated oxygen might be reduced by significant amount of hydrogen evolved from proton conducting supports. In addition, carbon deposition indirectly supports directly CH_4 formation from CO2 in one step.

It was clearly demonstrated that the proton conducting oxide has a potential as a support for Co-Pt catalyst in CO_2 methanation. The addition of Pt resulted in significant enhancement in CO_2 methanation, the effect of Pt addition was quite amplified in case to use proton conducting oxide; at same loading of Co-Pt, proton conducting oxide leads to six times higher CH_4 yield compared to γ-Al_2O_3. Furthermore, the selectivity to CH_4 over 0.2Pt1Co/BZ was maintained over 70% at all the range of temperature utilized in this study, 250~300 °C. Utilization of proton migration trough the bulk of proton conducting oxide for CO_2 methanation was demonstrated by differed amount of Y-doped BZ, where significant decrease in CH_4 yield with increasing Y-doping was observed . This indicates that proton is trapped by Y dopant, this proton trapping leads low CH_4 yield and selectivity. The TPO study clearly showed that Co catalyst was deactivated by carbon deposition.

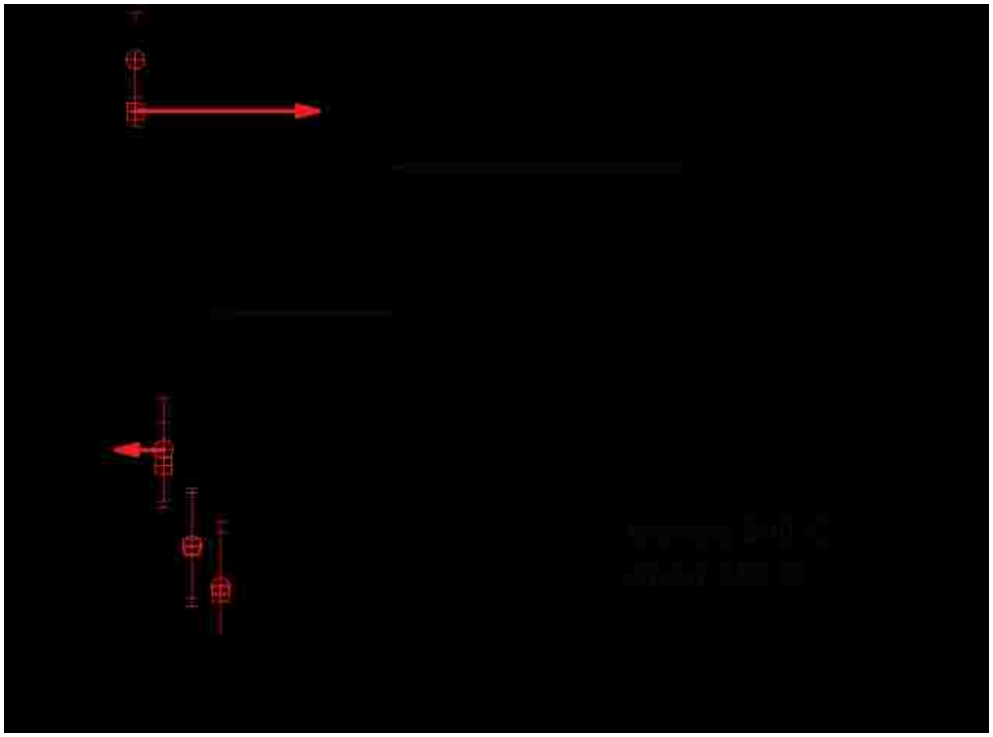

Figure 5.7 (a) CH4 yield versus time over 0.2Pt1Co/BZ at 300 and 350 °C and (b) temperature programmed oxidation (TPO) showing CO2 evolution (m/e 44) of carbon deposited during CO2 methanation at 300 and 350 °C.

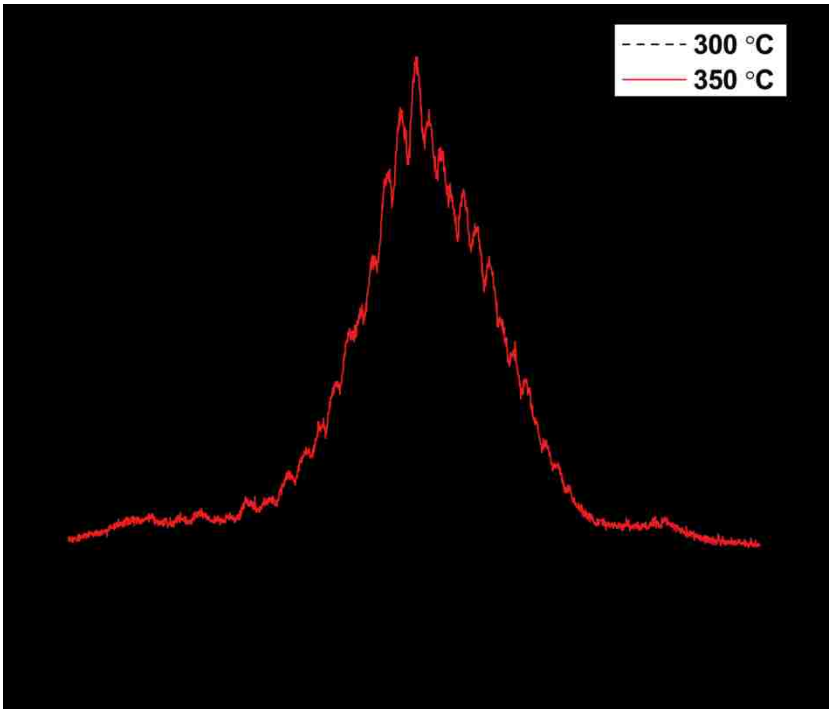

Figure 5.8 temperature programmed oxidation (TPO) showing CO2 evolution (m/e 44) of carbon deposited during CO2 methanation at 300 and 350 °C.

5.4 References

1. Ritter, S. K. *Chem. Eng. News* **2007**, *85*, 11-17.

2. Schwartz, S. E. *Energy Environ. Sci.* **2008**, *1*, 430-453.

3. Anonymoushttp://www.eia.gov/forecasts/ieo/ (accssed April 12,2005).

4. Centi, G.; Quadrelli, E. A.; Perathoner, S. *Energy Environ. Sci.* **2013**, *6*, 1711-1731.

5. Watson, G. H. *Methanation Catalysis;* International Energy Agency Coal Research: London, 1980; .

6. Alayoglu, S.; Beaumont, S. K.; Zheng, F.; Pushkarev, V. V.; Zheng, H.; Iablokov, V.; Liu, Z.; Guo, J.; Kruse, N.; Somorjai, G. A. *Top Catal* **2011**, *54*, 778-785.

7. Melaet, G.; Ralston, W. T.; Li, C.; Alayoglu, S.; An, K.; Musselwhite, N.; Kalkan, B.; Somorjai, G. A. *J. Am. Chem. Soc.* **2014**, *136*, 2260-2263.

8. Khodakov, A. Y.; Chu, W.; Fongarland, P. *Chem. Rev.* **2007**, *107*, 1692-1744.

9. Iablokov, V.; Beaumont, S.; Alayoglu, S.; Pushkarev, V.; Specht, C.; Gao, J.; Alivisatos, A. P.; Kruse, N.; Somorjai, G. A. *Nano Lett.* **2012**, *12*, 3091-3096.

10. Beaumont, S. K.; Alayoglu , S.; Specht, C.; Michalak, W. D.; Pushkarev, V. V.; Guo, J.; Kruse, N.; Somorjai, G. A. *J. Am. Chem. Soc.* **2014**, *136*, 9898-9901.

11. Beaumont, S. K.; Alayoglu, S.; Specht, C.; Kruse, N.; Somorjai, G. A. *Nano Lett.* **2014**, *14*, 4792-4796.

12. Shin, H. H.; McIntosh, S. *ACS Catal.* **2015**, *5*, 95-103.

13. Shin, H. H.; McIntosh, S. *J. Mater. Chem. A* **2013**, *1*, 7639.

14. Dorner, R. W.; Hardy, D. R.; Williams, F. W.; Davis, B. H.; Willauer, H. D. *Energy Fuels* **2009**, *23*, 4190-4195.

15. Wang, C.; Daimon, H.; Lee, Y.; Kim, J.; Sun, S. *J. Am. Chem. Soc.* **2007**, *129*, 6974-6975.

16. H. E. van Doorn, R.; Kruidhof, H.; Nijmeijer, A.; Winnubst, L.; J. Burggraaf, A. *J. Mater. Chem.* **1998**, *8*, 2109-2112.

17. Vogel, A. *Textbook of Quantitative Inorganic Analysis;* Longman Scientific and Technical: Longman, Harlow, United Kingdom, 1986; .

18. Levy, P.; Primet, M. *Applied Catalysis* **1991**, *70*, 263-276.

19. Stokes, S. J.; Islam, M. S. *J. Mater. Chem.* **2010**, *20*, 6258-6264.

20. Braun, A.; Duval, S.; Ried, P.; Embs, J.; Juranyi, F.; Strässle, T.; Stimming, U.; Hempelmann, R.; Holtappels, P.; Graule, T. *J. Appl. Electrochem.* **2009***, 39*, 471-475.

21. Duval, S. B. C.; Holtappels, P.; Vogt, U. F.; Stimming, U.; Graule, T. *Fuel Cells* **2009***, 9*, 613-621.

22. Tao, S.; Irvine, J. T. S. *Journal of Solid State Chemistry* **2007***, 180*, 3493-3503.

23. Kreuer, K. D.; Adams, S.; Münch, W.; Fuchs, A.; Klock, U.; Maier, J. *Solid State Ionics* **2001***, 145*, 295-306.

24. Owen, R. E.; O'Byrne, J. P.; Mattia, D.; Plucinski, P.; Pascu, S. I.; Jones, M. D. *Chem. Commun.* **2013***, 49*, 11683-11685.

25. Yamazaki, Y.; Blanc, F.; Okuyama, Y.; Buannic, L.; Lucio-Vega, J. C.; Grey, C. P.; Haile, S. M. *Nature materials* **2013***, 12*, 647-651.

26. Saib, A. M.; Moodley, D. J.; Ciobîcă, I. M.; Hauman, M. M.; Sigwebela, B. H.; Weststrate, C. J.; Niemantsverdriet, J. W.; van de Loosdrecht, J. *Catalysis Today* **2010***, 154*, 271-282.

6. Conclusion

The work presented in this dissertation shows the possibility toward proton conducting solid oxide fuel cell (SOFCs) for co-generation of power and fuel. The primary focus of this work is to study the kinetics in anode of SOFCs as most prior research in SOFCs has focused on enhancing electrolyte conductivity, with little knowledge available regarding hydrogen or water dissociation kinetics. SOFC performance is determined by a combination of many kinetic steps, including surface electrocatalysis and bulk ion-electron transport. This dissertation demonstrates the reaction mechanism of fuel oxidation in the anode of SOFCs by pulsed isotope experiments, provides insight into hydrocarbon fuelled SOFC and fuel production in proton conducting electrolyzer cell via catalytic study.

Chapter 2 and 3 of this dissertation are focused on the hydrogen fuel oxidation in the anode of SOFCs. While the pulsed isotope experiments utilized in this study were demonstrated to effectively measure the H_2/D_2 surface exchange rate on a range of ionic conducting oxides, it was determined that ionic conducting oxide acts as inert for the reaction in our measurement. With respect to their use in cermet electrodes, it is clear that, with the exception of Cu, the metal component of the electrode will dominate the observed exchange kinetics. Therefore, hydrogen-spillover mechanism can be supposed for hydrogen oxidation reaction in SOFC anodes, further work is required for the detail about the electrochemical charge-transfer steps, the role of H_2O and exact nature of the active site.

Chapter 4 demonstrates the potential of proton conducting oxide as a Cr catalysts supports for short contact time ethane dehydrogenation. The use of proton conducting oxide as supports of Cr catalysts led to more than one order of magnitude higher ethylene formation rate compared to 10Cr/Al in our study. While all of the samples showed deactivation due to coke, the use of the higher activity barium cerate or barium zirconate support materials could enable commercial productivity to be maintained at reduced operating temperatures with associated reduced carbon

deposition rates. In addition to potentially opening new reaction pathways through proton incorporation in the support material[11], the use of a proton conducting support opens the possibility of creating electrochemical reactors systems for cogeneration of olefins and electricity.

In the following chapter, we examine the possibility to use proton conducting oxide as support for Co and Pt catalyst in CO_2 methanation. It was clearly identified that introduction of proton conducting oxide as supports for Co and Pt catalyst in CO_2 methanation resulted in significantly higher CH_4 formation and selectivity to CH_4 compared to the case of γ-Al_2O_3. This finding opens up new reaction pathway in hydrogen migration, proton transport through the bulk of proton conducting oxide, for CO_2 methanation, also implies the possible fuel production with CO_2 in proton conducting electrolyzer cell.

7. Vita

Hyunho Shin was born to the Shins; Wooksung Shin and Kilnyu Shin, on April 25, 1980 in Seoul, South Korea. He started his study in Chemical Engineering at Chung-Ang University in 2000. He received his BS degree in 2007, and then attended to graduate school in corresponding university. Two years later, he received his MS degree in 2009, and then started to work in Korea Institute of Ceramic Engineering and Technology as a researcher. One year later, he came to Lehigh University to continue to study as a PhD student and started his research career in solid oxide fuel cell (SOFCs) and catalysis under the supervision of Prof. Steven McIntosh. He devoted his five years in research in fuel oxidation mechanism in anode of proton conducting SOFCs and application of proton conducting oxide as a supports for catalyst. The main results are described in this thesis